Dragan Maletic, BSc

Electromagnetic Model of a Power Transformer for Low Frequencies

MASTER'S THESIS

to achieve the university degree of

Diplom-Ingenieur

Master's degree programme: Electrical Engineering and Business

submitted to

Graz University of Technology

Supervisors

Ao.Univ.-Prof. Dipl.-Ing. Dr.techn. Herwig Renner
Institute of Electrical Power Systems

Dennis Albert, M.Sc
Institute of Electrical Power Systems

Graz, August 2021

AFFIDAVIT

I declare that I have authored this thesis independently, that I have not used other than the declared sources/resources, and that I have explicitly indicated all material which has been quoted either literally or by content from the sources used. The text document uploaded to TUGRAZonline is identical to the present master's thesis.

Date, Signature

Abstract

Transmission grid operators are always trying to improve their simulation models since simulations help to predict the behavior of the electricity grid. Transformers are a particularly important component of the grid. The usual modeling approach of transformers is the classic T-model. This model, however, is not able to model unbalanced and transient occurrences accurately. In this thesis, a topologically correct network model is derived, which is capable of reproducing the behavior of an actual three-phase power transformer under the influence of low-frequency transients. The non-linearity of the core material is reproduced with the Jiles-Atherton hysteresis model to represent this behavior accurately. Another difficulty in transformer modeling is the lack of parameter data. It is shown in this thesis that the parameters of the network model can be determined from standard transformer acceptance tests and a simple single-phase hysteresis measurement. The execution of the hysteresis measurement is possible outside of specialized laboratories. The model was compared to multiple measurements, including no-load tests and back-to-back tests with superimposed direct currents. The results show that an accurate transformer model can be derived with reasonable effort. The simulation model provides transmission grid operators an important and accurate tool for the simulation of low-frequency transients.

Kurzfassung

Netzbetreiber sind stetig daran interessiert ihre Simulationsmodelle zu verbessern, da diese dabei helfen das Verhalten des Stromnetzes vorauszusagen. Eine besonders wichtige Komponente des Stromnetzes sind Transformatoren. Die gängige Methode einen Transformator zu modellieren ist das klassische T-modell. Allerdings ist dieses Modell nicht geeignet, um unsymmetrische und transiente Ereignisse genau zu beschreiben. In dieser Arbeit wird am Beispiel eines realen dreiphasigen Leistungstransformators ein topologisch-korrektes Netzwerkmodell entwickelt, welches in der Lage ist das Verhalten des Transformators unter dem Einfluss niederfrequenter transienter Vorgänge zu simulieren. Um dieses Verhalten genau darzustellen, wird die Nichtlinearität des Transformatorkerns mithilfe des Jiles-Atherton Hysteresemodels modelliert. Eine weitere Schwierigkeit bei der Modellierung ist das Fehlen von Parameterdaten. In dieser Arbeit wird gezeigt, dass die Parameter des Netzwerkmodells mithilfe von Abnahmetestdaten und einer einfachen einphasigen Hysteresemessung herleitbar sind. Die Hysteresemessung ist auch außerhalb von speziellen Laboren durchführbar. Das Modell wurde mit mehreren Messungen verglichen, darunter Messungen in Leerlauf und Back-to-back mit überlagertem Gleichstrom. Die Ergebnisse zeigen, dass mit überschaubarem Aufwand ein genaues Simulationsmodell erstellt werden kann. Dieses liefert Netzbetreibern ein wichtiges und genaues Werkzeug in der Simulation von niederfrequenten transienten Vorgängen.

List of Symbols

α	Jiles-Atherton parameter representing interdomain coupling
δ	Jiles-Atherton sign function
δ_{m}	Sign function to prevent non-physical behavior of the Jiles-Atherton model
Θ_1, Θ_2	Primary and secondary magnetomotive force
μ_0	Vacuum permeability
μ_{r}	Relative permeability
Φ_{m}	Mutual magnetic flux
Φ_{peak}	Peak value of the magnetic flux
Φ_{U}, Φ_{V}, Φ_{W}	Magnetic fluxes of phases U, V, and W
φ_{U}	Phase shift between the voltage and current of phase U
φ_{V}	Phase shift between the voltage and current of phase V
φ_{W}	Phase shift between the voltage and current of phase W
Ψ_{m}	Mutual magnetic flux-linkage
a	Jiles-Atherton parameter representing the shape of the anhysteresis
A_{core}	Transformer core area
B	Magnetic flux density
B_{e}	Effective magnetic flux density
c	Jiles-Atherton parameter representing the reversibility
E	Energy
E_1, E_2	Root mean square values electromotive force of the primary and secondary winding
e_1, e_2	Instantaneous values electromotive force of the primary and secondary winding
f, f_{n}	Frequency, nominal frequency

i_0	Instantaneous magnetizing current
i'_0	Instantaneous zero-sequence current resulting from magnetic asymmetry
i_{LV}, i_{HV}	Instantaneous currents of the low- and high-voltage windings
I_{LV}, I_{HV}	Rated root mean square currents of the low- and high-voltage windigs
$I_{\mathrm{SC,U}}$, $I_{\mathrm{SC,V}}$, $I_{\mathrm{SC,W}}$	Root mean square values of the short-circuit currents of phases U, V, and W
I_{zero}	Root mean square value of the zero-sequence current
J	Magnetic polarization
k	Jiles-Atherton parameter representing hysteresis loss
k_{eddy}	Eddy loss parameter
k_{exc}	Excess loss parameter
L_0	Zero-sequence inductance
L_1, L_2, L_3	Inductances of primary, secondary, and tertiary winding
L_{12}	Short-circuit inductance
L_{C1}	Inductance between core and and first winding
L_{limb}, L_{yoke}	Limb and yoke inductances
L_{m}	Mutual inductance of the magnetizing branch
l_{limb}, l_{yoke}	Lengths of limb and yoke
m	Magnetic moment
M	Magnetization
M_{an}	Anhysteretic magnetization
M_{irr}, M_{rev}	Irreversible and reversible component of the magnetization
M_{s}	Saturation magnetization
N	Number of winding turns
N_1, N_2	Number of primary and secondary winding turns
N_{LV}, N_{HV}	Number of low- and high-voltage winding turns
P_{zero}	Zero-sequence active power
Q_{zero}	Zero-sequence reactive power
R_1, R_2, R_3	Primary, secondary, and tertiary winding resistances
R_{LV}, R_{HV}	Low- and high-voltage winding resistances
R_{m}	Resistance of the magnetizing branch
R_{m12}	Reluctance between the two windings
R_{mC1}	Reluctance between the core and first winding

R_{mlimb}, R_{myoke}	Reluctances of yoke and limb elements
R_{m0}	Zero-sequence reluctance
R_0	Zero-sequence resistance
S_{zero}	Zero-sequence complex power
t	Time
U	Root mean square value of the voltage
U, V, W	Phase identifier
U_1, U_2	Root mean square values of the primary and secondary voltages
u_1, u_2	Instantaneous values of the primary and secondary voltages
U_{LV}, U_{HV}	Rated root mean square voltages of the low- and high-voltage winding
U_{peak}	Peak value of the voltage
$U_{\text{SC,U}}$	Root mean square value of the short-circuit voltage of phases U
$U_{\text{SC,V}}$	Root mean square value of the short-circuit voltage of phases V
$U_{\text{SC,W}}$	Root mean square value of the short-circuit voltage of phases W
U_{zero}	Root mean square value of the zero-sequence voltage
W_{eddy}	Eddy component of the energy loss
W_{exc}	Excess component of the energy loss
W_{hys}	Hysteresis component of the energy loss
W_{tot}	Total energy loss
X_0	Zero-sequence reactance
X_{12}	Short-circuit reactance
Y	Admittance
Z_0	Zero-sequence impedance

List of Abbreviations

AC alternating current

B2B Back-to-back

DC direct current

GIC Geomagnetically induced current

JA Jiles-Atherton

mmf magnetomotive force

rms root mean square

STC Saturable transformer component

T74 Main transformer under test

T90 Second transformer used for back-to-back

Contents

1 Introduction

1.1 Motivation

Transformers, even though they are often taken for granted, are incredibly complicated electromagnetic devices containing various materials that act differently [1]. This complexity leads to different behaviors depending on the excitation [2]. Transmission grid operators express a rising demand for transformer simulation models capable of reproducing various transient behaviors. Such models can help to increase the understanding of transients in the electricity grid.

The classic T-model can not be used for this scenario because it is only valid for steady-state studies. The Pi-model is superior to the T-model and should be considered instead [3]. The use of a Pi-model, however, leads to another problem. The representation of a three-phase transformer using an equivalent single-phase model disregards the magnetic coupling between the phases. This limits the single-phase equivalent models to balanced and steady-state studies [4]. While it is possible to implement extensive models of transformers, a limiting factor is the available data since manufacturers rarely share their design information [2].

Depending on the study, the use of a hysteresis model can be of considerable importance [5]. The implementation of such models can be rather simple in theory, however, the parameter identification of the hysteresis model can be challenging, especially if no data sheet of the core material is available. Even in the unlikely case that such information is available, it is still necessary to adapt it to measurements since the losses of an entire transformer are usually higher than the losses of the pure core material [6].

1.2 Objective of the Thesis

The main objective of this thesis is to develop, implement, and verify a simulation model of a 50 kVA, three-phase, three-limb power transformer. The modeling approach should be applicable to different transformer core topologies and winding configurations. Only information that can either be found in the data sheet or can be measured in the field without great effort should be used. No detailed design data should be used since this information is often not available. Another objective of the thesis is to measure the hysteresis of the core material and to implement a hysteresis model. The finalized model has to be verified with multiple measurements to ensure the accurate representation of various applications. The tests include short-circuit, no-load, and zero-sequence tests. The behavior under geomagnetically induced currents has to be validated using back-to-back tests with superimposed direct currents.

1.3 Outline of the Thesis

Chapter 2 introduces basic concepts necessary to understand not just the modeling approach but the simulation results as well. The chapter consists of explanations of the basic transformer operating principle, the nonlinear behavior of the ferromagnetic core, and the magnetic asymmetry resulting from the core design.

Chapter 3 presents a short overview of possible modeling approaches before the simulation model is developed. The chapter is completed by a description of the parameter identification process of the developed model.

Chapter 4 presents the parameter identification process of the 50 kVA power transformer used for this thesis. The single-phase hysteresis measurement which determines the non-linear core behavior is explained in particular detail.

Chapter 5 compares measurements of various test scenarios to simulations of the developed model. The conducted experiments are short-circuit tests, zero-sequence tests, no-load tests at various voltages and frequencies, and back-to-back tests with superimposed direct currents.

Chapter 6 concludes the most important findings and gives an outlook on possible further research topics.

A conference proceeding on the topic of this thesis was published in cooperation with Dennis Albert and Herwig Renner. This publication can be found in the **Appendix**

2 Essential Transformer Basics

2.1 Transformer Theory

The basic functionality of a transformer, which works with the principle of electromagnetic induction, is best explained with the example of an ideal single-phase transformer. The following insights are based on [1]. A transformer is considered ideal when winding resistances, leakage flux, and core losses are neglected. Such a transformer is illustrated in Figure 2.1. Two windings with N_1 and N_2 turns are linked by a mutual flux Φ_m.

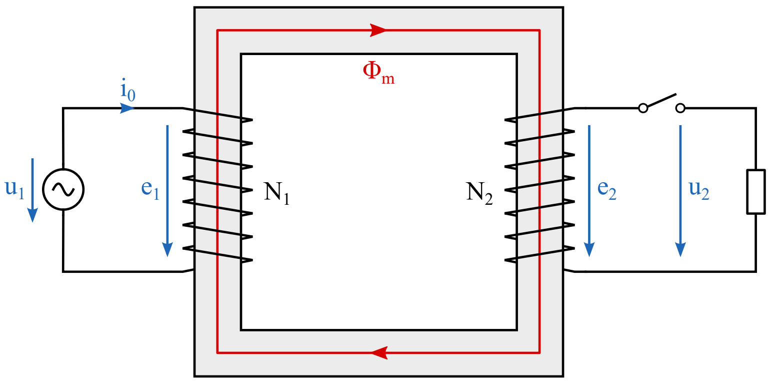

Figure 2.1: Ideal transformer

The first observations are conducted in no-load condition, meaning the secondary winding is left open-circuited. The primary winding is excited with a sinusoidal voltage. This leads to an excitation current, which sets up the mutual magnetic flux Φ_m. The core is considered lossless, which means that the current i_0 is a pure magnetizing current. The instantaneous electromotive force of the first winding e_1 is connected to the mutual flux the following way

$$e_1 = N_1 \frac{\mathrm{d}\Phi_\mathrm{m}}{\mathrm{d}t} \tag{2.1}$$

This electromotive force e_1 is equal to the supplied voltage u_1 since the ideal transformer has no winding resistances. This link between the supplied voltage and the mutual flux means that the flux Φ_m is sinusoidal with the same frequency as u_1. The product of the number of turns N_1 and the mutual flux Φ_m is called the magnetic flux-linkage Ψ_m, which can be used for an alternative notation

$$e_1 = \frac{\mathrm{d}\Psi_\mathrm{m}}{\mathrm{d}t} \tag{2.2}$$

The flux induces a voltage e_2 in the second winding

$$e_2 = N_2 \frac{\mathrm{d}\Phi_\mathrm{m}}{\mathrm{d}t} \tag{2.3}$$

The ratio between the induced voltages a can be derived by linking Equation 2.1 and Equation 2.3

$$a = \frac{e_1}{e_2} = \frac{N_1}{N_2} \tag{2.4}$$

The next observation is conducted with the switch on the secondary winding closed. The current that is now able to flow is set up according to Lenz's law, which states that the magnetomotive force (mmf) of the secondary winding $i_2 N_2$ opposes the flux Φ_m. The induced voltage e_1 and therefore the supplied voltage u_1 remain unchanged, which means that the mutual flux Φ_m can not change. This is only possible if the primary winding draws more current to counteract the effect of Lenz's law. The current in the primary winding now consists of a magnetizing component and a load component. The magnetizing current disappears if an infinitely permeable core material is assumed, leaving only the load current. The root mean square (rms) values of the winding currents are then linked in the following way

$$I_1 N_1 = I_2 N_2 \tag{2.5}$$

The ideal transformer can thus be described with the following equations

$$\frac{E_1}{E_2} = \frac{U_1}{U_2} = \frac{N_1}{N_2} = \frac{I_2}{I_1} = a \tag{2.6}$$

2.2 Magnetic Fields of the Core Material

The explanations and figures of this section are based on [7]. The phenomenon of magnetic fields can be described with two field quantities: the magnetic field intensity $\boldsymbol{H}$ in A/m and the magnetic flux density $\boldsymbol{B}$ in T. The field intensity is associated with the movement of charge carriers, while the flux density is associated with the force on moving charge carriers. In vacuum the two field quantities are linked as follows

$$\boldsymbol{B} = \mu_0 \cdot \boldsymbol{H} \tag{2.7}$$

with $\mu_0 = 4\pi \cdot 10^{-7}$ being the vacuum permeability. This formulation has to be adapted in the following way if a material is present

$$\boldsymbol{B} = \mu_r \cdot \mu_0 \cdot \boldsymbol{H} \tag{2.8}$$

with μ_r being the relative permeability of the material. This formulation with a constant μ_r is not usable for non-linear ferromagnets. In this case a more general formulation can be used which utilizes the so-called magnetic polarization $\boldsymbol{J}$

$$\boldsymbol{B} = \mu_0 \cdot \boldsymbol{H} + \boldsymbol{J} \tag{2.9}$$

with $\boldsymbol{J}$ having the same unit as $\boldsymbol{B}$, T. An alternative formulation utilizes the so-called magnetization $\boldsymbol{M}$

$$\boldsymbol{B} = \mu_0 \cdot (\boldsymbol{H} + \boldsymbol{M}) \tag{2.10}$$

with $\boldsymbol{M}$ having the same unit as $\boldsymbol{H}$, A/m. As stated previously, the ferromagnetic core material shows a non-linear relationship between $\boldsymbol{B}$ and $\boldsymbol{H}$. This behavior can be explained with the structure of the ferromagnetic material that consists of multiple magnetic domains. A single domain contains magnetic moments that are aligned in the same direction. The entirety of the domains is formed in a way that the energy configuration is at its minimum. The magnetization process is shown in Figure 2.2 in a simplified way. Part a) shows a ferromagnetic material that consists of four magnetic domains. The domains are aligned in a way which leads the magnetizing moments of the domains to cancel each other out. Therefore, the material is in an unmagnetized state. The domain walls are not rigid but are able to move if an external magnetic field is applied to the material. This process is shown in part b) where a small external field $\boldsymbol{H}$ is applied. The domain walls move according to the direction of the applied field and the magnetic moments of the respective domains. The walls move even further as the applied field is increased, as seen in part c). The behavior at high fields is shown in part d) where the two remaining domains result in a magnetization in direction of the applied field. A further increase of the applied field leads to a rotation of the domain magnetizations, as seen in part e).

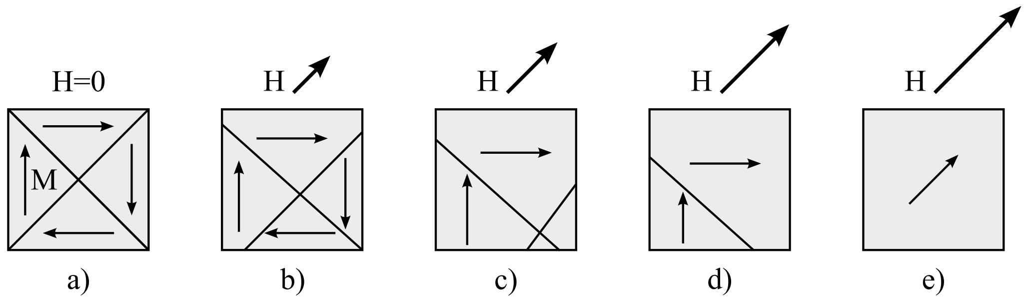

Figure 2.2: Behavior of magnetic domains [7]

The material in Figure 2.2 was ideal, meaning no defects in the material were considered. Defects limit the movement of the domain walls which causes an additional material behavior. Figure 2.3 explains how material defects influence the movement of domain walls. Part a) shows a material with two domains and six material defects depicted as circles. The domain wall is attached to the defects in the center of the material which prevent a free movement of the wall. Applying a small external field leads to the bending of the domain wall, as seen in part b). The wall, however, stays attached to the two defect sites. This type of domain wall movement is reversible, meaning that the domain wall will return to its original position (part a) if the external field disappears. The already explained rotation of the domain magnetization, seen in part d), is also a reversible magnetization process. A further increase of the external field causes the domain wall to detach from the defect sites. The domain wall is now able to move freely until it encounters further defects, as seen in part c). This domain movement is irreversible, meaning the domain wall does not return to its original position if the external field is removed.

These effects occurring in ferromagnetic materials cause the hysteretic relationship between the flux density $\boldsymbol{B}$ and the field intensity $\boldsymbol{H}$, as seen in Figure 2.4. The dashed curve represents the initial magnetization curve that occurs if the material is excited from a demagnetized state. If an external

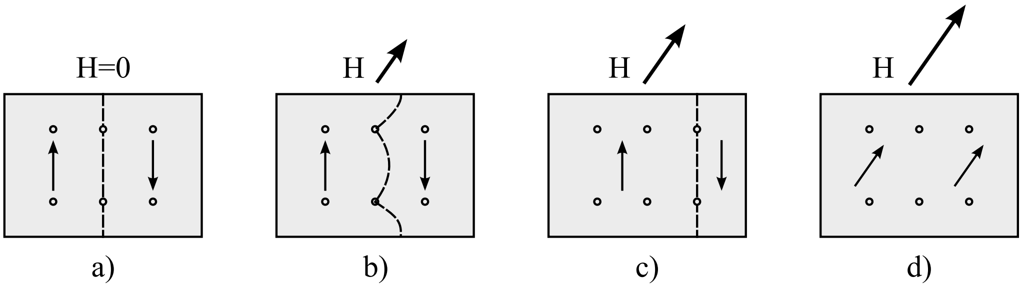

Figure 2.3: Reversible and irreversible domain movements [7]

field is applied to the material, the first domain wall movements are reversible. This corresponds to the very slow rise in the beginning of the initial magnetization curve. A rapid rise occurs as soon as the irreversible magnetization processes start to take place. The rotation, once again a reversible process, only produces a slow magnetization rise. The material starts to saturate which means that a rising $\boldsymbol{H}$ causes only a slight increase of $\boldsymbol{B}$. A decrease of $\boldsymbol{H}$ until the material enters negative saturation leads to the solid upper curve. A following increase of $\boldsymbol{H}$ leads to the solid lower curve. This means that a sinusoidal excitation leads to a counterclockwise cycle.

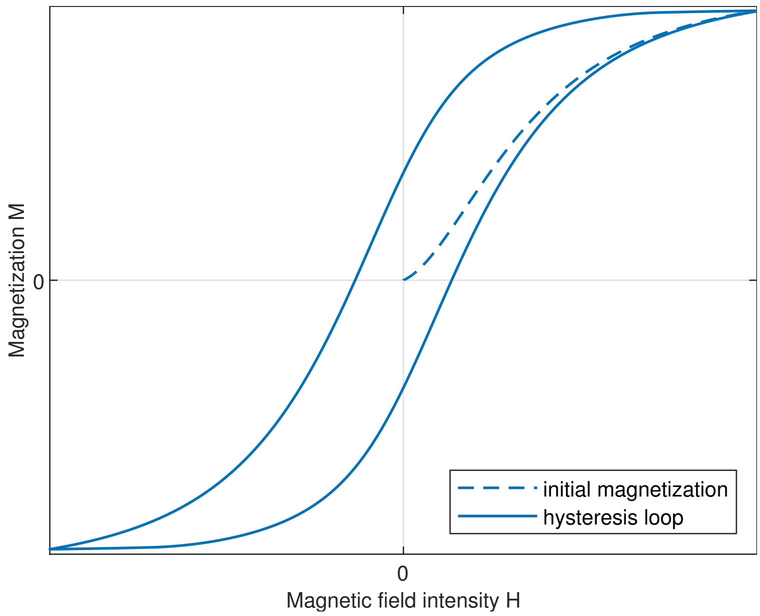

Figure 2.4: Ferromagnetic hysteresis

The hysteresis does not necessarily strictly follow the loop shown in Figure 2.4. Any magnetization process depends not only on the excitation but on the previous magnetization history as well. Some exemplary hysteresis loops are shown in Figure 2.5. The biggest possible loop is referred to as the major loop. Any loops smaller than the major loop are called minor loops, which can be symmetric or asymmetric. [8] The aforementioned effects make the prediction of the hysteresis difficult. The dashed curve in Figure 2.5, the so called anhysteretic magnetization curve, is often used as the base of hysteresis models. [8] The anhysteretic shows the thermal equilibrium state of the ferromagnetic material, which is why it was referred to as the ideal magnetization [9]. The anhysteresis and hysteresis modeling is further addressed in section 3.3.

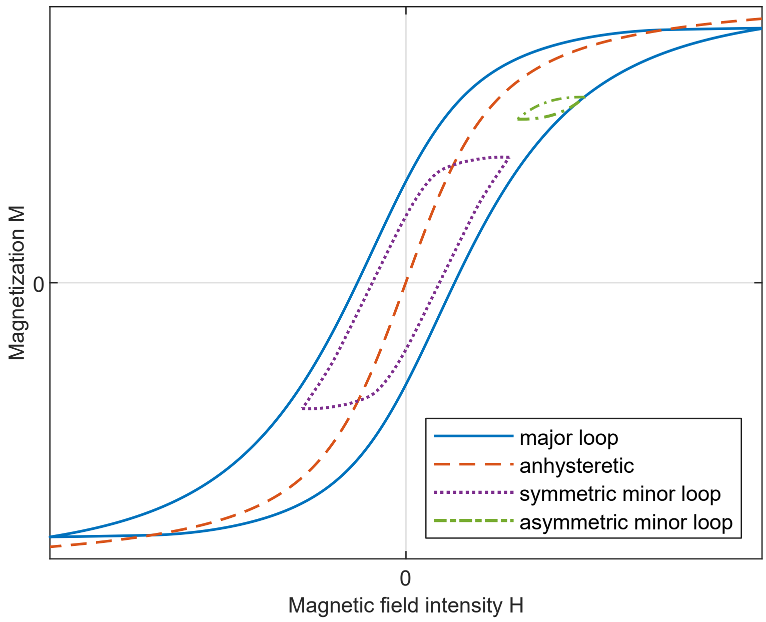

Figure 2.5: Possible hysteresis loops. Figure based on [8]

2.3 Magnetic Asymmetry of Three-Phase Transformers

It was already shown in section 2.1 that a no-load test of an ideal single-phase transformer leads to an excitation current. The current is a pure magnetizing current that sets up the required mmf which then produces the magnetic flux. A $\boldsymbol{BH}$-characteristic can be derived with the excitation current ($I \propto H$) and voltage ($U \propto B$) of the no-load test. This identification is not as straightforward in the case of three-phase transformers with all phases wound on a common core. The no-load phase currents differ from the magnetizing currents that are required for the mmf of the specific transformer limb. The same holds true for the phase powers and the true power loss of the individual transformer limbs. This discrepancy emerges because the phase currents depend on the requirements of all core sections, not just on the specific limb the winding is on. [1] [10]

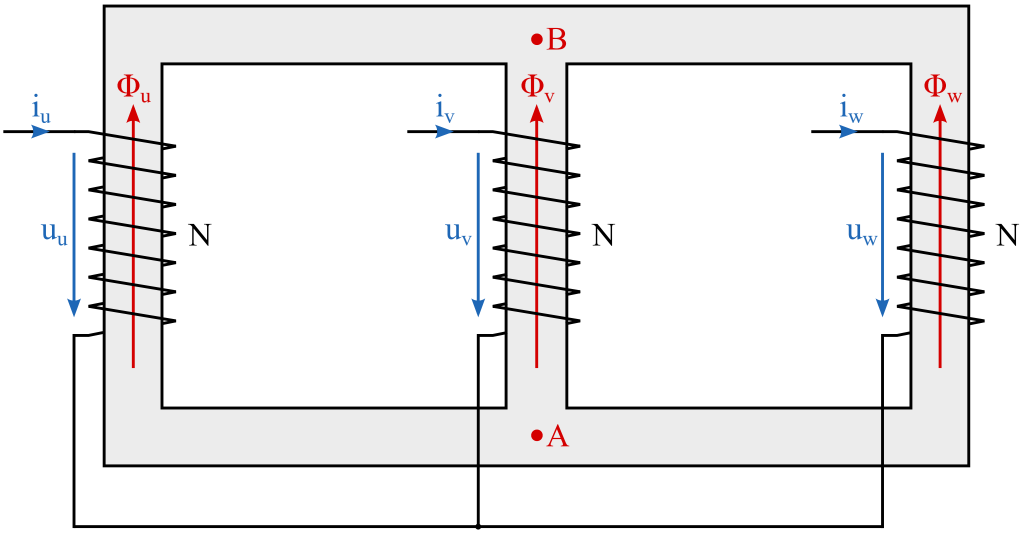

Figure 2.6: Derivation of magnetic asymmetry

This was shown in [10] for a three-limb Y-connected transformer in the following way: The investigated transformer is shown in Figure 2.6. The transformer is assumed to be ideal. All windings have the same number of turns N. The transformer is connected to a balanced, sinusoidal, three-phase voltage source. Therefore, the magnetic fluxes Φ_U, Φ_V, and Φ_W are balanced and sinusoidal too. The magnetic paths of the specific limbs start and end in the points A and B. Therefore, the middle limb has a shorter magnetic path than the two outer limbs. An mmf is required to set up the fluxes between the points A and B. In the left limb for example, an mmf of Ni'_U is required to produce the flux Φ_U. The instantaneous current i'_U represents the current that is required to set up the mmf for the left limb. As already stated, the actual phase current i_U differs from the required current i'_U. The actually produced mmf is equal to Ni_U. The actual and required mmfs of the branches can be set into relation in the following way

$$Ni_U - Ni_V = Ni'_U - Ni'_V \tag{2.11}$$

$$Ni_V - Ni_W = Ni'_V - Ni'_W \tag{2.12}$$

$$Ni_W - Ni_U = Ni'_W - Ni'_U \tag{2.13}$$

Dividing these equations by N leads to

$$i_U - i_V = i'_U - i'_V \tag{2.14}$$

$$i_{\mathrm{V}} - i_{\mathrm{W}} = i'_{\mathrm{V}} - i'_{\mathrm{W}} \tag{2.15}$$

$$i_{\mathrm{W}} - i_{\mathrm{U}} = i'_{\mathrm{W}} - i'_{\mathrm{U}} \tag{2.16}$$

One further equation is added due to the Y-connection of the transformer

$$i_{\mathrm{U}} + i_{\mathrm{V}} + i_{\mathrm{W}} = 0 \tag{2.17}$$

This set of four equations can be used to derive the following formulations of the phase currents

$$i_{\mathrm{U}} = i'_{\mathrm{U}} - \frac{1}{3}(i'_{\mathrm{U}} + i'_{\mathrm{V}} + i'_{\mathrm{W}}) \tag{2.18}$$

$$i_{\mathrm{V}} = i'_{\mathrm{V}} - \frac{1}{3}(i'_{\mathrm{U}} + i'_{\mathrm{V}} + i'_{\mathrm{W}}) \tag{2.19}$$

$$i_{\mathrm{W}} = i'_{\mathrm{W}} - \frac{1}{3}(i'_{\mathrm{U}} + i'_{\mathrm{V}} + i'_{\mathrm{W}}) \tag{2.20}$$

The derivation is shown in detail for i_{U} in Appendix A. All three currents contain the same expression which is a zero-sequence component i'_0

$$i'_0 = \frac{1}{3}(i'_{\mathrm{U}} + i'_{\mathrm{V}} + i'_{\mathrm{W}}) \tag{2.21}$$

This zero-sequence component causes an mmf Ni'_0 which, even at balanced excitation, produces a zero-sequence flux. This flux leaves the core at point A and closes itself in point B. This proves that the actual and required currents differ which means that a regular three-phase no-load test can not be used to derive the magnetization characteristic of the respective transformer limbs.

The effect of the zero-sequence current i'_0 is shown in Figure 2.7 and Figure 2.8. The left figure shows the measured ΨI-characteristics of phases U and W of a positive-sequence no-load test. The characteristics and measured power losses differ significantly even if the true $\boldsymbol{BH}$-characteristics of the two limbs are nearly identical. The right figure shows the same measurement result of a negative-sequence no-load test. The ΨI-characteristics of the phases flip if the phase sequence is changed from positive- to negative-sequence. The zero-sequence component therefore depends on the phase-sequence. A way to measure the true magnetization requirements despite the magnetic asymmetry is shown in subsection 3.4.2.

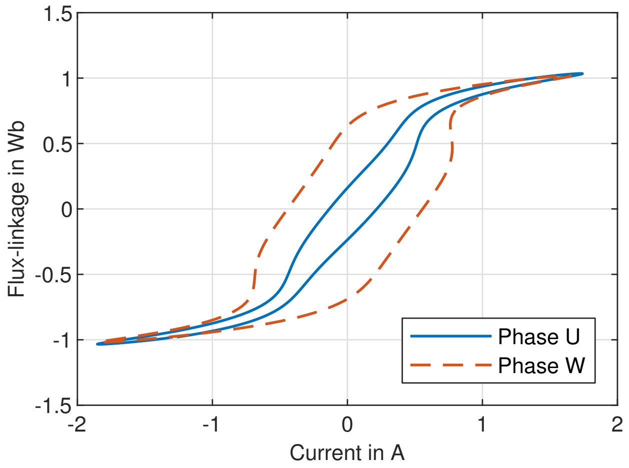

Figure 2.7: Comparison of ΨI-characteristics of phases U and W at positive-sequence

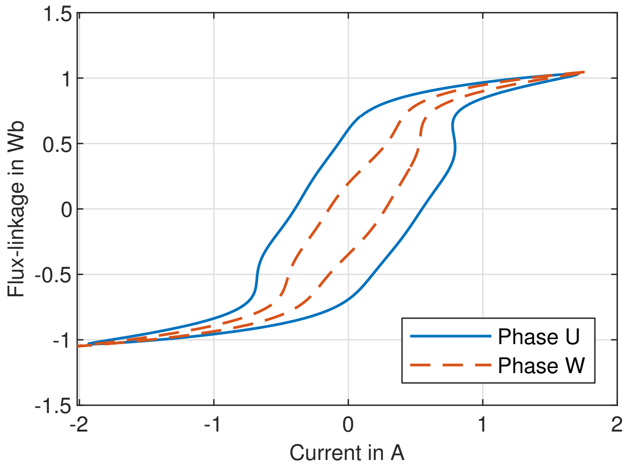

Figure 2.8: Comparison of ΨI-characteristics of phases U and W at negative sequence

3 Theory and Methods

3.1 Transformer Modeling for Low Frequencies

The complexity of transformers makes their modeling a difficult task. The various materials used in transformers have different frequency-dependent behaviors. The core effects have to be considered when the investigated transients have frequencies below a few kHz. The core can, however, be neglected at higher frequencies, while skin and proximity effects of the windings become dominant. Therefore, the modeling approach depends on the investigated frequency range. [1]

The frequency ranges of transients can be categorized according to [11] in the following way:

- 0.1 Hz - 3 kHz: low-frequency oscillations
- 50/60 Hz - 20 kHz: slow front surges
- 10 kHz - 3 MHz: fast front surges
- 100 kHz - 50 MHz: very fast front surges

Low-frequency transients in transformers include geomagnetically induced currents (GICs), ferroresonance, harmonic currents, and inrush currents [5]. The core and winding representation do not just depend on the frequency range but on the investigated tests as well. As an example, the core can be neglected in short-circuit tests, while it is important in the simulation of ferroresonance. Therefore, the core and winding representation can be viewed separately. [12]

According to [12], low-frequency models can be categorized into three groups:

1. Matrix representation
2. Saturable transformer component (STC)
3. Topology-based models

One approach of the first group is the use of an admittance matrix to represent the transformer

$$[I] = [Y] \cdot [U] \tag{3.1}$$

This model does not include the non-linearity of the core since the admittance matrix consists of the measured short-circuit test results. [12]

The drawback of the missing non-linearity is overcome in the STC-model. This approach adds the non-linearity in the form of a non-linear inductor at the star point [12]. Figure 3.1 shows a single-phase three-winding STC-model. The non-physical location of the single magnetization branch, however, can lead to numerical instabilities [2]. This can be overcome by the use of a topologically-correct model.

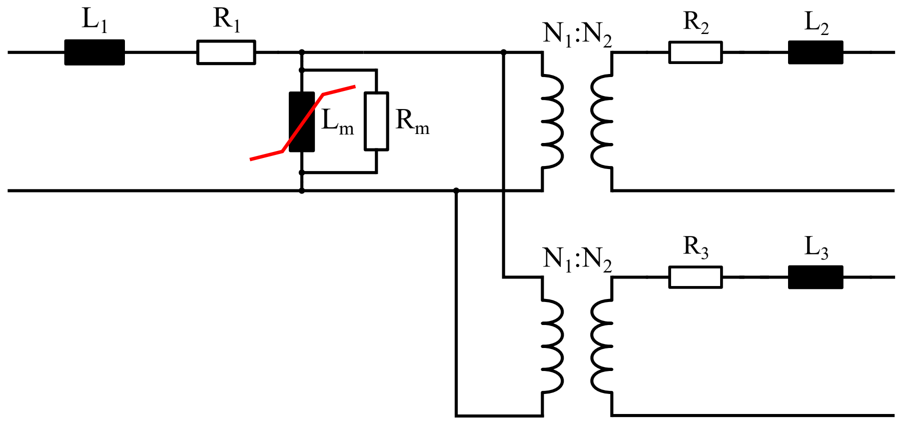

Figure 3.1: Single-phase three-winding STC-model. Figure based on [12]

3.1.1 Topology-Based Models

This group of models is derived from the core topology of the investigated transformer. One example are duality-based models, where a magnetic circuit of the transformer is converted into an equivalent electric circuit using the principle of duality. These transformer models reproduce each core element individually instead of grouping them into one single magnetizing branch as in the STC-model. Therefore, saturation effects are modeled in each core element separately. [12]
Another advantage of this approach is the consideration of magnetic coupling between phases. The use of a single-phase representation for a three-phase transformer lacks magnetic coupling, leading to inaccurate results in unbalanced operations. [4]

Duality-based models lack a detailed leakage model which lead to the development of hybrid transformer models. Such models combine the topologically correct core model with a matrix representation of the leakage inductances [13]. The hybrid model separates core and leakage representation under the assumption that core inductances are greater than leakage inductances. This can lead to doubtful results at deep saturation where this assumption does not hold. [14]
The magnetic coupling and the representation of every core element are important in the study of GICs, therefore, a topology-based model based on the principle of duality is developed in this thesis. The approach of modeling a three-limb, three-phase transformer is explained in section 3.2.

3.2 Duality-Based Three-Limb Transformer Model

The magnetic circuit of a transformer can be converted into an equivalent electric circuit using the physically correct duality approach. This allows the transformer to be simulated using only standard circuit elements. [2] Another advantage in this special case is that power system engineers are more used to work in the electric rather than the magnetic domain. A duality-based model of a three-phase, three-limb transformer with two concentric windings, as seen in Figure 3.2, is derived in this section. The principle of duality, first introduced for transformers in [15], requires a planar network. This means that a drawing of the circuit on a flat surface is not allowed to have intersecting branches. A planar graph is necessary and sufficient for the derivation of a dual circuit [16]. Transformers with more than three windings have a non-planar magnetic circuit and therefore, an equivalent electric circuit cannot be simply derived by the principle of duality [15]. The transformer shown in Figure 3.2 has only two windings which means that duality can be applied.

First, a magnetic circuit has to be created by approximating the magnetic field into flux tubes. The detail level of this approximation is crucial for the model's accuracy. [17]

Figure 3.3 shows the left limb and the attached yokes of the investigated three-limb transformer. Two magnetic nodes are placed on either end of the limb. The magnetic field is approximated into a main flux through the core (solid), a leakage flux between core and first winding (dashed), another leakage flux between the two windings (dashed), and a zero-sequence flux outside of the windings (dotted). A more detailed division of the magnetic field is possible, however, this approach is a reasonable compromise between required data and accuracy [18].

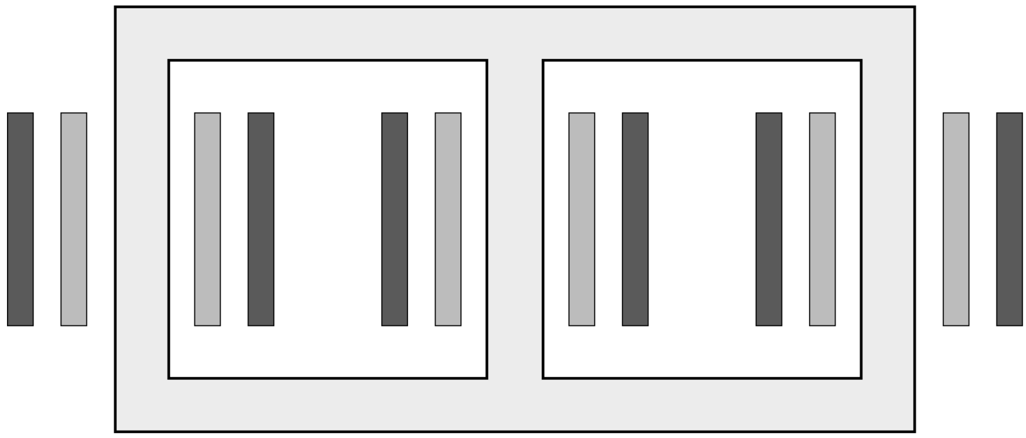

Figure 3.2: Three-phase, three-limb, two-winding transformer

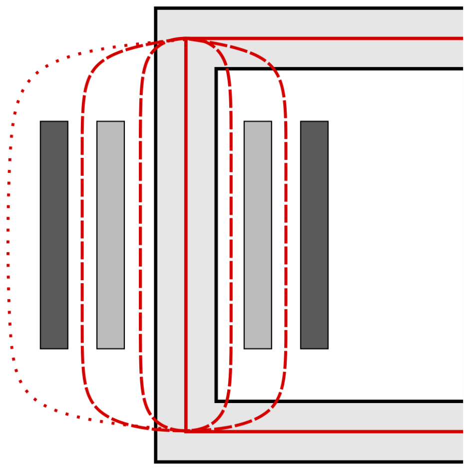

Figure 3.3: Main flux paths of one limb

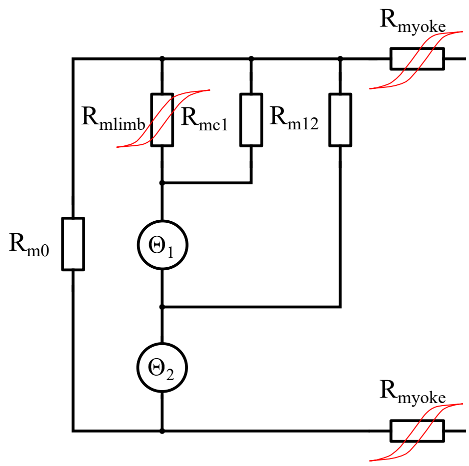

Figure 3.4: Magnetic circuit of one limb

The flux tubes can then be converted into a magnetic circuit, with the windings being represented by mmf-sources and the flux tubes by reluctances. Figure 3.4 shows the resulting magnetic circuit. The hysteretic reluctances R_{mlimb} and R_{myoke}, which represent the individual core sections, are drawn with a superimposed hysteresis. The linear reluctances R_{mc1} and R_{m12} represent the leakage fluxes. The zero-sequence flux is represented by the linear reluctance R_{m0}.

The second step is the derivation of the equivalent electric circuit. This can be done graphically by placing a dot into every loop of the magnetic circuit and an additional reference point outside of the circuit. In the duality approach the nodes/loops of one circuit turn into the loops/nodes of the other one. The drawn dots represent the nodes of the equivalent electric circuit. [15] Neighboring nodes are connected with lines which cross each element of the magnetic circuit. These lines represent the branches of the electric circuit. This process is shown in Figure 3.5 for the left limb of the

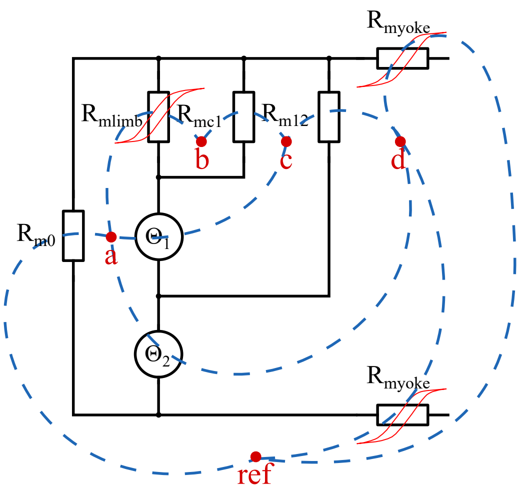

Figure 3.5: Derivation of the dual electric network

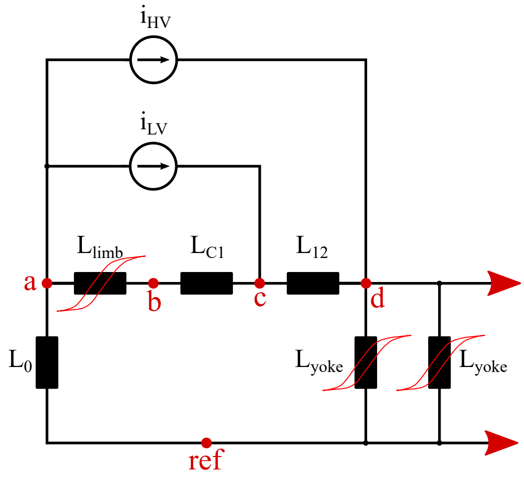

Figure 3.6: Equivalent electric circuit of one limb

transformer. The connections to the middle limb are not shown in the figure. According to [15], the mmf and the flux rate of change of the magnetic circuit are dual to the current and voltage of the electric circuit. This means that the mmf sources and reluctances in the magnetic domain are replaced by current sources and inductances in the electric domain. This leads to the equivalent electric circuit shown in Figure 3.6. The two arrows symbolize the connection to the middle limb.

Another limitation of the principle of duality is the requirement of equal turns. This can be overcome by replacing the current sources with ideal transformers [15]. The equivalent circuit is independent of the vector group, since the winding connections are realized outside of the ideal transformers [19]. A capacitive network for the improvement of the model's accuracy at higher frequencies and the winding resistances can be added outside of the ideal transformers as well [18]. The model in this thesis merely implements the winding resistances as shown in the final electric circuit of the three-limb transformer in Figure 3.7. The parameter estimation for this transformer model is detailed in section 3.4.

3.3 Iron Core Modeling

The traditional way of modeling core elements with a non-linear inductor and a parallel constant resistor is limited in its accuracy regarding the voltage- and frequency-dependent core behavior. The constant resistor is usually adapted to fit the losses at nominal voltage. This leads to an inaccurate loss representation at excitations other than the nominal voltage. The accuracy can be improved by

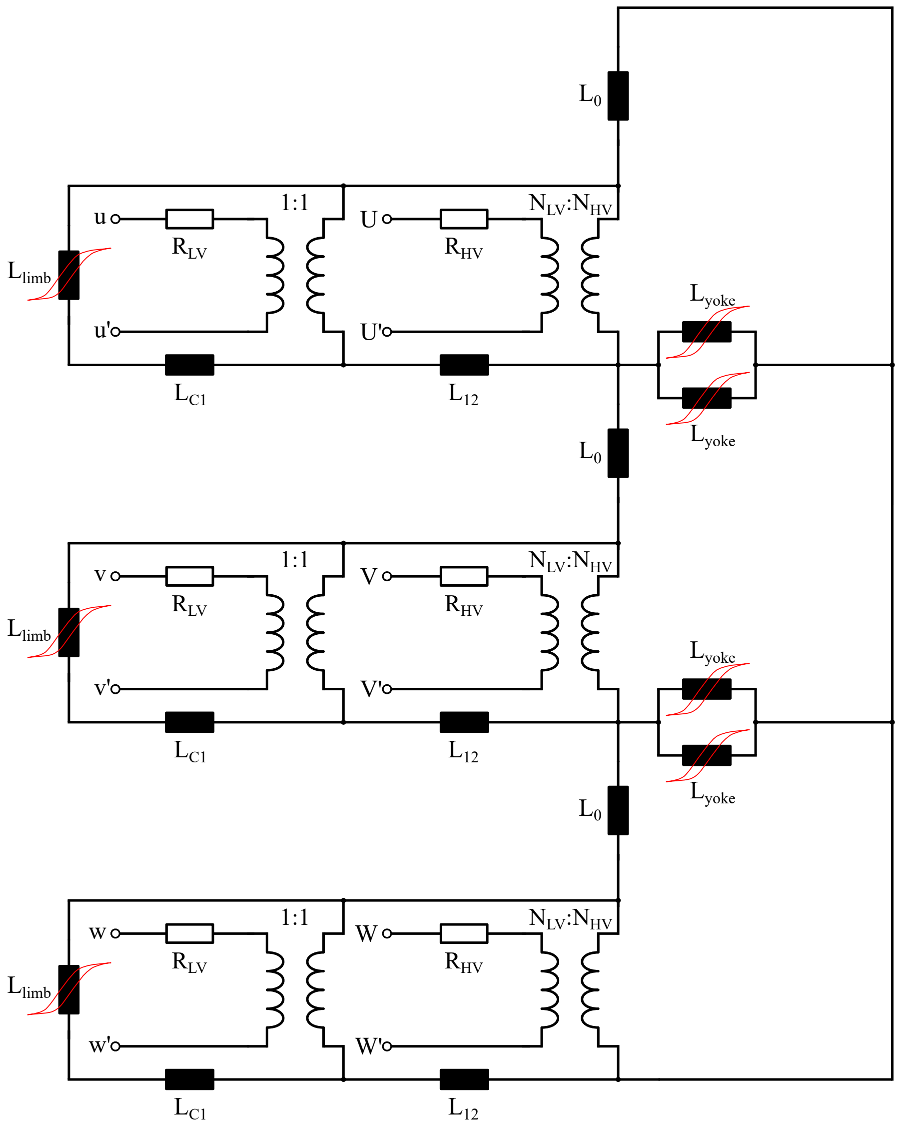

Figure 3.7: Equivalent electric circuit of the transformer

replacing the constant resistor with a non-linear one. This does not, however, solve the inaccurate frequency-dependent representation. A hysteresis model is much better suited to represent the voltage- and frequency-dependent core losses. [4]

One approach to represent hysteresis is the group of macroscopic models. This group uses mathematical expressions to describe the hysteresis phenomenon on a macroscopic scale without completely neglecting material physics [20]. The big advantage over the more detailed models used by physicists is that they are not as computational time-consuming [8]. Therefore, a macroscopic approach is chosen for this transformer model. The core loss can be divided into static and dynamic loss components. Thus, hysteresis modeling is separated into a static and dynamic model.

3.3.1 Static Hysteresis Modeling – Jiles-Atherton Model

A static hysteresis model has to replicate the major and symmetrical/asymmetrical minor loops [8]. Two of the best-known static hysteresis models are the Preisach- and the Jiles-Atherton (JA)-model. A good introduction into the models is given in [8]. A comparison of the two approaches in [21] concludes that Preisach is more accurate especially at producing minor loops but also more computationally intensive. It is also stated that Preisach requires extensive measurements but little fitting while the opposite is true for JA.

Less measurements are a big advantage of the JA-model in the case of power transformers that are in use. Quicker and simpler measurements lead to shorter downtimes in which the transformer has to be disconnected from the grid. This is the main reason why the JA-model is used for the representation of static hysteresis losses in this transformer model.

Multiple mathematical descriptions of the model with slight differences can be found. The main idea, however, stays the same. The description in this section is based on [22], while the formulas show a slightly modified version of the model found in [23]. For more detailed explanations see [22] and [23]. The often-mentioned physical basis of the model has to be viewed critically if a physically correct representation is important. According to [24] it is in fact non-physical, however, the model is still useful in circuit simulations.

The JA-model uses the anhysteretic magnetization and combines it with pinning sites that represent defects in the material. The model creates sigmoid-shaped hysteresis loops by considering the influence of pinning sites on domain wall motions. The energy of a ferromagnetic solid is viewed to derive a formula for the anhysteretic magnetization. The energy per unit volume of an isotropic domain can be expressed as follows

$$E = -\mu_0 \boldsymbol{m} \cdot \boldsymbol{H} \tag{3.2}$$

with $\boldsymbol{m}$ being the magnetic moment per unit volume and $\boldsymbol{H}$ being the internal magnetic field intensity. A ferromagnetic solid consists of multiple coupled domains. The coupling between magnetic domains is represented by the product of the bulk magnetization $\boldsymbol{M}$ with a factor α

$$E = -\mu_0 \boldsymbol{m} \cdot (\boldsymbol{H} + \alpha \boldsymbol{M}) \tag{3.3}$$

The mean-field parameter α expresses the interdomain coupling. The resulting field is termed the effective field intensity $\boldsymbol{H}_\mathrm{e}$

$$\boldsymbol{H}_\mathrm{e} = \boldsymbol{H} + \alpha \boldsymbol{M} \tag{3.4}$$

This effective field intensity can be used to derive a magnetization. At this point only the coupling between domains is considered. No pinning has been incorporated yet which means the material is ideal. The expression is only valid for the ferromagnetic material in its global equilibrium state. This state is equivalent to the anhysteretic magnetization $\boldsymbol{M}_\mathrm{an}$. The relation of $\boldsymbol{M}_\mathrm{an}$ and $\boldsymbol{H}_\mathrm{e}$ can be simplified as

$$\boldsymbol{M}_\mathrm{an} = M_\mathrm{s} \cdot f(\boldsymbol{H}_\mathrm{e}) \tag{3.5}$$

where f is a function that is zero when $\boldsymbol{H}_\mathrm{e}$ is zero and converges to one when $\boldsymbol{H}_\mathrm{e}$ approaches infinity. Any function that fulfills these conditions can be used. The following function for $\boldsymbol{M}_\mathrm{an}$ is given in [22]

$$M_\mathrm{an}(H_\mathrm{e}) = M_\mathrm{s} \left(\coth\left(\frac{H_\mathrm{e}}{a}\right) - \left(\frac{a}{H_\mathrm{e}}\right) \right) \tag{3.6}$$

The function Equation 3.6 includes a new parameter a, which influences the curve shape. Figure 3.8 and Figure 3.9 show how the anhysteretic magnetization calculated with Equation 3.6 is influenced when the values of a and M_s are varied.

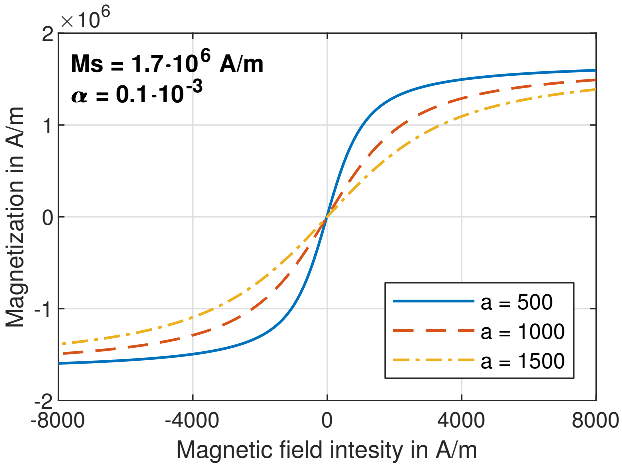

Figure 3.8: Variation of a

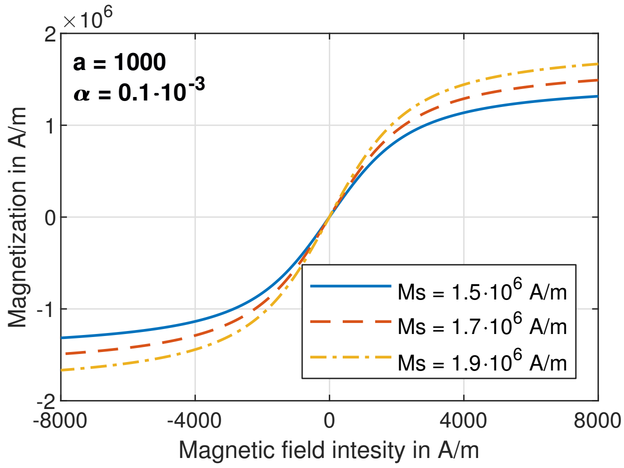

Figure 3.9: Variation of M_s

The defects found in real materials interfere with domain wall motions, causing the hysteretic behavior of the material. An example of the interfering defect sites can be shown with the initial magnetization curve of a previously demagnetized ferromagnetic material. The initial magnetization curve always lies below the ideal anhysteretic magnetization curve because the defect sites oppose the movement of the domain walls. The JA-model takes two types of domain wall movements into account: domain wall displacement and domain wall bulging. Domain wall displacement causes an irreversible magnetization change, meaning the domain wall will stay in its position if the magnetic field is removed. The magnetization change caused by the bulging of domain walls is reversible. The JA-model expresses the magnetization M as the sum of an irreversible and a reversible component

$$M = M_{\text{irr}} + M_{\text{rev}} \tag{3.7}$$

The irreversible component is examined first. For this it is assumed that the domain wall is perfectly rigid. It will not bulge, it can only be displaced. As already mentioned, the domain walls become pinned at defect sites. The achieved magnetization can therefore be described as the ideal anhysteretic minus a component representing the loss due to the pinning of the material. The coefficient k is introduced to describe this behavior

$$M_{\text{irr}} = M_{\text{an}} - \delta k \left(\frac{\mathrm{d}M_{\text{irr}}}{\mathrm{d}H_{\text{e}}} \right) \tag{3.8}$$

The parameter δ ensures that the influence of the domain wall pinning opposes the change of magnetization. It is +1 when $\mathrm{d}H/\mathrm{d}t > 0$ and -1 when $\mathrm{d}H/\mathrm{d}t < 0$. Appendix B shows the process of

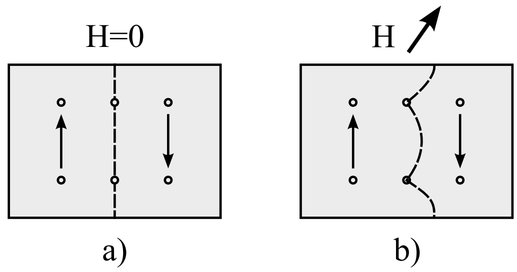

Figure 3.10: Domain wall bulging [7]

how Equation 3.8 is rewritten into its final form

$$\frac{\mathrm{d}M_{\mathrm{irr}}}{\mathrm{d}H} = \frac{M_{\mathrm{an}} - M_{\mathrm{irr}}}{\delta k - \alpha(M_{\mathrm{an}} - M_{\mathrm{irr}})} \tag{3.9}$$

However, domain walls are not rigid but flexible. The reversibility can be explained using Figure 3.10. It shows an unflexed domain wall that is pinned on two defect sites. The pinning is not immediately overcome by an increasing magnetic field. The domain wall flexes, causing a reversible magnetization change. The flexing continues until the domain wall breaks free from the current pinning sites. The reversibility is implemented once again using the anhysteretic magnetization M_{an}. The domain walls are assumed to be unflexed at the anhysteretic magnetization. Therefore, the sign of the reversible component depends on the difference between anhysteretic M_{an} and magnetization M, or alternatively between the anhysteretic M_{an} and the irreversible magnetization M_{irr}. The relation can be simplified resulting in a single coefficient c which represents how much the domain walls flex before breaking free.

$$M_{\mathrm{rev}} = c(M_{\mathrm{an}} - M_{\mathrm{irr}}) \tag{3.10}$$

This leads to the reversible component of the JA-model

$$\frac{\mathrm{d}M_{\mathrm{rev}}}{\mathrm{d}H} = c\left(\frac{\mathrm{d}M_{\mathrm{an}}}{\mathrm{d}H} - \frac{\mathrm{d}M_{\mathrm{irr}}}{\mathrm{d}H}\right) \tag{3.11}$$

The irreversible (Equation 3.9) and the reversible component (Equation 3.11) can then be combined to derive the final mathematical description of the JA-model. The derivation is shown in Appendix C.

$$\frac{\mathrm{d}M}{\mathrm{d}H} = (1-c)\frac{M_{\mathrm{an}} - M_{\mathrm{irr}}}{k\delta - \alpha(M_{\mathrm{an}} - M_{\mathrm{irr}})} + c\frac{\mathrm{d}M_{\mathrm{an}}}{\mathrm{d}H} \tag{3.12}$$

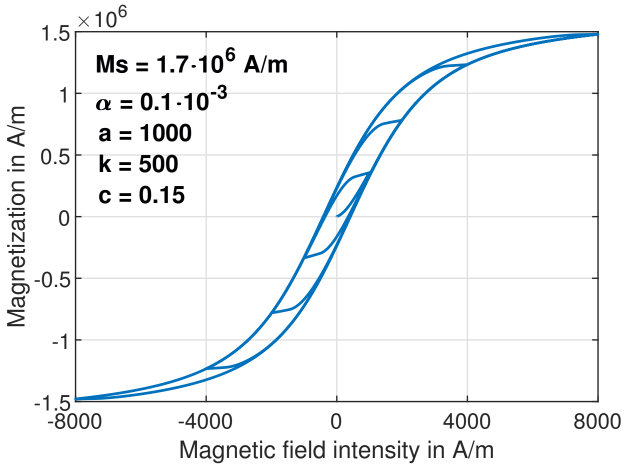

Figure 3.11: Major and minor loops constructed using the JA-model

The classic JA-model using Equation 3.6 as a function for the anhysteretic magnetization contains five parameters α, a, M_s, k, and c. A short description of the parameters is shown in Table 3.1. Figure 3.11 shows an example of major and minor loops generated with Equation 3.12.

Table 3.1: JA parameters and physical link

Parameter	Description
α	represents interdomain coupling
a	shapes the anhysteretic curve
M_s	saturation magnetization
k	represents hysteresis losses
c	represents the reversibility

There are multiple approaches for the estimation of the five parameters. The knowledge of how the parameters influence the hysteresis shape can be used to roughly fit the parameters by hand. The influence of the parameters a and M_s on the anhysteretic magnetization calculated with Equation 3.6 was already shown in Figure 3.8 and Figure 3.9. The influence of the parameters α, k, and c is shown in Figure 3.12 - Figure 3.14. In these figures only one hysteresis with an increased parameter value is compared to the major loop from Figure 3.11. This was merely done to heighten visibility. A decrease of the respective parameter values obviously results in the opposite effects.

An iterative identification process based on measurements of only one hysteresis loop was first introduced in [23]. This method does not always converge, therefore mathematical optimization

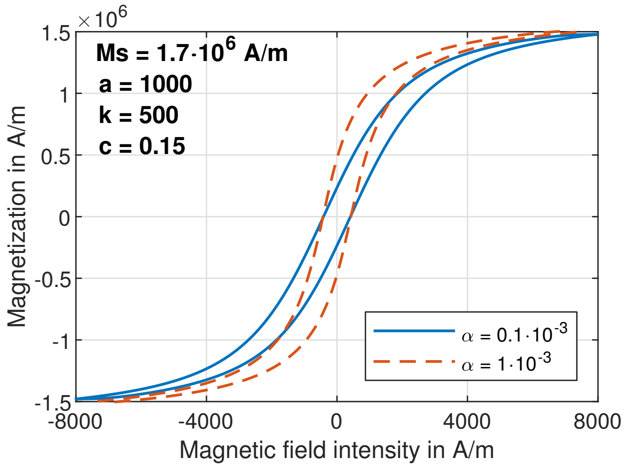

Figure 3.12: Variation of α

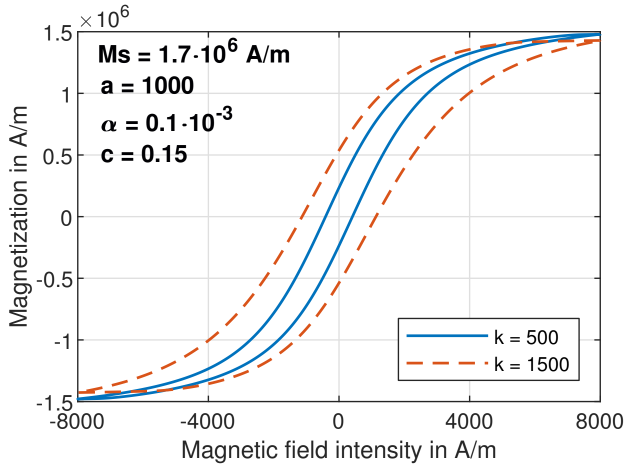

Figure 3.13: Variation of k

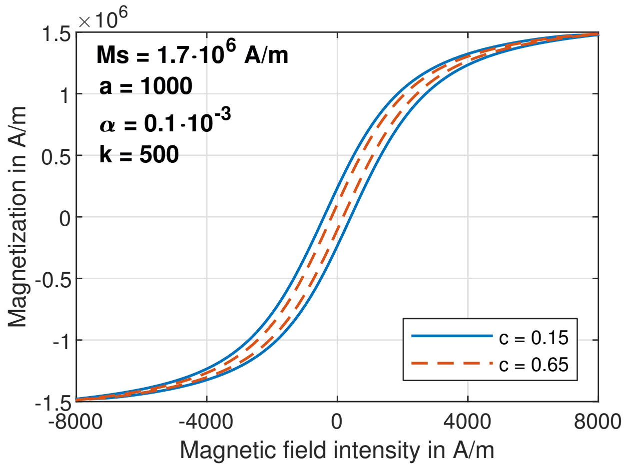

Figure 3.14: Variation of c

techniques are used to overcome this limitation and to improve the accuracy. One example of an optimization approach is found in [25].

Multiple improvements and modifications of the classic JA-model exist. One modification prevents non-physical behavior of the model that can occur at the loop tips as explained in [23]. The hysteresis in the first quadrant is observed to explain the non-physical behavior. The magnetization M approaches the anhysteresis M_{an} as the magnetic field intensity H is increased. When the magnetic field intensity H is reduced, the magnetization M is reduced too. The flexed domain walls relax at first while still staying pinned. This means that the wall motion is mostly reversible until the domain walls become unflexed, which is the case at the anhysteretic magnetization. The model, however, can calculate an irreversible component in this situation as well. [23] To overcome this problem another parameter δ_{M} can be implemented as stated in [26]

$$\delta_{\mathrm{M}} = \begin{cases} 0 & \text{if } H < 0 \text{ and } M_{\mathrm{an}} - M > 0 \\ 0 & \text{if } H > 0 \text{ and } M_{\mathrm{an}} - M < 0 \\ 1 & \text{otherwise} \end{cases} \tag{3.13}$$

The multiplication of this parameter with Equation 3.9 ensures that the irreversible component is set to zero under these circumstances to prevent the non-physical behavior.
A modification that can be useful in some cases is the inverse JA-model. The classic approach uses the magnetic field intensity H as an input, while the inverse uses the magnetic flux density B. The approach used in this thesis is based on the inverse time-stepping JA-model found in [27], which was enhanced by the implementation of Equation 3.13. The implemented JA-model can be found in Appendix D.

The function for M_{an} given in Equation 3.6 can be exchanged if a higher adjustability is needed. Equation 3.14, proposed in [28], can give a more accurate model.

$$M_{\mathrm{an}} = M_{\mathrm{s}} \frac{a_1 H_{\mathrm{e}} + {H_{\mathrm{e}}}^b}{a_3 + a_2 H_{\mathrm{e}} + {H_{\mathrm{e}}}^b} \tag{3.14}$$

This equation can be used if the following constraints apply

$$a_1 > 0, \quad a_2 \geqslant a_1, \quad a_3 > 0, \quad \text{and} \quad b \geqslant 1.0 \tag{3.15}$$

As stated before, the JA-model generates sigmoid-shaped hysteresis loops. Grain-orientated steels used in transformers, however, have loops that widen at the shoulder and are therefore different from the uniformly converging sigmoid-shape [29]. The accuracy can be increased by modifying the constant parameter k to be dependent on the magnetization M, since the width depends on the parameter k [28].

The accuracy of minor loops can be improved by either introducing scaling factors or by determining the parameters for different excitations. The use of a scaling factor only requires the measurement of the major loop. Multiple loops at different excitations are necessary if separate sets of parameters are used. [25]

3.3.2 Dynamic Hysteresis Losses

The Hysteresis losses can be split into static and dynamic components. In fact, the total energy loss W_{tot} can be split into three components: a static hysteresis loss component W_{hys}, an eddy loss component W_{eddy}, and an excess loss component W_{exc} [30].

$$W_{\mathrm{tot}} = W_{\mathrm{hys}} + W_{\mathrm{eddy}} + W_{\mathrm{exc}} \tag{3.16}$$

The total loss can not be described accurately with only a static and an eddy loss component. The eddy loss component, which is calculated with a Maxwell equation, assumes a homogeneous magnetic material. This is because the Maxwell equation predates the knowledge of magnetic domains. The dynamic effect caused by the domains is considered in the excess loss component W_{exc}. [29]

The two dynamic components exhibit different frequency-dependent behaviors [30]

$$\begin{aligned} W_{\mathrm{eddy}} &\propto f \\ W_{\mathrm{exc}} &\propto f^{1/2} \end{aligned} \tag{3.17}$$

Figure 3.15, which is based on a figure from [6], shows the frequency-dependent hysteresis loss and possible hysteresis loss models. The shown modeling approaches are fitted to correctly represent the energy loss at nominal frequency f_{n}. The classic approach of an inductor in combination with a loss resistor disregards the static and excess components. It underestimates the loss below f_{n} and overestimates loss above f_{n}. A better approach is to use a static model to represent the static losses in combination with a loss resistor. Following [29], this approach will be referred to as the two-component dynamic model. This approach, while more accurate, still underestimates the loss below f_{n} and overestimates it above f_{n} because it disregards excess eddy loss. Furthermore, the loss is voltage-dependent. The use of a two-component dynamic model leads to a slight overestimation below and significant underestimation above nominal voltage [5]. The frequency-dependent loss behavior can only be modeled accurately if all three components of Equation 3.16 are considered. Following [29], this approach will be referred to as the three-component dynamic model.

The separation principle in Equation 3.16 can also be applied to the magnetic field intensity leading to the following expression [30]

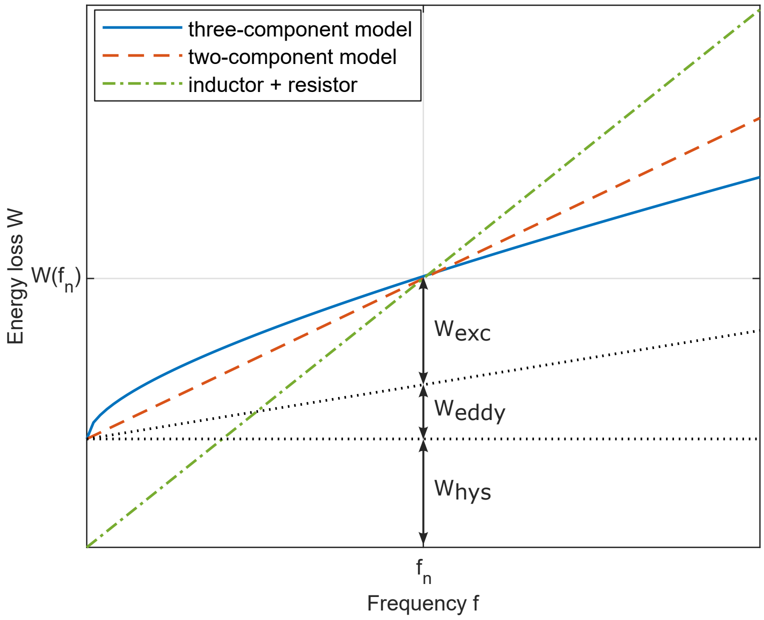

Figure 3.15: frequency-dependent model accuracy. Figure is modified based on [6]

$$H_{\text{tot}} = H_{\text{hys}} + H_{\text{eddy}} + H_{\text{exc}} \tag{3.18}$$

The dynamic model can be implemented with a two- or three-component approach based on Equation 3.18. The three-component dynamic model can be implemented as follows [31], [29]

$$H_{\text{tot}} = H_{\text{hys}} + k_{\text{eddy}} \frac{\mathrm{d}B}{\mathrm{d}t} + k_{\text{exc}} \delta \left| \frac{\mathrm{d}B}{\mathrm{d}t} \right|^{\frac{1}{2}} \tag{3.19}$$

with δ being +1 for $\mathrm{d}B/\mathrm{d}t > 0$ and -1 for $\mathrm{d}B/\mathrm{d}t < 0$. The static component H_{hys} is calculated by the inverse JA-model. The complexity of the complete model depends on the required accuracy and the available data. The static JA hysteresis model can be improved and modified in various ways, as the examples given in subsection 3.3.1 show. The parameter k_{exc} can be constant [31] or dependent on B in order to improve the voltage-dependent accuracy [29].

3.4 Parameter Derivation

The parameter derivation process consists of numerous different measurement and fitting procedures. The linear parameters and can either be derived by standard tests or can be found in factory test protocols. The linear components of the transformer model are:

- Winding resistances R_{LV} and R_{HV}
- Short-circuit inductance L_{12} between the two windings
- Inductance L_{C1} between core and first winding
- Zero-sequence impedance L_0

The non-linear core parameters require measurements and data beyond the standard tests.

3.4.1 Linear Parameters

The winding resistances can be measured using a direct current (DC) source according to the standard [32]. The frequency-dependence of the winding resistance, mainly caused by the skin and proximity effect, can be incorporated [13]. The model in this thesis, however, only includes the DC winding resistances.

The linear inductance L_{12} representing the flux between the two windings can be calculated from a short-circuit test according to the standard [32].

The inductance L_{C1} can not be measured directly but can be approximated based on L_{12} [14]

$$L_{\mathrm{C1}} \approx K \cdot L_{12} \tag{3.20}$$

with $K = 0.5$ giving good results [14].

The zero-sequence inductance can be derived from zero-sequence measurements according to the standard [32]. Depending on the winding connection the zero-sequence flux may flow partly through the tank which is non-linear. This occurs in transformers with missing winding balancing ampere-turns, as is the case for Yy-transformers without an additional delta winding [32]. The non-linearity can safely be neglected according to [14], where a duality-based model is applied to simulate a 300 kVA Yyn-transformer. This is explained with the linear behavior of the oil gap between core and tank which outweighs the non-linear behavior of the tank. More detailed models that include the non-linear tank as well as other structural components are possible, however, the parameter estimation is not trivial [5].

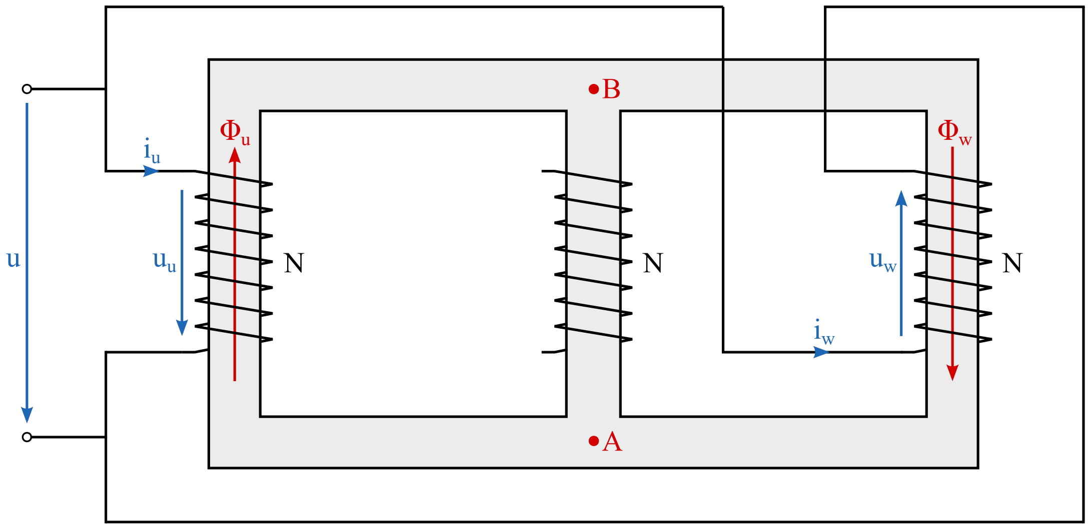

Figure 3.16: Measurement of core properties [10]

3.4.2 Non-Linear Core Parameters

As stated in chapter 2, the phase currents of a regular three-phase no-load test do not just depend on the properties of their respective core section but on the other sections as well. Therefore, the magnetic properties can not be deduced from a three-phase no-load test. Figure 3.16 shows an approach found in [10] to measure the required excitations of two core sections without the interference of the third. An ideal transformer without leakage flux and winding resistances is assumed to explain the method. A sinusoidal voltage is applied to windings U and W. The magnetic fluxes in the outer limbs will be equal, since the voltage is applied to both windings. This means that there is no magnetic flux and mmf in the middle limb. The mmf set up in the left limb is consumed to create the magnetic flux in the same section. Therefore, the drawn current of winding U is the actual current needed to excite the left limb of the core. The same applies to the right limb and winding W. In reality a small flux will occur in the middle limb. Nevertheless, this approach allows to measure the voltage-current and therefore the flux-current properties of the core sections. [10]

An alternative method is shown in Figure 3.17. This gives the disadvantage of measuring the sum of both excitation currents instead of the separate currents related to the individual core sections. Yet, this method was used in this thesis because it required less modifications of the preexisting laboratory set-up.

The measurement for the derivation of JA-parameters should be performed at low frequencies in

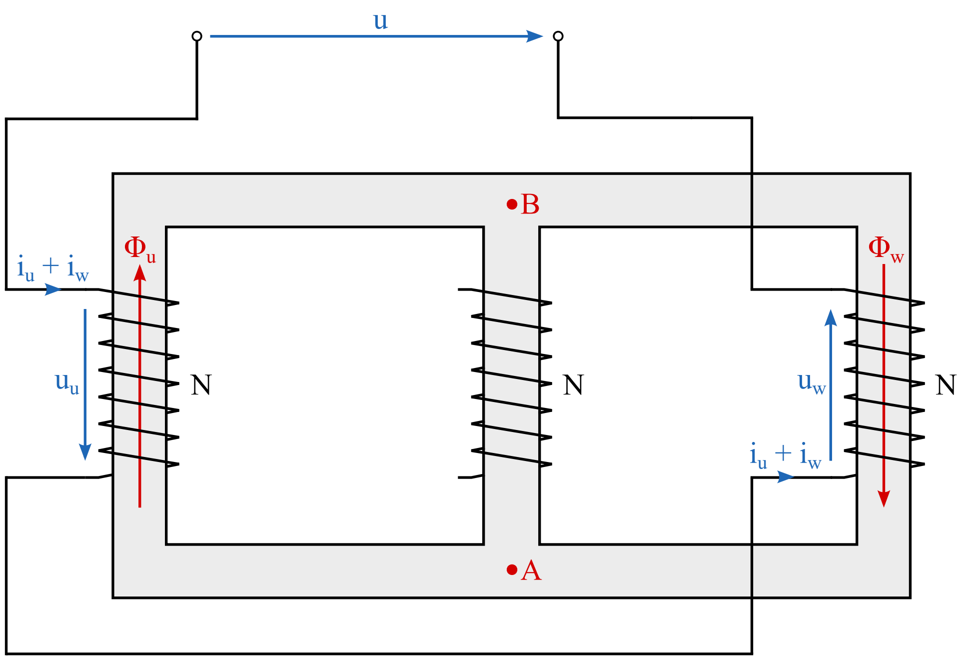

Figure 3.17: Realized measurement of core properties

order to minimize dynamic effects. A welcome side effect of a lowered frequency is that a lower voltage amplitude is required to reach the same flux amplitude. Thus, the measurements can be possible with portable measuring devices. [33]

A method for the derivation of the dynamic loss components of a 3 kVA single-phase transformer is shown in [31]. Hysteresis measurements at various frequencies were conducted and resulted in wider loops as the frequency was increased. It is safe to assume that the 3 kVA transformer used in [31] does not have a tank, which would increase the capacitive behavior at higher frequencies. The same method might not be applicable to power transformers as considerable capacitive effects of the tank might occur at higher frequencies. This effect is shown in Figure 3.18 for a 50 kVA power transformer. Two minor loops at 5 Hz and 50 Hz are compared to each other. The use of minor loops makes the effect more noticeable. The phase shift, caused by the capacitance, rotates the 50 Hz hysteresis loop counterclockwise in comparison to the 5 Hz loop. This renders the results useless. Additionally, such a measurement might not be possible for large power transformers outside of laboratory settings, since a higher frequency requires a higher voltage amplitude to reach the same flux as in the low-frequency measurement. Portable measuring devices might not be able to supply a high enough voltage amplitude. The fitting of the dynamic hysteresis parameters can therefore only be realized with power loss measurements, such as no-load tests at rated frequency.

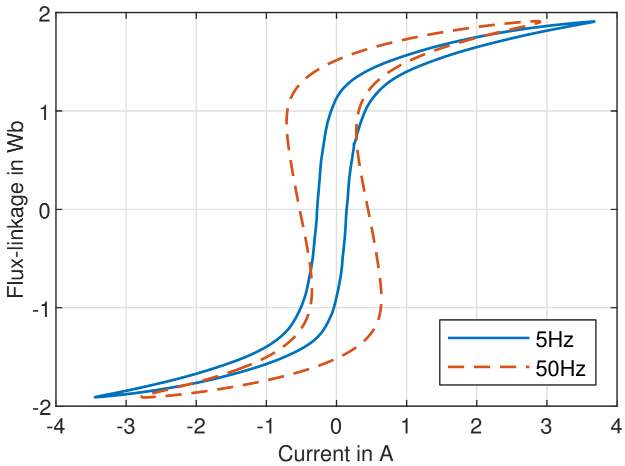

Figure 3.18: Hysteresis measurements at different frequencies

4 Measurements and Fitting

4.1 Transformer Under Test (T74) – General Data

The transformer model from chapter 3 is tested on a three-phase, three-limb, two-winding, 50 kVA power transformer. The topology of the transformer matches the topology of the transformer in Figure 3.2. Table 4.1 shows the relevant nameplate data. The transformer, built in 1974, will hereafter be referred to as T74.

The transformer has been modified in a way that allows the low-voltage winding connection to be chosen at will [34]. All of the following measurements and simulations are based on the transformer in YNyn0 connection. The deviation of the nameplate winding connection entails a deviation of the voltage amplitude. If the YNyn0-transformer is excited with 400 V from the low-voltage side, the voltage on the high-voltage side is less than the rated voltage U_{HV} given in Table 4.1. The number of low- and high-voltage winding turns are needed to properly represent the voltage ratio independent of the chosen winding connection. Another requirement are the core dimensions. If the exact core dimensions are not known, typical ratios for the specific core type can be used instead of the exact dimensions [35]. In the case of the T74, however, all dimensions are known. Table 4.2 contains the geometric data and number of turns of the T74. The given lengths correspond to the mean lengths of the main magnetic flux paths as shown in Figure 4.1.

Table 4.1: Relevant nameplate data

Type	f	U_{LV}	U_{HV}	I_{LV}	I_{HV}
-	Hz	V	V	A	A
Yzn5	50	400	35000	72.1	0.842

Table 4.2: Geometric transformer data

A_{core}	l_{yoke}	l_{limb}	N_{LV}	N_{HV}
mm^2	mm	mm	-	-
6001	237	440	102	7730

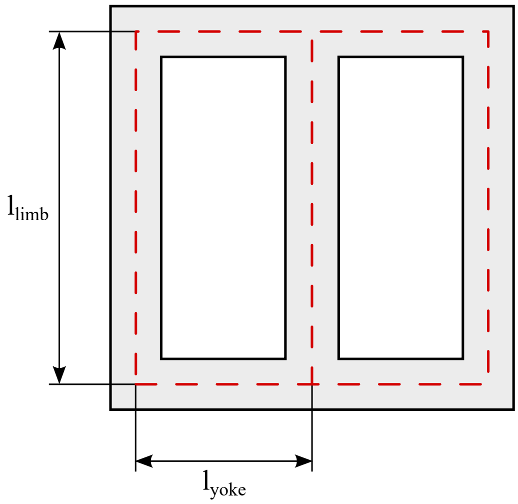

Figure 4.1: T74 core dimensions

4.2 T74 - Linear Parameters

The derivation of the linear components is performed as explained in subsection 3.4.1. It is assumed that there are no differences among the phases. The parameters of the individual phases are therefore assumed to be equal. All measurements were performed on the low-voltage side of the transformer.

The first step are the DC winding resistances. The values of the resistances of the low-voltage winding R_{LV} and the high-voltage winding R_{HV} were measured previously and were provided for this thesis.

The inductance L_{12} is calculated using a short-circuit test. Table 4.3 contains the rms values of phase voltages and currents as well as the power factors of each phase. The mean values of phase voltages, phase currents and power factors are calculated with Equation 4.1 to Equation 4.3.

$$\overline{U_{\mathrm{SC}}} = \frac{U_{\mathrm{U,SC}} \cdot U_{\mathrm{V,SC}} \cdot U_{\mathrm{W,SC}}}{3} = \frac{17.590\ \mathrm{V} \cdot 18.361\ \mathrm{V} \cdot 17.557\ \mathrm{V}}{3} = 17.836\ \mathrm{V} \tag{4.1}$$

Table 4.3: Short-circuit test data

$U_{U,SC}$	$U_{V,SC}$	$U_{W,SC}$	$I_{U,SC}$	$I_{V,SC}$	$I_{W,SC}$	$\cos(\varphi_U)$	$\cos(\varphi_V)$	$\cos(\varphi_W)$
V	V	V	A	A	A	-	-	-
17.590	18.361	17.557	70.352	65.458	70.910	0.482	0.509	0.426

$$\overline{I_{SC}} = \frac{I_{U,SC} \cdot I_{V,SC} \cdot I_{W,SC}}{3} = \frac{70.352\ \text{A} \cdot 65.458\ \text{A} \cdot 70.910\ \text{A}}{3} = 68.901\ \text{A} \tag{4.2}$$

$$\overline{\cos(\varphi)} = \frac{\cos(\varphi_U) \cdot \cos(\varphi_V) \cdot \cos(\varphi_W)}{3} = \frac{0.482 \cdot 0.509 \cdot 0.426}{3} = 0.472 \tag{4.3}$$

The mean values can then be used to calculate the short-circuit impedance L_{12}

$$X_{12} = \frac{\overline{U_{SC}}}{\overline{I_{SC}}} \cdot \overline{\sin(\varphi)} = \frac{17.836\ \text{V}}{68.901\ \text{A}} \cdot \sin(61.836^\circ) = 0.228\ \Omega \tag{4.4}$$

$$L_{12} = \frac{X_{12}}{2 \cdot \pi \cdot f_n} = \frac{0.228\ \Omega}{2 \cdot \pi \cdot 50\ \text{Hz}} = 726\ \mu\text{H} \tag{4.5}$$

The inductance L_{C1} can be approximated according to Equation 3.20 with $K = 0.5$ [14]

$$L_{C1} \approx K \cdot L_{12} = 0.5 \cdot 726\ \mu\text{H} = 363\ \mu\text{H} \tag{4.6}$$

As explained in subsection 3.4.1, the zero-sequence inductance can be assumed to be linear. An open-circuit zero-sequence test conducted on the T74 transformer confirmed the near linear behavior at the test current of 23.5 A per phase. A higher test current was not possible due to the current limitation of the neutral connection. Table 4.4 contains the rms values of the conducted zero-sequence test. The current I_{zero} is the total current of all three phases combined. The supplied voltage was adjusted by subtracting the voltage drop across the winding, leading to U_{zero}. The zero-sequence impedance X_0 per phase is then calculated according to [32].

$$Z_0 = \frac{3 \cdot U_{zero}}{I_{zero}} = \frac{3 \cdot 52.73\ \text{V}}{70.50\ \text{A}} = 2.244\ \Omega \tag{4.7}$$

Table 4.4: Main transformer under test (T74) zero-sequence test data

U_{zero}	I_{zero}	S_{zero}	P_{zero}	Q_{zero}
V	A	VA	W	var
52.73	70.50	3784.81	2224.66	3061.97

Table 4.5: T74 linear parameters

R_{LV}	R_{HV}	L_{12}	L_{C1}	L_0	R_0
Ω	Ω	µH	µH	mH	Ω
0.041	332.058	726	363	8.671	3.749

The impedance can be split into an inductance and a parallel resistance which represents the losses

$$X_0 = \frac{3 \cdot U_{zero}^2}{Q_{zero}} = \frac{3 \cdot (52.73\ \mathrm{V})^2}{3061.97\ \mathrm{var}} = 2.724\ \Omega \tag{4.8}$$

$$L_0 = \frac{X_0}{2 \cdot \pi \cdot f_n} = \frac{2.724\ \Omega}{2 \cdot \pi \cdot\ 50\ \mathrm{Hz}} = 8.671\ \mathrm{mH} \tag{4.9}$$

$$R_0 = \frac{3 \cdot U_{zero}^2}{P_{zero}} = \frac{3 \cdot (52.73\ \mathrm{V})^2}{2224.66\ \mathrm{W}} = 3.749\ \Omega \tag{4.10}$$

The linear parameters of the T74 model are summarized in Table 4.5.

4.3 T74 - Non-Linear Core Parameters

The measurements of the static hysteresis losses were conducted with the measuring setup shown in Figure 3.17. A power-amplifier capable of supplying near perfect sinusoidal voltages with constant amplitudes was used for all measurements. The simulations, that use ideal voltage sources, are therefore comparable to the measurements. All measurements were conducted with a measuring device that measures the overall power, not just the fundamental power. The simulated powers were therefore derived in the same way as with the measuring device. The used formulas are shown in

Appendix E. A frequency of 5 Hz was used to minimize dynamic effects for the measurement of the static hysteresis losses. A positive side effect of low frequencies is caused by the proportionality seen in Equation 4.11. If the frequency is lowered, the voltage amplitude has to be lowered too for the flux amplitude to remain unchanged. Lower voltage amplitudes make the measurement possible with portable alternating current (AC) sources. Alternatively, specialized test-devices can have the ability to output DC-voltages to measure the core characteristics. Appendix F compares the measurement with the AC power-amplifier to a measurement with a not yet released testing software of a specialized transformer test-device using DC-excitation.

$$\Phi_{\text{peak}} \propto \frac{U_{\text{peak}}}{f} \tag{4.11}$$

The supplied voltages are integrated to obtain the flux linkage Ψ. The relation between flux-linkage Ψ and measured current I can then be used to analyze the core behavior. Figure 4.2 shows a comparison of the ΨI-characteristics measured between the phases UW, UV and VW. The measurement shows only slight differences between the phases. Therefore, only one characteristic is used to derive the JA-parameters for all core sections. The parameters of individual core sections can be adjusted later if necessary.

The measured response between phases U and W was chosen arbitrarily to fit the parameters. Figure 4.3 shows loops measured between phases U and W at 5 Hz and various excitations.

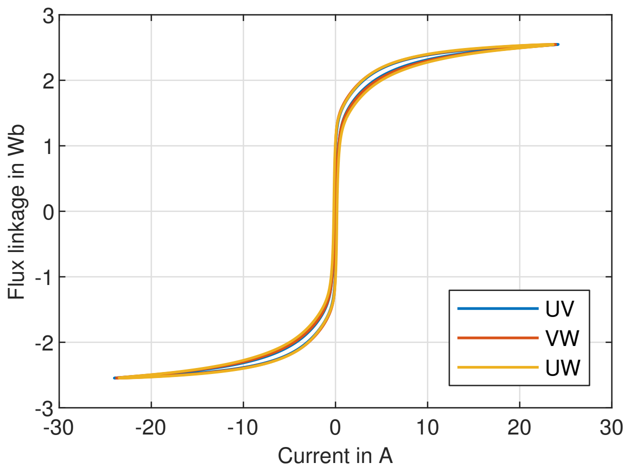

Figure 4.2: Comparison of ΨI-characteristics measured between different phases

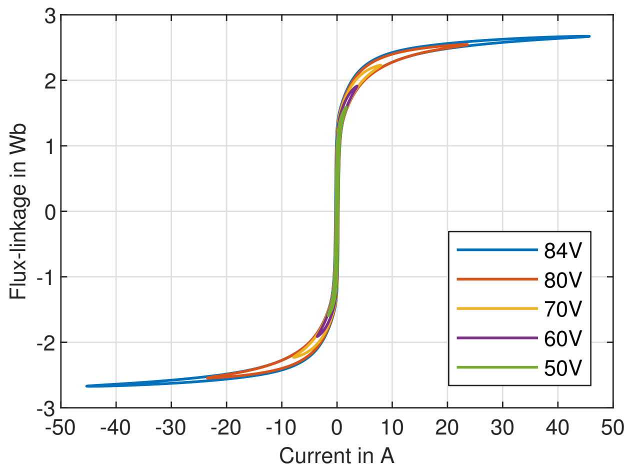

Figure 4.3: Comparison of ΨI-characteristics measured between phases U and W at different excitations

Only one major loop is needed to implement the JA-model in its original form shown in subsection 3.3.1. The parameters are fitted by recreating the measurement setup (Figure 3.17) in the simulation model. The simulated ΨI-characteristic can then be compared to the measured characteristic. The arbitrary chosen initial JA-parameters were modified by hand using the knowledge of how the parameters influence the shape of the hysteresis (subsection 3.3.1). Figure 4.4 shows the measured 80 V ΨI-characteristic that was used to fit the parameters. It can be seen clearly that the measured loop in Figure 4.4 deviates from the classic sigmoid-shaped hysteresis loop which the JA-model was developed for. The hysteresis widens noticeably at higher excitation. The same behavior is observed in the measurement with the specialized transformer test-device seen in Appendix F. A similar loop shape was measured on 350 MVA transformer built in 1971 [36]. The similar age of the transformers used in this thesis (1974) and in [36] (1971) suggests that the shape is caused by the core material of that time period. Therefore, a measuring error can be excluded.

The widening of the loop makes a good fit of the JA-parameters difficult, since a constant k is used. Adapting the JA-parameters to fit the width at lower excitation leads to poor performance at higher excitation and vice versa. The performance at nominal and therefore lower excitation was deemed as more important than the performance at high saturation. A set of parameters fitted to the 84 V measurement did not deliver satisfactory results at lower excitation voltages. A set of parameters fitted to the measurement at 80 V lead to a much improved accuracy at lower voltages while delivering a poor simulation when simulating the 84 V test. Nevertheless, the parameters derived from the 80 V test were preferred, considering the improved accuracy at nominal excitation.

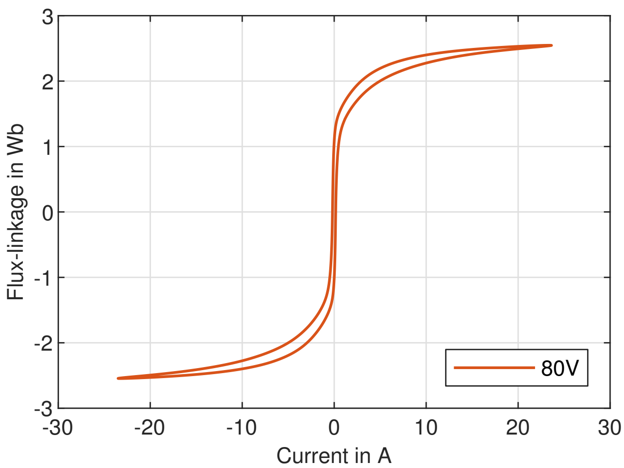

Figure 4.4: ΨI-characteristic between phases U and W at 80 V

Table 4.6: T74 JA-parameters

α	a	M_s	k	c
-	-	A/m	A/m	A/m
$0.20 \cdot 10^{-3}$	120	$1.75 \cdot 10^{6}$	15	0.15

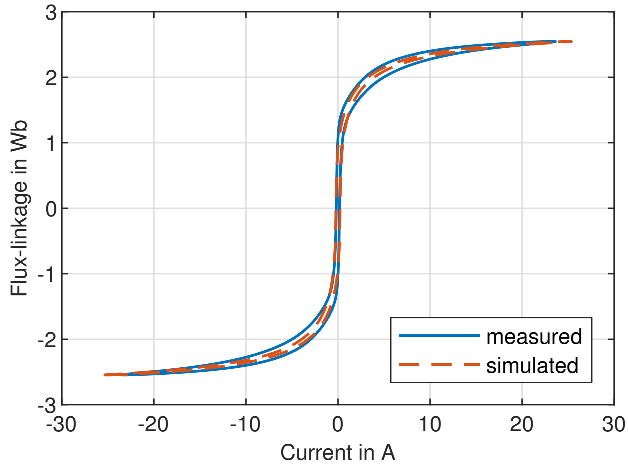

Figure 4.5: Comparison of ΨI-characteristics between phases U and W at 80 V

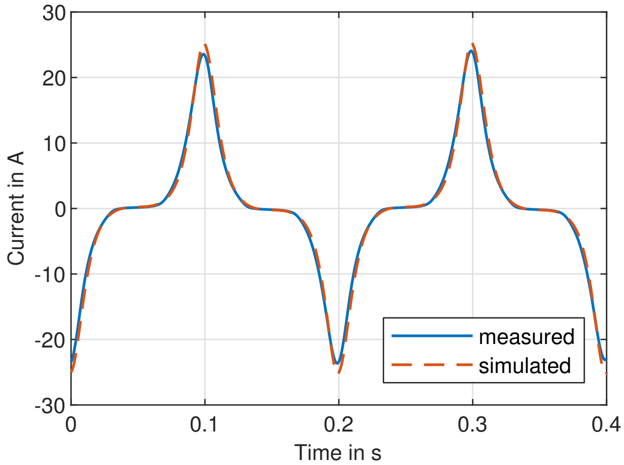

Figure 4.6: Comparison of currents between phases U and W at 80 V

Figure 4.5 shows how the simulation using the parameters in Table 4.6 compares to the measurement at 80 V. As already mentioned, the measured loop widens as it starts to saturate. The simulation yields a much narrower loop at saturation, which leads to a underrepresentation of active power loss. The active and reactive power loss of all executed tests are summarized in Table 4.7. The measured and simulated currents at 80 V are compared in Figure 4.6. The simulated current is slightly overestimated at the peaks. Apart from that, the currents are in good agreement.

Figure 4.7 shows how a simulation at 50 V with the parameters in Table 4.6 compares to the measurement. While not perfect, the parameters deliver results at an acceptable accuracy. The measured ΨI-loop does not yet widen as it approaches the loop tips. This leads to a more accurate recreation of the loop areas and therefore the loss is in much better agreement as seen in Table 4.7. The simulated current, while it recreates the general shape of the measured one, is slightly lower at the peak as seen in Figure 4.8. The same observations apply to the test at 60 V, as shown in Figure 4.9 and Figure 4.10.

A divide between the measured and simulated ΨI-loops can be seen in Figure 4.11. It can clearly be

Table 4.7: Measured and simulated powers of the 1-phase test

U V	P_{meas} W	Q_{meas} var	S_{meas} VA	P_{sim} W	Q_{sim} var	S_{sim} VA
50	6.15	28.18	28.84	7.18	26.51	27.47
60	9.84	74.41	75.06	8.72	63.34	63.93
70	16.54	182.51	183.26	10.56	163.29	163.63
80	32.65	549.26	550.23	16.56	577.68	577.92
84	49.96	1027.47	1028.69	37.87	1419.11	1419.61

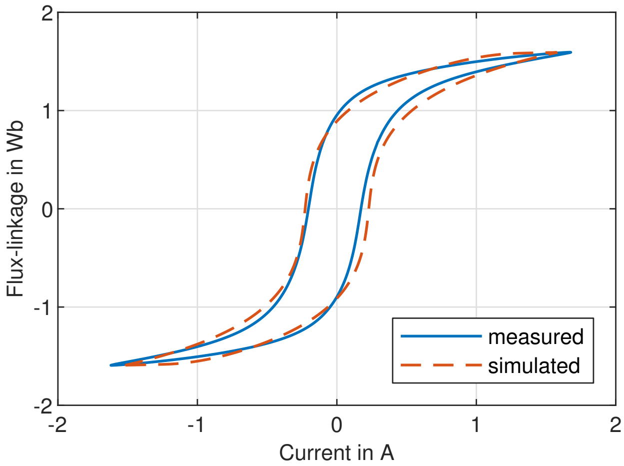

Figure 4.7: Comparison of ΨI-characteristics between phases U and W at 50 V

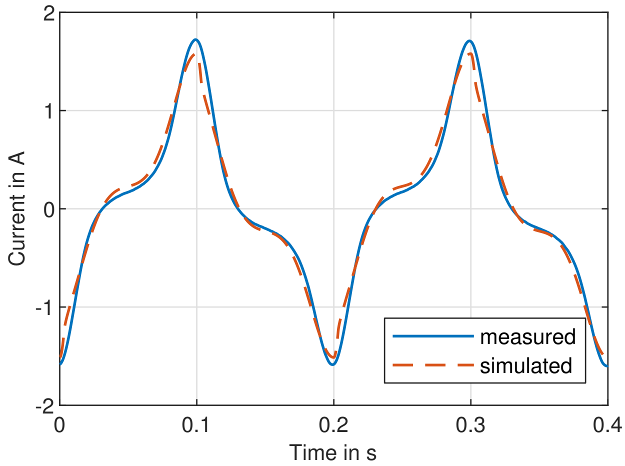

Figure 4.8: Comparison of currents between phases U and W at 50 V

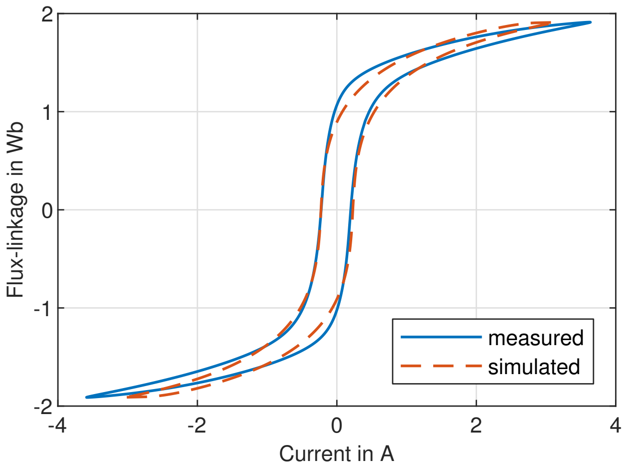

Figure 4.9: Comparison of ΨI-characteristics between phases U and W at 60 V

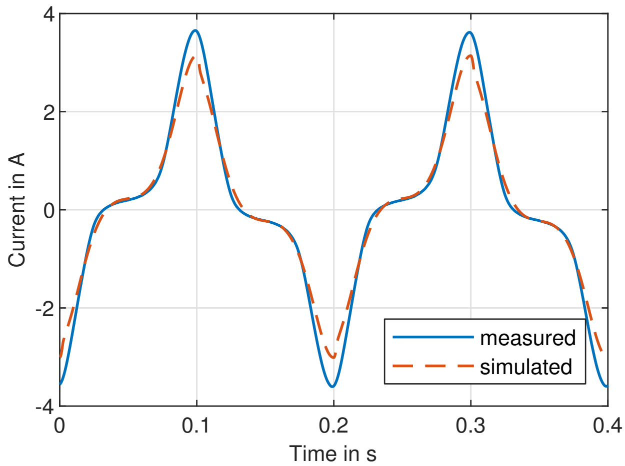

Figure 4.10: Comparison of currents between phases U and W at 60 V

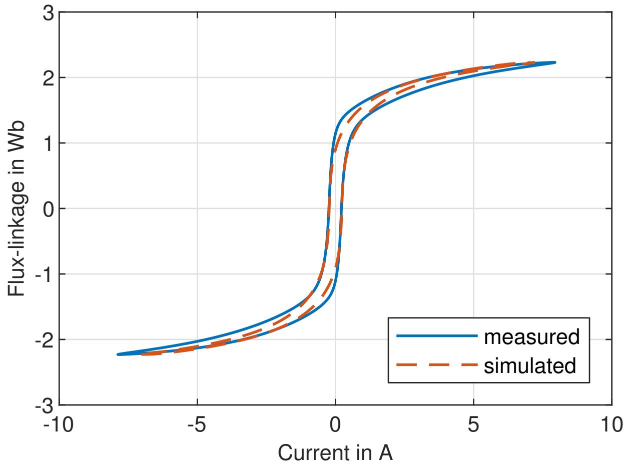

Figure 4.11: Comparison of ΨI-characteristics between phases U and W at 70 V

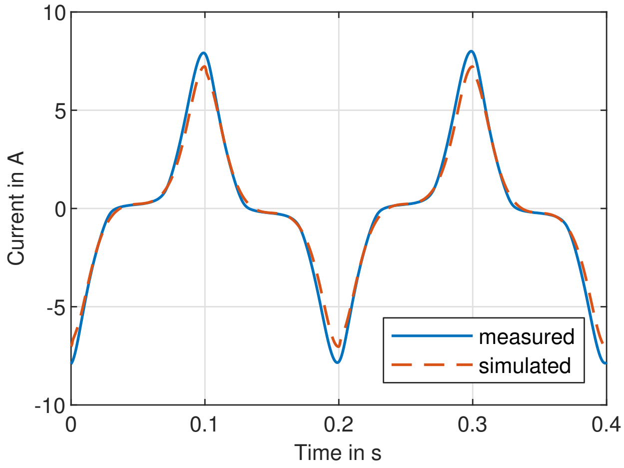

Figure 4.12: Comparison of currents between phases U and W at 70 V

seen that the measured loop starts to widen as it starts to saturate. This divide can also be seen in Table 4.7, where the measured and simulated active power loss differ significantly at 70 V. The current comparison in Figure 4.12 shows a slight underestimation of the simulated current peak.

The measured ΨI-characteristics of the different phase connections do not differ significantly, as already shown in Figure 4.2. Be that as it may, slight differences can still result in unsatisfactory results of individual phases. Ideally, the identified parameters in Table 4.6 would be compared to a low-frequency three-phase no-load test. The response of every phase could then be compared to the simulation. Differences that may arise between phases could then be eliminated with adjustments to the JA-parameter of the affected core sections. In the case of the T74, however, such a test results in long transient oscillations. Such a measurement requires a long measuring duration. Furthermore, this measurement might not be feasible for large power transformers outside of laboratory settings.

Another obstacle is the identification of the dynamic hysteresis losses, as already explained in subsection 3.4.2. This in combination with the not perfect implementation of the static hysteresis loss lead to the conclusion that the more accurate three-component dynamic model is unreasonable. Therefore, only the eddy component is implemented in the form of a resistance in parallel to the JA-components.

The JA-parameter adjustment of the individual limbs and the addition of the dynamic loss resistance is conducted using a single three-phase no-load test at rated frequency. Figure 4.13 to Figure 4.15

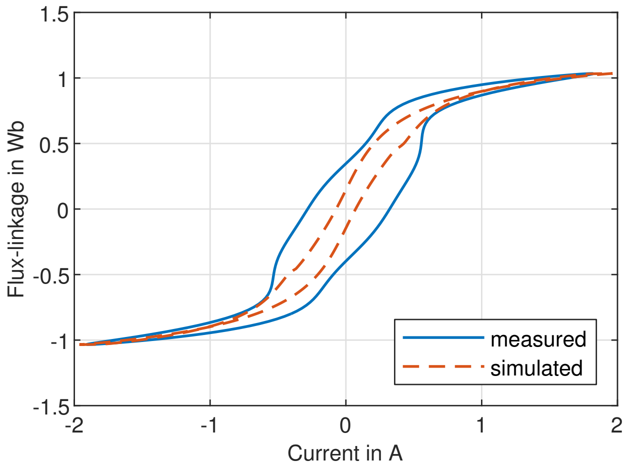

Figure 4.13: ΨI-characteristics of phase U with identical JA-parameters

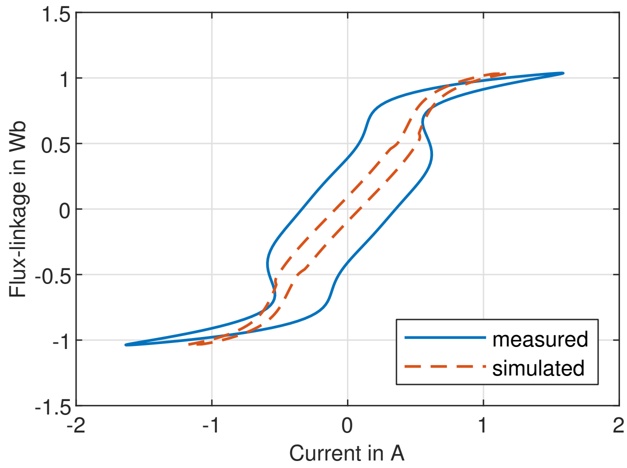

Figure 4.14: ΨI-characteristics of phase V with identical JA-parameters

show the comparison between the measured and simulated ΨI-characteristics of the three phases. The different loop widths are caused by the magnetic asymmetry, as explained in section 2.3. It is obvious that the simulated loops differ from the measured loops, since no dynamic hysteresis loss is incorporated yet. Therefore, the simulation yields narrower loops. The simulated curve in Figure 4.13, while it may look like a regular loop, has flipped upward and downward curves. This means that the lower curve represents a negative change of magnetization, while the upper curve represents a positive change of magnetization. The two curves cross at high saturation. This behavior is caused by the magnetic asymmetry, since all core sections simulate the identical hysteresis loop in Figure 4.16.

The first step is to ensure that the amplitudes of the simulated phase currents match the measured current amplitudes. Figure 4.14 shows that the simulation yields too low current amplitudes in phase V. This can be corrected by lowering the M_s-parameter of the middle limb from $1.75 \cdot 10^6$ A/m to $1.63 \cdot 10^6$ A/m. This adjustment causes the middle limb to saturate at a lower excitation. The α-parameter was increased from $0.20 \cdot 10^{-3}$ to $0.24 \cdot 10^{-3}$ which causes the loop to slightly rotate counterclockwise. Table 4.8 summarizes the adjusted JA-parameters for the middle limb. Figure 4.17 to Figure 4.19 show the ΨI-characteristics of all three phases with the adjusted parameters. The adjustment does not change the responses of phases U and W significantly while improving the response of phase V. The simulated hysteresis loops of the adjusted limb and all other core sections are shown in Figure 4.20.

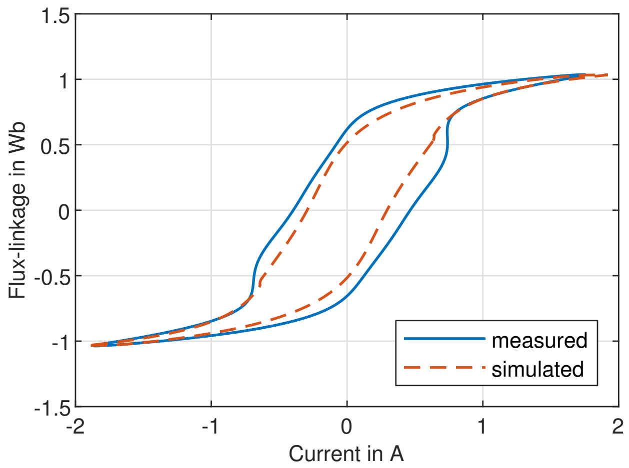

Figure 4.15: ΨI-characteristics of phase W with identical JA-parameters

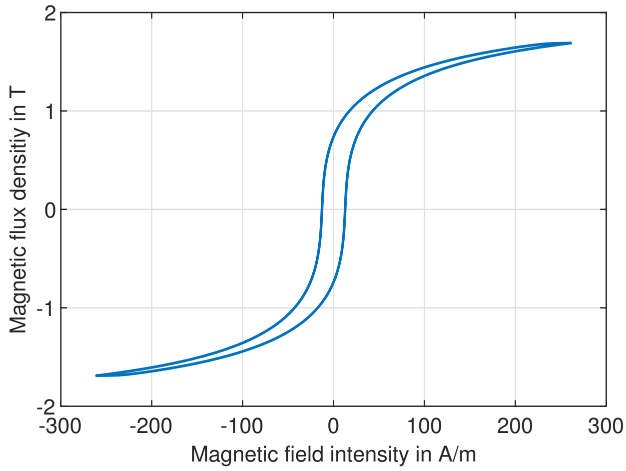

Figure 4.16: Identical BH-characteristic of all core elements

Table 4.8: Adjusted JA-parameters of the middle limb

α	a	M_s	k	c
-	-	A/m	A/m	A/m
$0.24 \cdot 10^{-3}$	120	$1.63 \cdot 10^{6}$	15	0.15

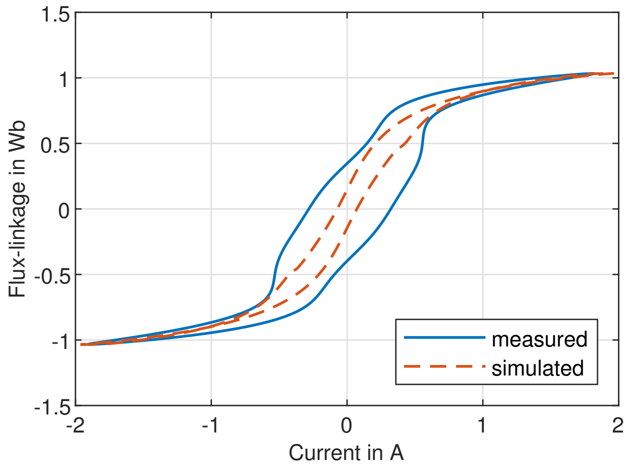

Figure 4.17: ΨI-characteristics of phase U with adjusted JA-parameters

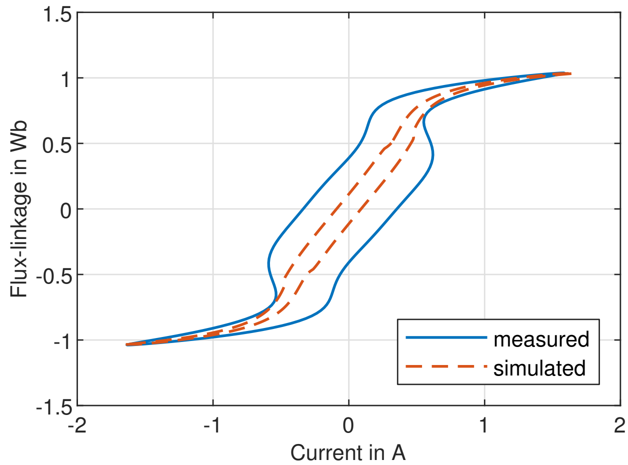

Figure 4.18: ΨI-characteristics of phase V with adjusted JA-parameters

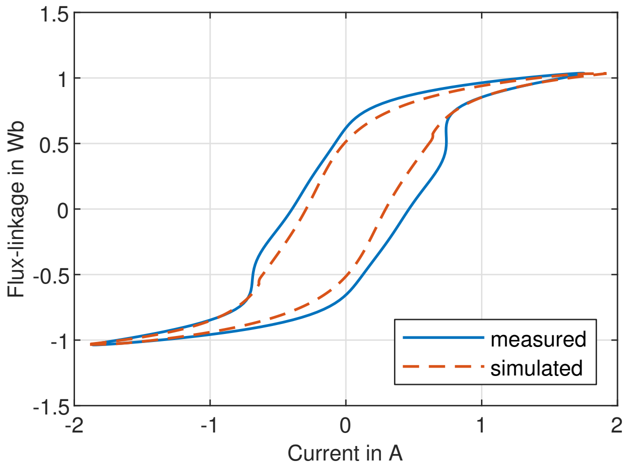

Figure 4.19: ΨI-characteristics of phase W with adjusted JA-parameter

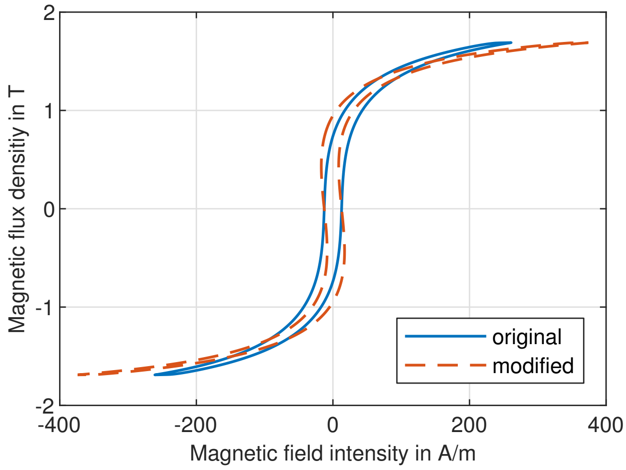

Figure 4.20: Original and modified BH-characteristics of the middle limb

Table 4.9: Loss resistances of the core elements

R_{limb}	R_{yoke}
Ω	Ω
2272	4219

The next step is the fitting of the dynamic losses. As already explained, the more simple two-component dynamic hysteresis model is chosen, which can be derived using a single no-load measurement at rated frequency and voltage. The dynamic loss is implemented by linear resistors in parallel to every JA-element. The resistance is then fitted to match the simulated active power loss to the measurements. The different lengths of limb and yoke elements lead to separate values for each type of core section. The values of the loss resistances are summarized in Table 4.9. Figure 4.21 to Figure 4.23 show the comparisons of the measurements and the finalized simulation model. The area of the simulated ΨI-characteristic of phase U is smaller than area of the measurement, while the opposite is true for phase W. The differences balance each other out, leading to an accurate reproduction of the total active loss. The results will be shown in more detail in chapter 5.

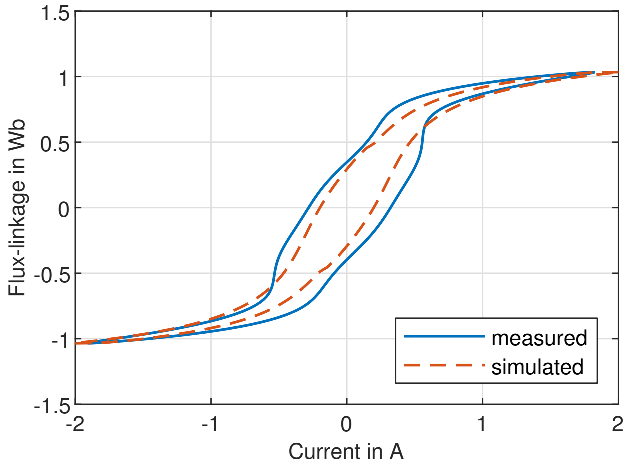

Figure 4.21: ΨI-characteristics of phase U with added dynamic loss

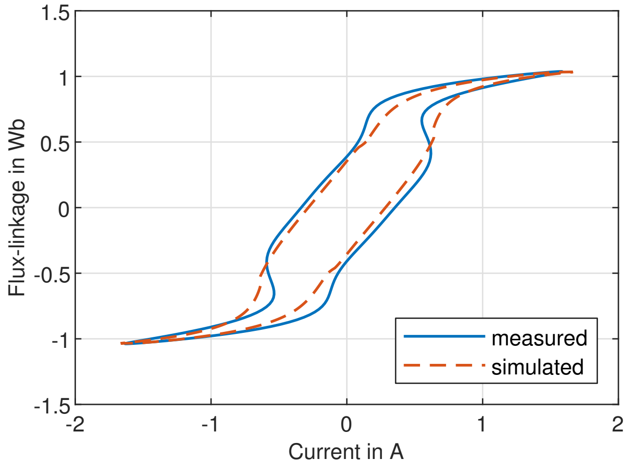

Figure 4.22: ΨI-characteristics of phase V with added dynamic loss

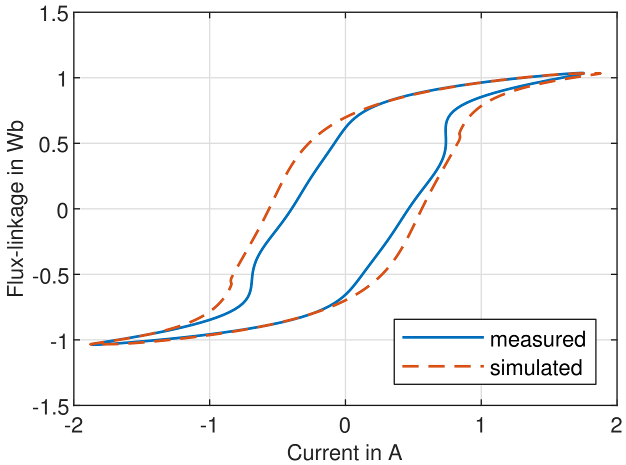

Figure 4.23: ΨI-characteristics of phase W with added dynamic loss

5 Simulation Results T74

5.1 Short-Circuit Test

The short-circuit test was conducted on the low-voltage side with the high-voltage windings short-circuited as seen in Figure 5.1. Figure 5.2 shows the supplied voltages of the measurement (solid line) and the simulation (dashed line). The power-amplifier was not able to supply a jitter-free sinusoidal voltage in this measurement setup. The measured voltage waveform, however, does not deviate significantly from the simulated voltage. Figure 5.3 compares the measured short-circuit currents (solid line) and the simulated currents (dashed line). The simulation yields slightly delayed currents. The current in phase V is overestimated slightly by the simulation. This is caused by the approach described in section 4.2, where the median short-circuit impedance is used for all phases. The accuracy can be further increased by the implementation of separate short-circuit impedances for the individual phases.

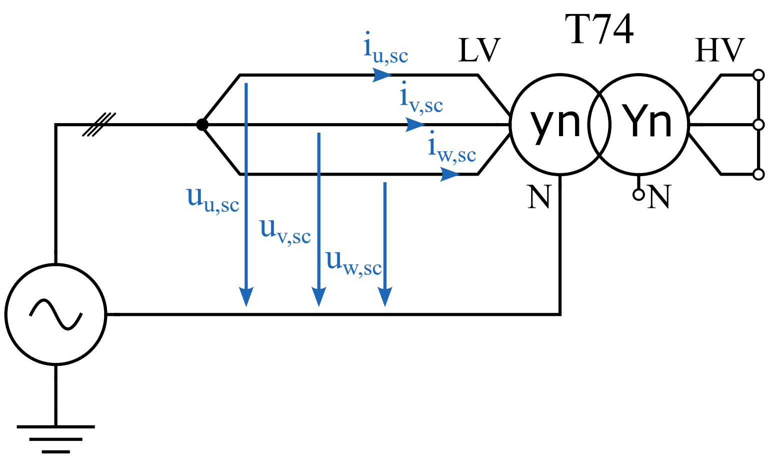

Figure 5.1: Short-circuit measurement setup

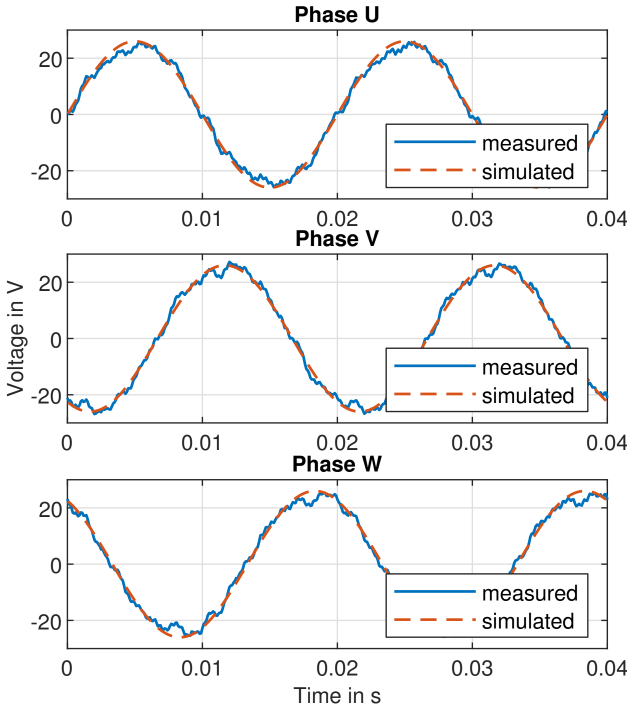

Figure 5.2: Phase voltages of the short-circuit test

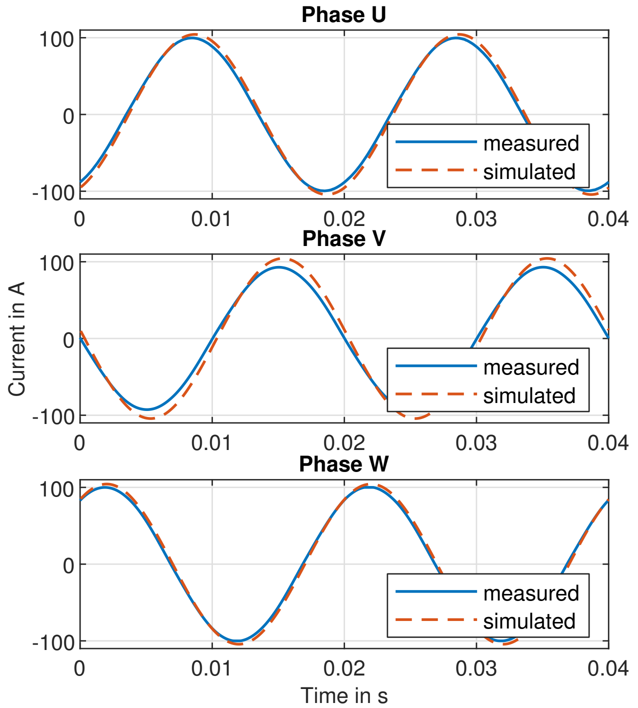

Figure 5.3: Phase currents of the short-circuit test

5.2 Zero-Sequence Test

The zero-sequence test was conducted as seen in Figure 5.4. The zero-sequence impedance of Yy transformers can be derived using multiple measurement setups, according to [32]. The zero-sequence impedance in this model represents the zero-sequence flux path in Figure 3.3. This flux leaves the core, enters the tank, and closes itself in the core again. This behavior is represented by the open-circuited zero-sequence test. Figure 5.5 shows the measured (solid line) and simulated (dashed line) voltages. The current waveforms in Figure 5.6 show that the simulation (dashed line) underestimates the current amplitude compared to the measurement (solid line). The measurement revealed a minor non-linearity, which might be the cause of the amplitude deviation. This non-linearity is deemed to be insignificant in the parameter estimation process, since the deviation is tolerable.

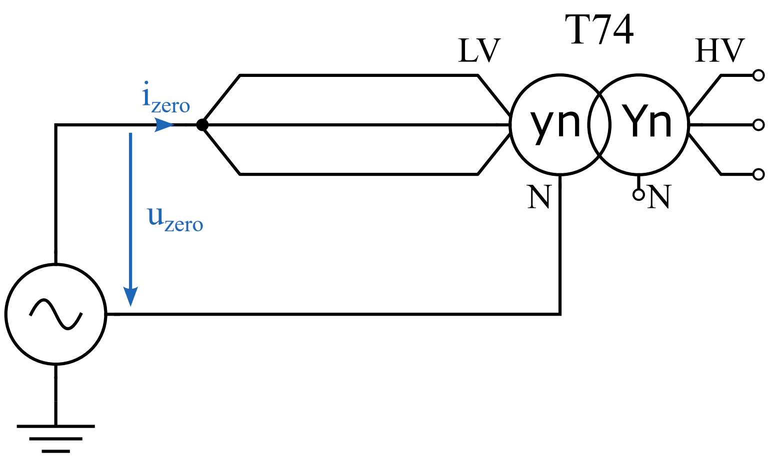

Figure 5.4: Zero-sequence measurement setup

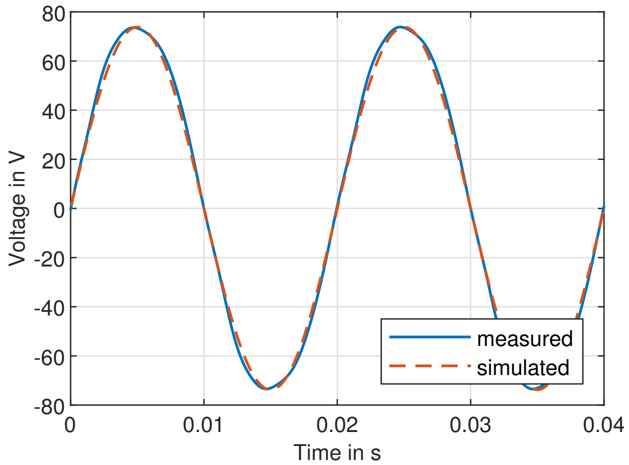

Figure 5.5: Voltages of the zero-sequence test

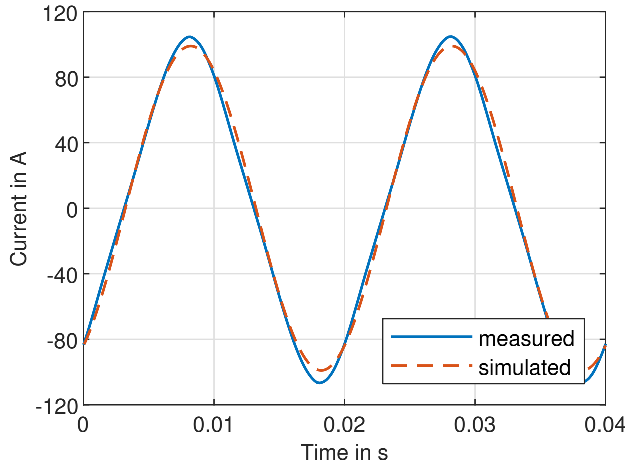

Figure 5.6: Currents of the zero-sequence test

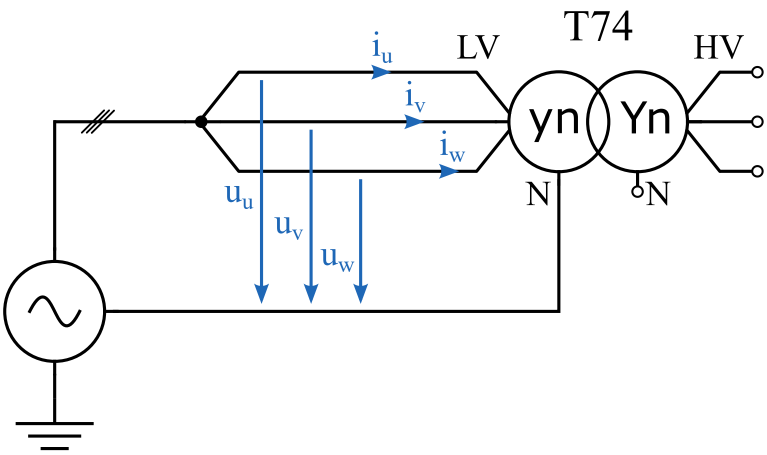

Figure 5.7: No-load measurement setup

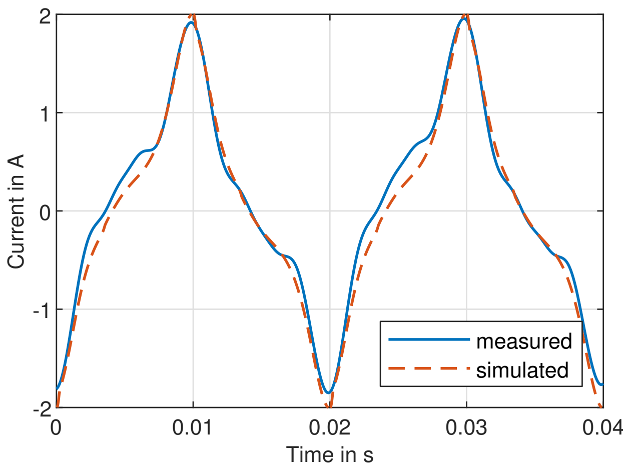

Figure 5.8: No-load currents of phase U

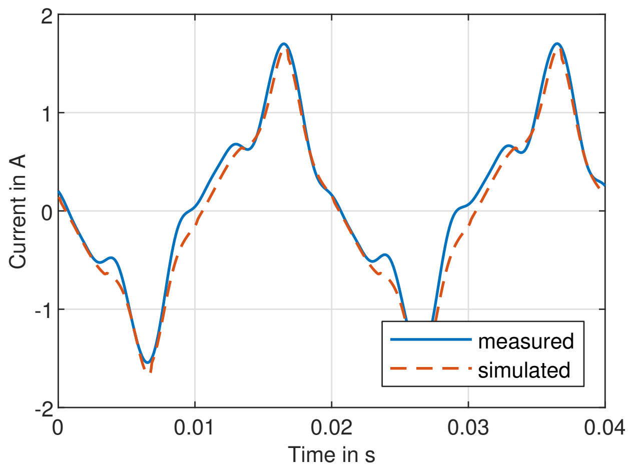

Figure 5.9: No-load currents of phase V

5.3 No-Load Test at Rated Frequency

The no-load test, seen in Figure 5.7, was conducted at rated frequency and voltage. The measured (solid) and simulated (dashed) current waveforms of phases U, V, and W are shown in Figure 5.8, Figure 5.9, and Figure 5.10 respectively. The differing current amplitudes, caused by a combination of the magnetic asymmetry and hysteresis, are predicted accurately in the simulation. The general shape of the current waveforms is in good accordance with the measurements. This proves the applicability of the single-phase hysteresis measurement in section 4.3. The accuracy could be further increased with improvements to the hysteresis model.

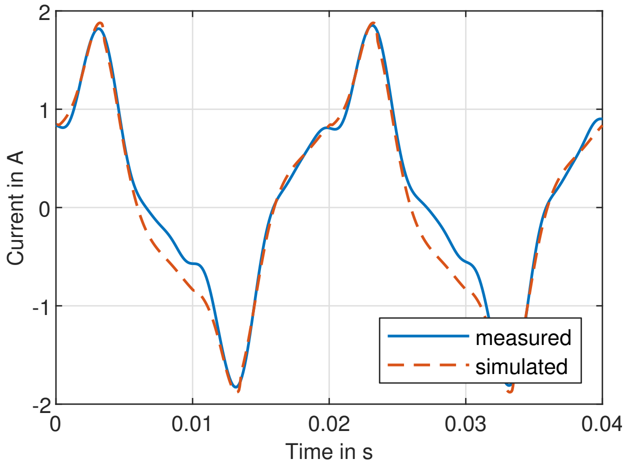

Figure 5.10: No-load currents of phase W

5.4 Voltage-Dependent No-Load Loss

The initial fitting of the dynamic hysteresis loss was performed at 1 pu (230 V). No-load tests at various excitation voltages were conducted to investigate the representation of voltage-dependent power loss of the model. The voltage was varied from 0.87 pu to 1.13 pu (200 V - 260 V). The measured and simulated powers are summarized in Table 5.1. As already mentioned in section 4.3, a measuring device capable of measuring not just the fundamental, but the overall power, was used. All presented values correspond to the overall power. The formulas utilized by the measuring device, shown in Appendix E, were also used in the simulation. Figure 5.11 compares the measured (cross markers) and simulated (circle markers) active power in dependence of the supplied excitation voltage. The dashed lines are polynomials of second order fitted to the measurements and simulations respectively. The two curves cross each other approximately at a voltage of 1 pu, since the dynamic loss components R_{yoke} and R_{limb} are fitted to represent the behavior correctly at nominal voltage. The simulation data shows a linear relation between active power and supplied excitation voltage. This leads to the overestimation of losses below nominal power and underestimation of losses above nominal voltage. The deviation between measured and simulated data increases significantly above nominal voltage, as mentioned in [5]. Figure 5.12 shows the voltage-dependent reactive power. The cross markers represent the measured data and the circle markers represent the simulated data. The dashed curves are polynomials of second order fitted to the measurement and simulation data respectively. The voltage-dependent reactive power loss is represented more accurately, however, the simulations deliver overestimations over all measured voltages. The core parameters were

Table 5.1: Measured and simulated voltage-dependent no-load losses

U	U	P_{meas}	Q_{meas}	S_{meas}	P_{sim}	Q_{sim}	S_{sim}
V	pu	W	var	VA	W	var	VA
200	0.87	126.74	256.88	286.44	139.72	280.49	316.14
205	0.89	134.15	300.60	329.18	145.36	319.95	354.49
210	0.91	141.76	346.23	374.12	151.07	365.34	398.77
215	0.93	149.77	404.36	431.20	156.87	417.67	450.01
220	0.96	158.15	465.42	491.56	162.73	478.62	509.84
225	0.98	169.94	538.28	564.47	168.64	549.92	580.06
230	1.00	177.19	623.59	648.27	174.60	633.89	662.99
235	1.02	186.83	721.07	744.88	180.61	733.62	761.74
240	1.04	202.45	834.94	859.13	186.63	853.94	881.15
245	1.07	214.36	970.37	993.76	192.66	1000.53	1026.94
250	1.09	225.95	1129.84	1152.22	198.67	1182.67	1208.42
255	1.11	239.95	1323.81	1345.39	204.66	1414.67	1439.92
260	1.13	260.74	1556.06	1577.76	210.61	1721.25	1746.21

fitted to the active power loss at nominal voltage, which resulted in a slight overestimation of reactive loss even at nominal voltage. The complex power is shown in Figure 5.13. The results show the model's inability to correctly represent the voltage-dependent active power loss when two-component hysteresis model is used.

5.5 Frequency-Dependent No-Load Loss

No-load tests with varying excitations and frequencies were conducted to investigate the frequency-dependent power losses. Solely varying the frequency would lead to different flux amplitudes. Therefore, the excitation voltages were adapted to the frequencies according to Equation 4.11. This adaption results in a constant magnetic flux amplitude over all measured frequencies. This means the measured and simulated powers are only frequency-dependent. Table 5.2 summarizes the measurement and simulation data. As mentioned before, the shown values correspond the overall powers. Figure 5.14 contains the measured (cross markers) and simulated (circle markers) active

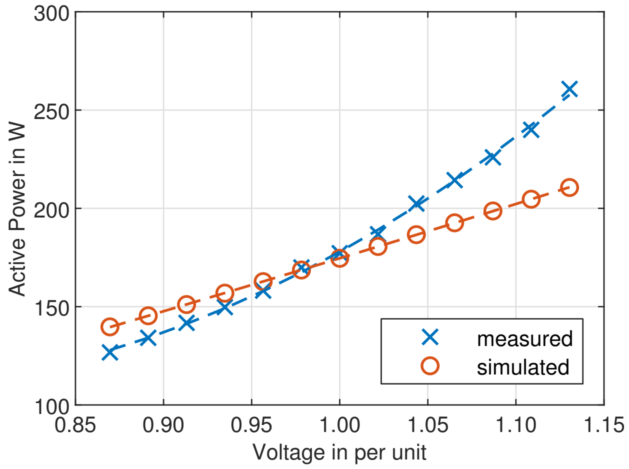

Figure 5.11: Voltage-dependent active power

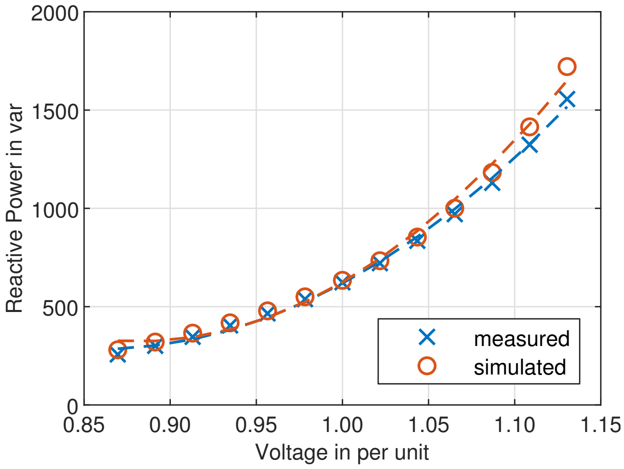

Figure 5.12: Voltage-dependent reactive power

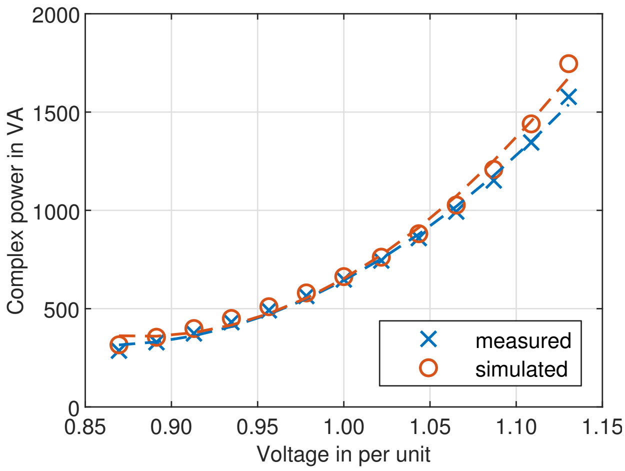

Figure 5.13: Voltage-dependent complex power

Table 5.2: Measured and simulated frequency-dependent no-load losses

f	f	U	P_{meas}	Q_{meas}	S_{meas}	P_{sim}	Q_{sim}	S_{sim}
Hz	pu	V	W	var	VA	W	var	VA
35	0.7	161	101.98	493.99	504.42	97.92	443.48	457.91
40	0.8	184	125.08	550.27	564.31	121.17	506.92	525.51
45	0.9	207	152.02	593.90	613.05	146.73	570.39	593.85
50	1.0	230	178.03	625.46	650.30	174.60	633.89	662.99
55	1.1	253	206.35	649.52	681.51	204.79	697.34	732.88
55	1.2	276	237.76	676.40	716.97	237.30	760.83	803.69
60	1.3	299	268.34	694.85	744.87	272.12	824.30	875.39

power over the frequency in per unit. The dashed lines represent polynomials of second order of the measurement and simulation data respectively. The simulation slightly underestimated the active power below nominal frequency and slightly overestimated the loss above nominal frequency. In general, however, the frequency-dependent active power loss is represented correctly by the simulation model. Figure 5.15 shows the measured (cross markers) and simulated (circle markers) reactive power over various frequencies. The dashed lines are once again polynomials of second order fitted to the measurement and simulation data respectively. The curves cross each other approximately at nominal voltage. The simulation data show a linear relation between reactive power and frequency due to the use of the loss resistances R_{yoke} and R_{limb}. The measurement shows the behavior as seen in Figure 3.15, where not only a dynamic eddy component dependent of the frequency but a dynamic excess component dependent on the frequency to the power of 0.5 occurs. Merely using the eddy component in the form of the loss resistances fitted to nominal frequency leads to an underestimation of reactive power below nominal frequency and overestimation of reactive power above nominal frequency. The discrepancy between the measured and simulated reactive power can also be seen in the complex power, as shown in Figure 5.16. The accuracy of the simulation can be improved by expanding the model to include a three-component hysteresis representation.

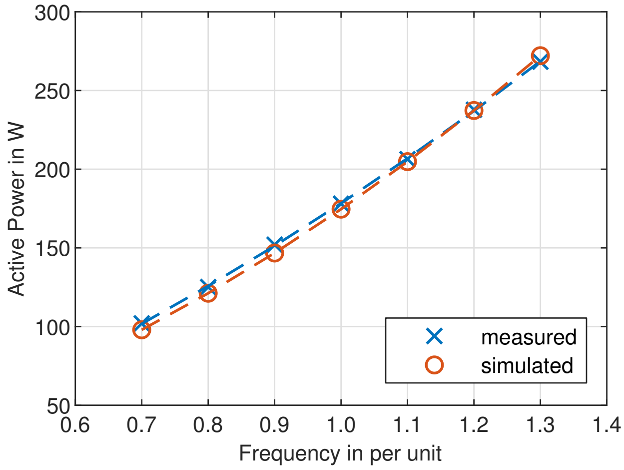

Figure 5.14: Frequency-dependent active power

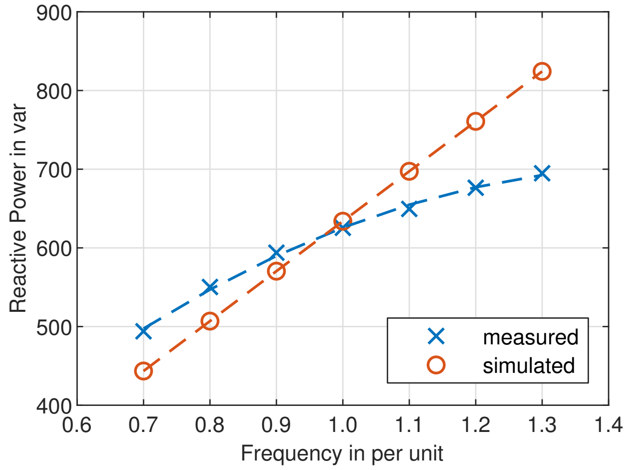

Figure 5.15: Frequency-dependent reactive power

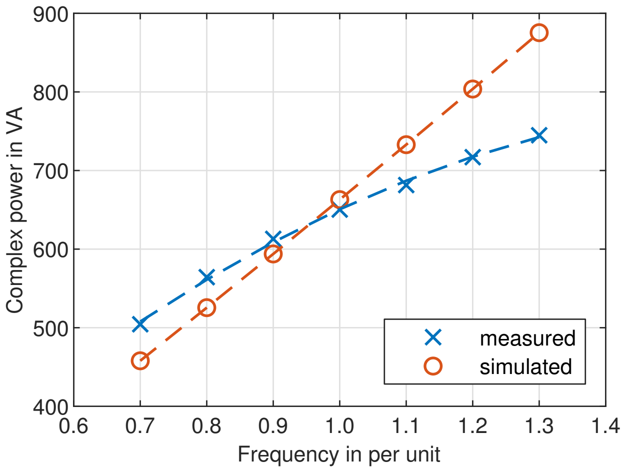

Figure 5.16: Frequency-dependent complex power

5.6 Back-to-Back (B2B)

The back-to-back test setup seen in Figure 5.17 was chosen to test the model's general capability to reproduce the behavior of the transformer under DC-excitation. A similar but not identical YNyn0 transformer built in 1990 was connected to the T74 transformer. The second transformer will hereafter be referred to as T90. A DC-voltage source can be connected on high-voltage potential to the neutral points between the two transformers. This source can then be used to superimpose a DC-excitation on high-voltage potential. The results in this section only investigate the general capability of the simulation, since no separate model for the T90 transformer was derived. An exact copy of the T74 model was used instead. Therefore, the results can not be used as a measure of accuracy. A model of the second transformer should be derived to further investigate how accurate the simulation is.

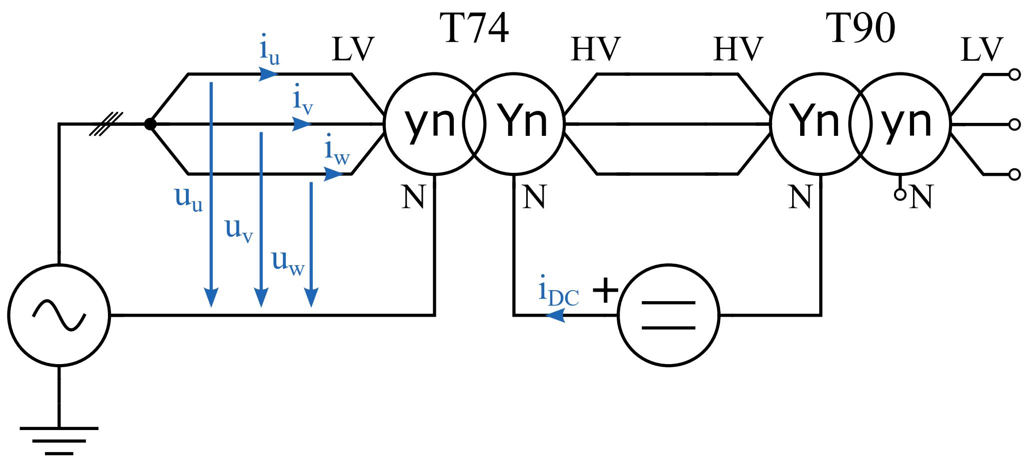

Figure 5.17: Back-to-back measurement setup

Multiple measurements with various DC-amplitudes were conducted to investigate the model. Figure 5.18 shows the measured current over time when no DC is superimposed. The simulated currents over time of this scenario are shown in Figure 5.19. The amplitudes of the simulated B2B-currents are twice as high as the amplitudes of the regular no-load simulation seen in Figure 5.8 - Figure 5.10. This is caused by the use of the two identical T74-models. The measured currents in Figure 5.18 indicate that the newer T90 transformer has lower no-load currents at rated excitation than the T74 transformer. The comparison of both waveforms confirms the model's ability to recreate the general current shapes.

A measurement of the low-voltage currents with superimposed direct currents ranging from 100 mA

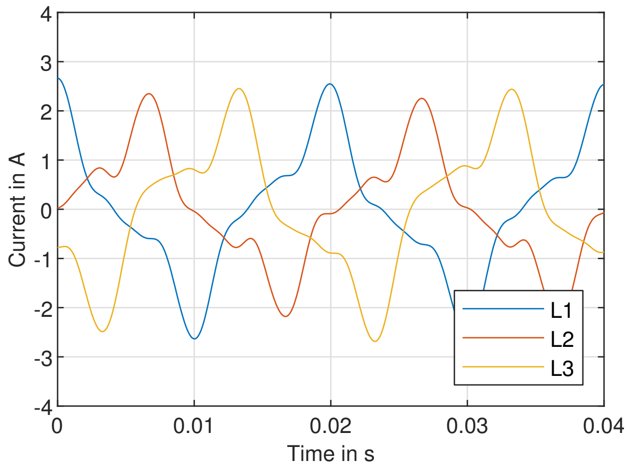

Figure 5.18: Measured B2B-currents without any DC-current

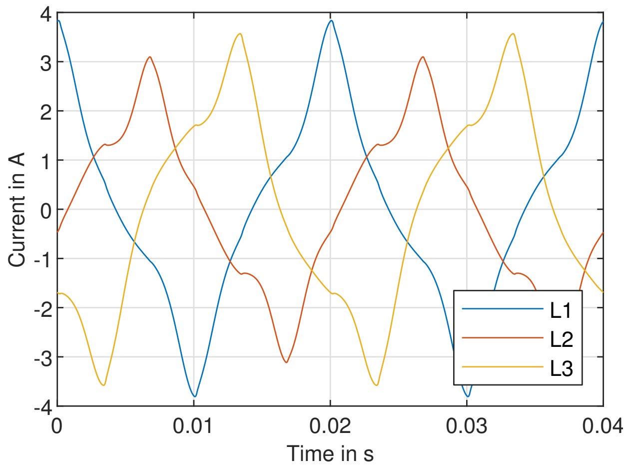

Figure 5.19: Simulated B2B-currents without any DC-current

to 1900 mA in steps of 100 mA was conducted to investigate the behavior under DC-excitation. The resulting current of phase U is shown in Figure 5.20. The other phases produce nearly identical waveforms. The simulation result of phase U with the same direct currents is shown in Figure 5.21. As before, the amplitudes differ, since no specific model was developed for the T90 transformer. Both figures show a rise of the phase currents as the direct current is increased. A half-cycle saturation is visible in both figures, as higher amplitudes are achieved during the positive half-cycle. An example of the measured currents is shown in Figure 5.22, where a 1400 mA direct current is superimposed. Obviously, the same DC-excitation leads to different amplitudes in the simulation. Therefore, a simulation with similar amplitudes is used to compare the waveforms. The result of a simulation with a superimposed direct current of 1900 mA is shown in Figure 5.23.

The active and reactive power loss is shown in Figure 5.24 and Figure 5.25 respectively. Unlike the real measurement, the simulated active power decreases as the direct current rises. The phase shift between the simulated voltages and currents approaches 90° as the direct current is increased, which explains the decrease in active power. This, however, is true for the measurement as well and yet the measured active power increases. This discrepancy might be explained by a missing loss component in the simulation model. The general behavior of the reactive loss is recreated correctly. Once again, the simulation results were derived using two identical models of the T74 transformer while the measurements were conducted with the T74 and T90 transformers. A deviation of amplitudes was therefore expected. Be that as it may, the results prove the applicability of the simulation model for GIC-studies.

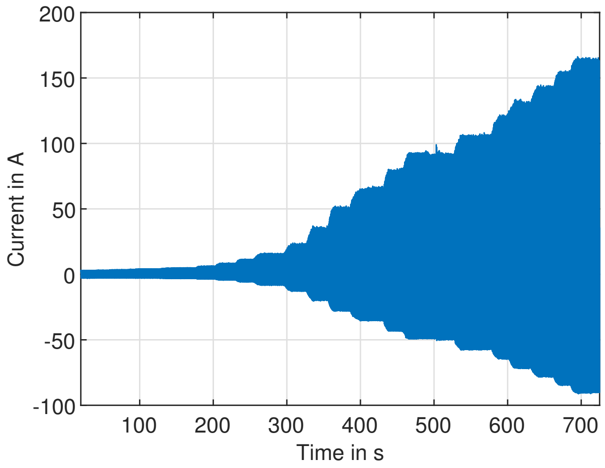

Figure 5.20: Measured B2B-currents

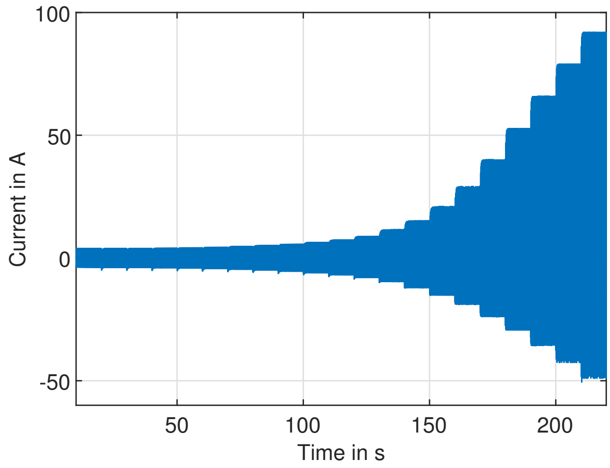

Figure 5.21: Simulated B2B-currents

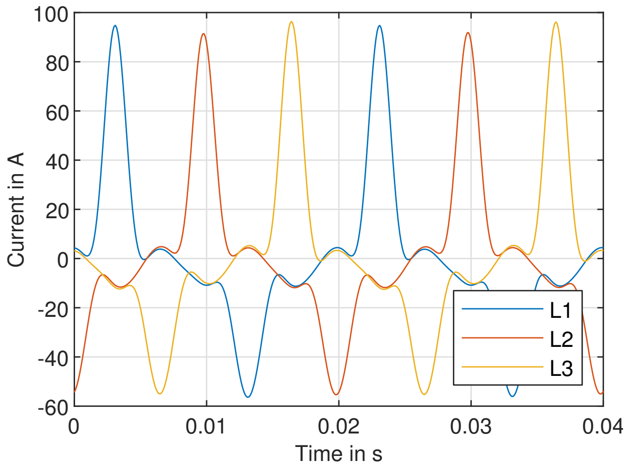

Figure 5.22: Measured B2B-currents with 1400 mA DC

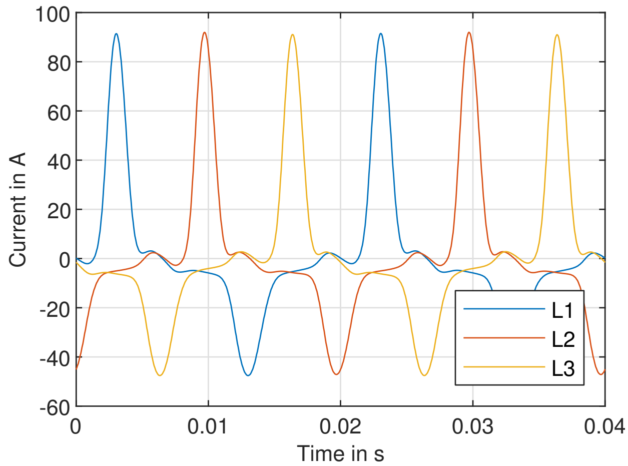

Figure 5.23: Simulated B2B-currents with 1900 mA DC

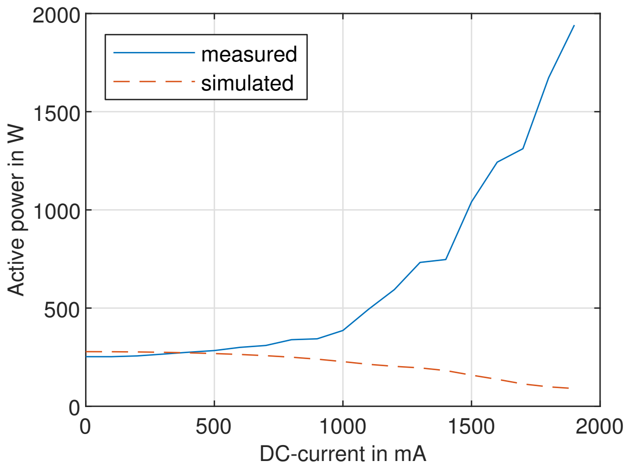

Figure 5.24: DC-dependent active power

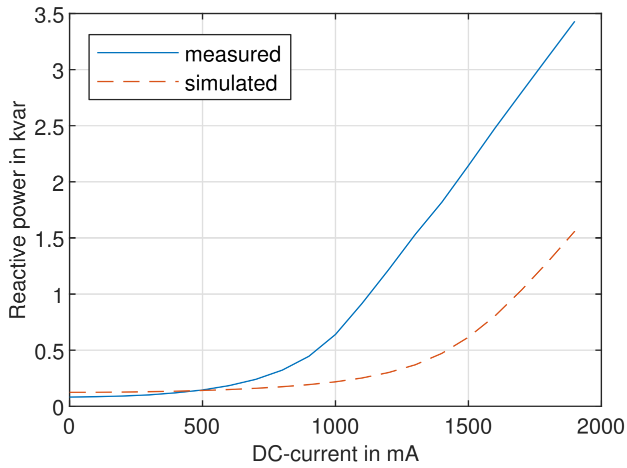

Figure 5.25: DC-dependent active power

6 Discussion and Outlook

On the development of the model

The classic way to model a transformer is the well-known single-phase equivalent T-model. This model, however, lacks magnetic coupling [4] and is only valid in steady-state [3]. A transformer model capable of reproducing low-frequency transients is derived in section 3.2. This model uses the topologically correct duality-approach which converts the magnetic circuit of the transformer into an equivalent electric circuit [15]. A model of a three-phase, three-limb, two-winding transformer is derived in section 3.2. The same approach can be used to derive a five-limb transformer. A third winding can be added with the approach shown in [37]. Therefore, the duality approach can be applied to a multitude of transformer core and winding configurations.

The modeling of the iron core is addressed in section 3.3. The derived model in this thesis implements a hysteresis model in the form of an inverse JA-model. The JA-model replicates the static hysteresis loss. The dynamic hysteresis loss can be incorporated with a two- or more accurate three-component approach, as seen in subsection 3.3.2. The model in this thesis uses the simpler two-component model which is implemented with constant loss resistances in parallel to every JA core element. Depending on the investigated low-frequency study, a static hysteresis model might not be necessary. In such cases a simpler piecewise linear approximation can be used. [5] The importance of a dynamic hysteresis model can depend on the investigated transient as well. However, the opinions on the importance of dynamic hysteresis modeling are divided [5]. The lack of definite answers makes this topic interesting for future research.

On the parameter derivation

The derivation of the linear parameters for the model of the T74 is straightforward, as seen in section 4.2. The short-circuit and zero-sequence impedance can be derived by standard tests. The more interesting measurements are associated with the identification of the non-linear core loss. Two possible approaches are shown and explained in subsection 3.4.2. section 4.3 shows the execution of the measurement and fitting process. It is shown that the behavior of the core can be measured with a low-frequency sinusoidal voltage source. The measurement is possible with portable measuring devices, since a lower frequency is accompanied with a lower voltage amplitude [33]. The measurement returned a rather unusual looking characteristic as seen in Figure 4.4. The loop widens as it starts to saturate. This makes the fitting of the parameters difficult, since the JA-model was developed for sigmoid-shaped hysteresis loops [22]. The accuracy could be improved by making the parameter k, which is responsible for the width of the loop, dependent on the excitation. Such a modification is shown in [28]. Many modifications of the JA-model exist that extend the model or improve the accuracy. One main goal of this thesis, however, was to show the general applicability of the JA-model in the case of a three-limb transformer. A highly accurate replication of the measurements was not a top priority. Therefore, a very basic version of the JA-model is used. Nevertheless, the measurements and simulations are in good agreement. For future research more time should be invested in a optimization procedure of the JA-parameters. A fitting by hand is possible and can lead to acceptable results as shown in section 4.3, however, an automated optimization procedure can drastically improve user-friendliness.

The same hysteresis measurement is not repeatable at higher frequencies to derive the dynamic hysteresis loss components. The capacitive influence of the transformer at higher frequencies significantly affects the shape of the measured hysteresis, rotating it counterclockwise. Therefore, the dynamic loss components can not be fitted to the measured shape of the hysteresis. It is possible to fit the parameters to no-load test data measured at different excitations and frequencies. Results of these measurements are shown in chapter 5, however, such data might not be available and is difficult to measure outside of laboratory settings. Therefore, the simpler two-component dynamic model was used, which can be fitted to standard no-load test data.

On the simulation results

Various simulations and measurements of T74-transformer were compared in chapter 5. All phases were assumed to be equal in the parameter derivation process. The design of transformers, which also causes the magnetic asymmetry, leads to unavoidable differences between the phases. This is seen in the comparison of the measured and simulated short-circuit test. The simulation returns a slightly too high short-circuit current in phase V. This can easily be corrected by the implementation of phase-specific short-circuit impedances. The difference between measured and simulated current, however, is not significant enough to make this adjustment necessary.

The zero-sequence test can show a non-linear behavior in Yy-transformers as explained in the standard [32]. The zero-sequence measurement of the T74-transformer does in fact show a slight non-linearity. This is, however, insignificant and is therefore ignored in the parameter identification process. The measurement confirms the assertion in [14], that the non-linearity can safely be neglected.

The simulation over various voltages shows the inability of the two-component hysteresis model to accurately represent the active power loss. The parallel loss resistance overestimates the active loss below nominal voltage and underestimates it above nominal voltage. The reactive power is in good accordance over a wide voltage range. The accuracy of the active power can be increased if a three-component hysteresis model with an excitation-dependent excess loss component is used instead.

The frequency-dependent no-load loss comparison shows that the model is able to reproduce the active power over a wide frequency range. The reactive power, however, is underestimated below and overestimated above nominal frequency. Again, a three-component hysteresis model is able to represent the losses more accurately.

The general ability of the model to represent low-frequency transients was tested with a back-to-back (B2B) test, which allows to superimpose direct currents. It is important to note that no simulation model of the second transformer was derived. Instead, a one-to-one copy of the T74 model was used. This obviously makes an evaluation of the simulation accuracy nonsensical. The results can, however, show if the general transient response is reproduced correctly. The simulation model is able to reproduce the general behavior as the results show. The only major discrepancy can be seen in the measured active power. The simulated power slowly decreases as the direct current is increased, while the measured active power rises. The cause for this is not known and requires further research. Furthermore, a model of the second transformer should be derived in order to assess the simulation accuracy.

On the implementation of the model

The model was implemented in Matlab Simulink 2019a. It was tested with the Simscape Electrical library as well as the Specialized Power Systems library. Both libraries are suitable and delivered identical results. However, the model implemented in Specialized Power Systems is prone to instabilities. The use of the Simscape Electrical library is therefore recommended.

On the application in transmission grid simulations

The three-component hysteresis model gives a visible advantage when it comes to voltage- and frequency-dependent loss representation. Some transient studies such as ferroresonance might even require a detailed three-component model [5]. However, considering the required effort, such a model is not feasible for transmission grid operators. It was shown that the hysteresis measurement is not usable at higher frequencies due to the capacitive influence as the frequency rises. The dynamic components can theoretically be fitted to loss measurements using various voltages and frequencies. Such measurements are not technically feasible for large power transformers outside of specialized laboratory settings. Datasheets usually provide no-load loss data at 90 %, 100 %, and 110 % of nominal voltage. This can be used to fit the excess component. The lack of frequency-dependent data, however, makes the verification at different frequencies not possible. This means a three-component dynamic model can hardly be implemented for already installed equipment. This assessment leads back to the two-component model which can be implemented with considerably less effort. This approach results in a massive improvement in accuracy over the classic single-phase equivalent models at a reasonable cost. The only out of ordinary measurement is the hysteresis measurement which can be measured in mere minutes using modern transformer testing utilities. The two-component hysteresis model gives the most cost-effective results for transmission grid operators.

Appendix

Appendix A

Derivation of the Magnetic Asymmetry

The derivation is based on [10]. The following equations are given

$$i_U - i_V = i'_U - i'_V \tag{A.1}$$

$$i_V - i_W = i'_V - i'_W \tag{A.2}$$

$$i_W - i_U = i'_W - i'_U \tag{A.3}$$

$$i_U + i_V + i_W = 0 \tag{A.4}$$

Equation A.1 can be rearranged to

$$i_U = i'_U - i'_V - i_V \tag{A.5}$$

The exchange of i_V with Equation A.4 leads to

$$i_U = i'_U - i'_V - i_U - i_W \tag{A.6}$$

Exchanging i_W with Equation A.3 leads to

$$i_U = i'_U - i'_V - i_U - i'_U - i'_W - i_U \tag{A.7}$$

Which can be rearranged to

$$3i_{\mathrm{U}} = 2i'_{\mathrm{U}} - i'_{\mathrm{V}} - i'_{\mathrm{W}} \tag{A.8}$$

Adding and subtracting i'_{U} on the right side results in

$$3i_{\mathrm{U}} = 3i'_{\mathrm{U}} - i'_{\mathrm{U}} - i'_{\mathrm{V}} - i'_{\mathrm{W}} \tag{A.9}$$

Dividing both sides by three delivers the final form of the equation for the first phase

$$i_{\mathrm{U}} = i'_{\mathrm{U}} - \frac{1}{3}(i'_{\mathrm{U}} - i'_{\mathrm{V}} - i'_{\mathrm{W}}) \tag{A.10}$$

Appendix B

Derivation of the JA Equation 3.9

The following two equations of the effective field intensity H_e and the irreversible magnetization M_irr are given

$$H_\mathrm{e} = H + \alpha M \tag{B.1}$$

$$M_\mathrm{irr} = M_\mathrm{an} - \delta k \left(\frac{\mathrm{d}M_\mathrm{irr}}{\mathrm{d}H_\mathrm{e}} \right) \tag{B.2}$$

Equation B.2 can be rearranged in the following way

$$\frac{\mathrm{d}M_\mathrm{irr}}{\mathrm{d}H_\mathrm{e}} = \frac{M_\mathrm{an} - M_\mathrm{irr}}{\delta k} \tag{B.3}$$

Inverting both sides of the equation and inserting Equation B.1 leads to

$$\frac{\mathrm{d}(H + \alpha M)}{\mathrm{d}M_\mathrm{irr}} = \frac{\delta k}{M_\mathrm{an} - M_\mathrm{irr}} \tag{B.4}$$

The left side of the equation can then be rewritten into

$$\frac{\mathrm{d}H}{\mathrm{d}M_\mathrm{irr}} + \alpha = \frac{\delta k}{M_\mathrm{an} - M_\mathrm{irr}} \tag{B.5}$$

Subtracting α on both sides and converting the right side of the equation to a common denominator leads to

$$\frac{\mathrm{d}H}{\mathrm{d}M_{\mathrm{irr}}} = \frac{\delta k - \alpha(M_{\mathrm{an}} - M_{\mathrm{irr}})}{M_{\mathrm{an}} - M_{\mathrm{irr}}} \tag{B.6}$$

Inverting both sides leads to the final equation

$$\frac{\mathrm{d}M_{\mathrm{irr}}}{\mathrm{d}H} = \frac{M_{\mathrm{an}} - M_{\mathrm{irr}}}{\delta k - \alpha(M_{\mathrm{an}} - M_{\mathrm{irr}})} \tag{B.7}$$

Appendix C

Derivation of the JA Equation 3.12

The following two equations of the irreversible rate of magnetization change and reversible rate of magnetization change are given

$$\frac{\mathrm{d}M_{\mathrm{irr}}}{\mathrm{d}H} = \frac{M_{\mathrm{an}} - M_{\mathrm{irr}}}{\delta k - \alpha(M_{\mathrm{an}} - M_{\mathrm{irr}})} \tag{C.1}$$

$$\frac{\mathrm{d}M_{\mathrm{rev}}}{\mathrm{d}H} = c\left(\frac{\mathrm{d}M_{\mathrm{an}}}{\mathrm{d}H} - \frac{\mathrm{d}M_{\mathrm{irr}}}{\mathrm{d}H}\right) \tag{C.2}$$

The complete rate of magnetization change is the sum of both components

$$\frac{\mathrm{d}M}{\mathrm{d}H} = \frac{\mathrm{d}M_{\mathrm{irr}}}{\mathrm{d}H} + \frac{\mathrm{d}M_{\mathrm{rev}}}{\mathrm{d}H} \tag{C.3}$$

Inserting Equation C.2 into Equation C.3 leads to

$$\frac{\mathrm{d}M}{\mathrm{d}H} = \frac{\mathrm{d}M_{\mathrm{irr}}}{\mathrm{d}H} + c\left(\frac{\mathrm{d}M_{\mathrm{an}}}{\mathrm{d}H} - \frac{\mathrm{d}M_{\mathrm{irr}}}{\mathrm{d}H}\right) \tag{C.4}$$

The expansion of the product on the right side leads to the following expression

$$\frac{\mathrm{d}M}{\mathrm{d}H} = (1-c)\frac{\mathrm{d}M_{\mathrm{irr}}}{\mathrm{d}H} + c\frac{\mathrm{d}M_{\mathrm{an}}}{\mathrm{d}H} \tag{C.5}$$

Inserting Equation C.1 into Equation C.5 leads to the final equation of the JA-model

$$\frac{\mathrm{d}M}{\mathrm{d}H} = (1-c)\frac{M_{\mathrm{an}} - M_{\mathrm{irr}}}{\delta k - \alpha(M_{\mathrm{an}} - M_{\mathrm{irr}})} + c\frac{\mathrm{d}M_{\mathrm{an}}}{\mathrm{d}H} \tag{C.6}$$

Appendix D

Implemented Inverse JA-Model

The implemented inverse JA-model is based on the time-stepping approach found in [27]. It was enhanced by the parameter δ_M based on [26]. This parameter prevents possible non-physical behavior at the loop tips. The values of $H(t)$ and $B(t)$ are the known values from the preceding step which are used to calculate the values of the current step.

$$\Delta B = B(t + \Delta t) - B(t) \tag{D.1}$$

$$M(t) = \frac{B(t)}{\mu_0} - H(t) \tag{D.2}$$

$$H_\mathrm{e}(t) = H(t) + \alpha M(t) \tag{D.3}$$

$$M_\mathrm{an}(t) = M_\mathrm{s}\left[\coth\frac{H_\mathrm{e}(t)}{a} - \frac{a}{H_\mathrm{e}(t)}\right] \tag{D.4}$$

$$\frac{\mathrm{d}M_\mathrm{an}}{\mathrm{d}H_\mathrm{e}} = \frac{M_\mathrm{s}}{a}\left[1 - \coth^2\frac{H_\mathrm{e}(t)}{a} + \left(\frac{a}{H_\mathrm{e}(t)}\right)^2\right] \tag{D.5}$$

$$M_\mathrm{irr}(t) = \frac{M(t) - cM_\mathrm{an}(t)}{1 - c} \tag{D.6}$$

$$\delta_{\mathrm{M}} = \begin{cases} 0 & \text{if } \Delta B < 0 \text{ and } M_{\mathrm{an}}(t) - M(t) > 0 \\ 0 & \text{if } \Delta B > 0 \text{ and } M_{\mathrm{an}}(t) - M(t) < 0 \\ 1 & \text{otherwise} \end{cases} \tag{D.7}$$

$$\frac{\mathrm{d}M_{\mathrm{irr}}}{\mathrm{d}B_{\mathrm{e}}} = \delta_{\mathrm{M}} \frac{M_{\mathrm{an}}(t) - M_{\mathrm{irr}}(t)}{\mu_0 k \delta} \tag{D.8}$$

$$\frac{\mathrm{d}M}{\mathrm{d}B} = \frac{(1-c)\frac{\mathrm{d}M_{\mathrm{irr}}}{\mathrm{d}B_{\mathrm{e}}} + \frac{c}{\mu_0}\frac{\mathrm{d}M_{\mathrm{an}}}{\mathrm{d}H_{\mathrm{e}}}}{1 + \mu_0(1-\alpha)(1-c)\frac{\mathrm{d}M_{\mathrm{irr}}}{\mathrm{d}B_{\mathrm{e}}} + c(1-\alpha)\frac{\mathrm{d}M_{\mathrm{an}}}{\mathrm{d}H_{\mathrm{e}}}} \tag{D.9}$$

$$M(t+\Delta t) = M(t) + \frac{\mathrm{d}M}{\mathrm{d}B}\Delta B \tag{D.10}$$

$$H(t+\Delta t) = \frac{B(t+\Delta t)}{\mu_0} - M(t+\Delta t) \tag{D.11}$$

Appendix E

Power Calculation

The following formulas show how the measuring device calculates the AC-power. The same approach was used to calculate the simulation data. The active power is calculated according to the next formula

$$P = \frac{1}{N} \sum_{n=0}^{N} u[n] \cdot i[n] \tag{E.1}$$

The apparent power is calculated according to

$$S = U_{\mathrm{RMS}} \cdot I_{\mathrm{RMS}} \tag{E.2}$$

The reactive power can then be calculated with

$$Q = \sqrt{S^2 - P^2} \tag{E.3}$$

Appendix F

Hysteresis Measurement With a Transformer Test Device

The hysteresis of the T74-transformer was also measured with a yet unreleased trial software of a specialized transformer testing device. This device uses a DC-excitation to measure the hysteresis. The software was still in development which lead to limitations in the measurement process. The device was only able to deliver measurements on the high-voltage side. The measurement in Figure F.1 therefore shows the measured ΨI-characteristic measured from the high-voltage side. The widening of the loop is visible even if not as distinct. The measurement with the low-frequency sinusoidal excitation on the low-voltage side is shown in Figure F.2.

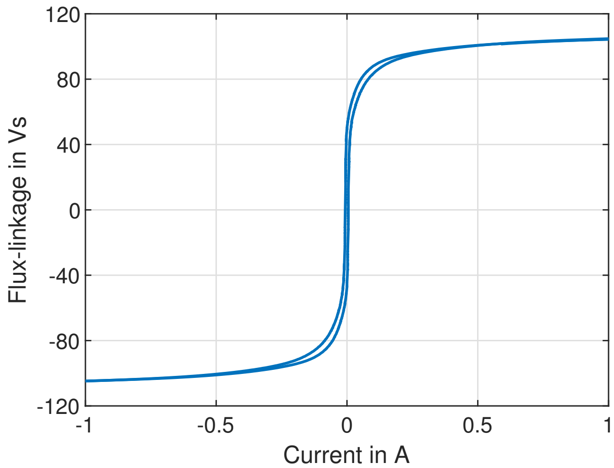

Figure F.1: Measured hysteresis using DC-excitation

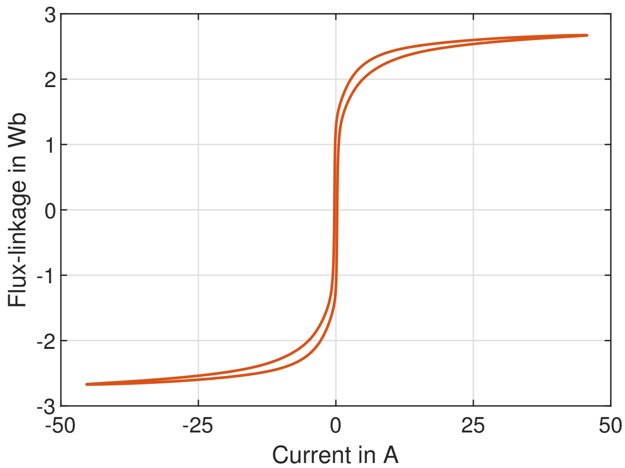

Figure F.2: Measured hysteresis using AC-excitation

The two measurements were conducted on different voltage potentials. This makes a conversion of the measured values necessary before the two loops can be compared. The flux-linkages were converted to the flux using the individual number of winding turns. The measured high-voltage current was converted to the low-voltage side using the winding ratio. The now comparable loops are shown in Figure F.3. It is obvious that the loop of the test device saturates farther. The two measured loops are in good accordance, besides the different current peaks.

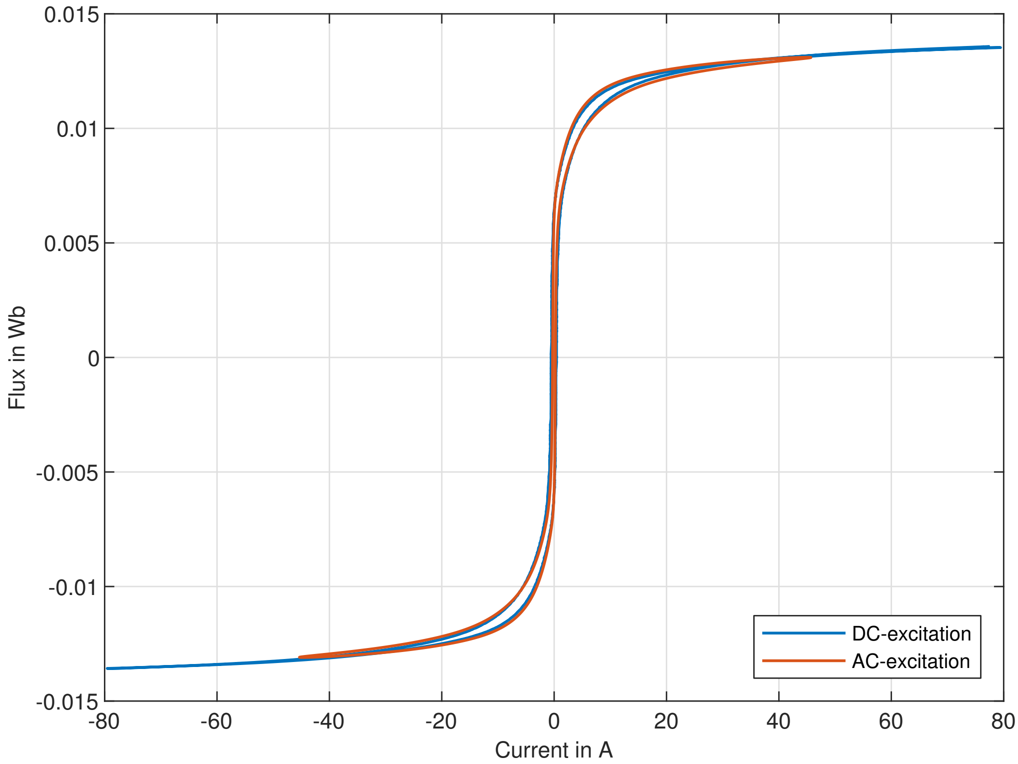

Figure F.3: Comparison of the hysteresis loops

Appendix G

Conference Proceeding

Measurement based transformer modelling approach

Dennis Albert, Dragan Maletic, and Herwig Renner

Internationaler ETG-Kongress 2021
Das Gesamtsystem im Fokus der Energiewende : 18.-19. Mai 2021

ETG-Kongress 2021 . ISBN 978-3-8007-5549-3 . ©VDE VERLAG GMBH . Berlin . Offenbach

Measurement based transformer modelling approach
Messdaten basierte Modellierung von Transformatoren

Dennis Albert*, Dragan Maletic*, and Herwig Renner
Institute of Electrical Power Systems, Graz University of Technology, 8010 Graz, Austria, dennis.albert@tugraz.at

Kurzfassung

Die Modellierung von Transformatoren und deren Interaktion mit dem Stromnetz ist entscheidend für die Aufrechterhaltung eines zuverlässigen und sicheren Stromnetzes. Allerdings sind die verfügbaren Transformatorendaten oft unvollständig, fehlen oder sind nicht zugänglich. Bisher wurden verschiedene Ansätze zur Modellierung von Transformatoren mit unterschiedlichen Daten und Detaillierungsgraden veröffentlicht. Das Ziel unseres Ansatzes ist es, möglichst schnell und einfach ein Transformatormodell zu erstellen, um das Transformatorverhalten und die Netzinteraktion zu untersuchen. Die erforderlichen Messungen können einfach im Feld oder im Umspannwerk durchgeführt werden. Die Messungen werden zur Parameteridentifikation des Jiles-Atherton-Hysterese Modells verwendet. Der Modellansatz basiert auf dem Dualitätsprinzip, das den magnetischen Kreis in sein elektrisches Äquivalent transformiert. In dieser Arbeit demonstrieren wir diesen Ansatz am Beispiel eines 3-phasigen 3-schenkligen 50 kVA Leistungstransformator. Die Simulationen und Messung zeigen eine Übereinstimmung von mindestens 97 %. Daher kann dieser Ansatz in Industrie und Forschung verwendet werden, um Transformatoren zu modellieren und deren Verhalten und Netzinteraktion zu untersuchen.

Abstract

Modelling transformers and the power grid interaction is crucial to maintain a reliable and safe power grid. However, often the available transformer data is incomplete, missing or not accessible. Different approaches have been published for modelling transformers with different amount of data and degree of detail. The aim of this approach is, to easily setup a fast transformer model to study the transformer behaviour and grid interaction. The required measurements can be done easily in the field or substation. The measurements are used to setup the Jiles-Atherton hysteretic model. The model approach is based on the duality principle, transforming the magnetic circuit into its electric equivalent. In this work we demonstrate this approach on a 3-phase 3-limb 2-winding 50 kVA power transformer. The correlation between simulation and measurement are at least 97 %. Therefore, this approach can be used in industry and research to model transformers and study their behaviour and grid interaction.

1 Introduction

Transformers are a key component in our electrical transmission grid. Transformer outages can affect a geographically large area and can have a major economical impact [1]. To ensure a safe, reliable and quiet operation, digital transformer models are used to study the transformer behaviour and the interaction with the power grid. Especially the reactive power consumption of the transformer is of interest during increased low frequency transformer neutral point current (LFC). LFC in the transformer neutral point current can be caused by geomagnetically induced currents (GIC) or man-made systems, such as DC transportation systems [2, 3]. These LFC can cause transformer half-cycle saturation. During the saturation of the transformer the reactive power demand increases [4]. If the reactive power demand of a large number of transformer in the power grid take place at the same time, voltage instability or even outages need to be considered. Transformer models are used to study the interaction between the installed transformer with the power grid. However, these models often require detailed information about the transformer under investigation, which are not always available [5]. Also the computational power required for transformer models increases with the level of detail. Therefore, simulations with many transformer models are time and computational power consuming.

In this work we describe a new approach to set up an electromagnetic model of a power transformer, which also requires low computational power and time. The approach uses measurements and basic information about the transformer. The model is based on the duality transformation [6] and uses the Jiles-Atherton (JA) model [8] for the hysteresis implementation. The duality principle is used to transform the magnetic circuit into its equivalent electric circuit, using commonly known electric components. Thus, the magnetic field strength and magnetic flux can be easily calculated and assessed in the simulation with current and voltage measurements. The JA model is commonly used in electrical power engineering, because it re-

*The authors are equally contributing and are mentioned in alphabetic order

quires very few measurements and can be controlled with five parameters. The approach is tested with a 3-phase 3-limb 2-winding 50 kVA power transformer. The current and voltage wave forms of the simulation and measurement are in good accordance and don't require high computational power. Therefore, multiple transformers can be used simultaneously in a power grid simulation to study the transformer interaction with the rest of the grid.
This modelling approach does not yield the simulation of heating or mechanical stress on the transformer, neither does it simulate transient behaviour in terms of frequencies above 1 kHz.

2 Fundamentals

2.1 Duality Principle

It was shown in [6] that the topological principle of duality can be applied to transformers. With this method, the topological correct magnetic circuit of a transformer can be converted into an equivalent electric circuit. First, a magnetic circuit with all the major flux paths can be drawn. Then, the nodes/loops of the magnetic circuit are converted into loops/nodes of the equivalent electric circuit. The reluctances are converted into inductances, the magnetomotive sources turn into current sources. The general principle can only be applied to transformers where the windings have an equal amount of turns. The current sources can be replaced by ideal transformers in order to overcome this limitation. Another limitation is that duality is only possible for planar networks. This means that in the case of a transformer a maximum amount of three coil pairs can be modelled if all leakage flux paths are included. **Fig. 1** shows the resulting equivalent electric network of the 3-phase 3-limb 2-winding core-type transformer. It includes the hysteretic elements in the limbs and yokes of the core. Resistors were added in parallel to the JA-elements in order to model the dynamic core losses. A more accurate approach is the inclusion of a rate dependant dynamic hysteresis model [7]. The inductances L_0 represent the zero sequence flux path. The inductances L_{LC} and L_{HL} represent the stray flux path between core and low voltage winding and the low and high voltage winding respectively. The winding resistances were added to the terminals of the ideal transformers. The derived circuit is only valid for the investigated core topology.

2.2 Jiles-Atherton Model

The JA model is developed on the physical effect of domain wall motion under the influence of an applied magnetic field [8]. Although the JA model attempts to describe the physical behaviour of the materials, it shows non-physical behaviour [9]. Nevertheless, the JA model is used because is accurately calculates the electrically behaviour at the transformer terminals. the In this paper, the JA model is used in differential form, described in Eq. 11. The physical link of the parameters in Eq. 11 are presented in **Tab. 1** and need to be determined iterative with the use of measurements.

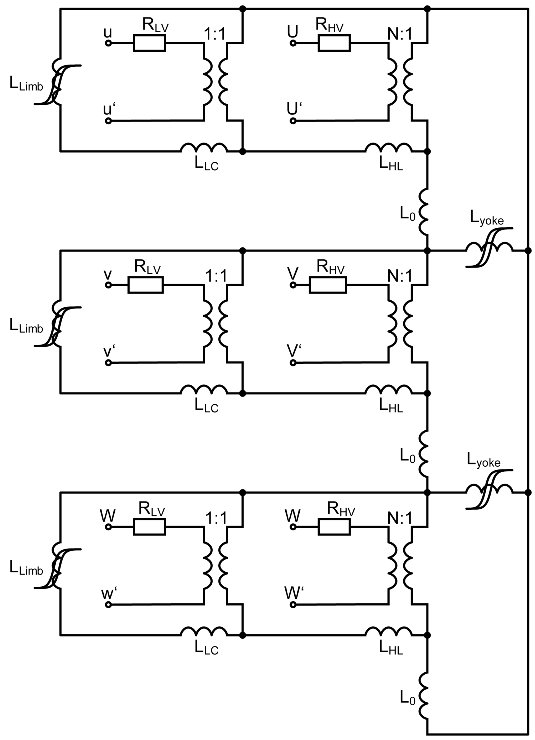

Figure 1 3-phase 3-leg transformer duality principle equivalent circuit

Parameter	Physical link
α	domain wall interaction
a	M_{an} shape
k	hysteresis losses
c	reversibility coefficient
M_{sat}	saturation magnetization
δ	direction of magnetizing field ± 1

Table 1 JA parameters and physical link

The implementation of the hysteresis elements in MATLAB/Simulink are presented in **Fig. 2**. The voltage across the hysteresis element is measured and integrated, giving the voltage-seconds across the element. With the geometric parameters of the transformer core, the magnetic flux density B is derived. The JA model itself uses Eq. 2 to 13 in the presented order to calculate the output as magnetic field strength H. In the last step the equivalent current is calculated from the H field using the geometric transformer data. This current is used to control a current source at the second terminal of the hysteresis block. The time delay block is used to increase the model stability. Further information on the time delay are given in Sec. 4.

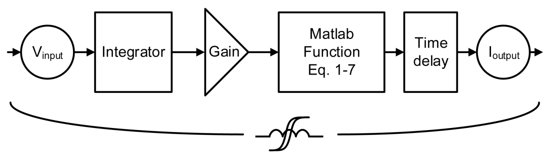

Figure 2 Block diagram of JA implementation in MATLAB/Simulink

3 Modelling Approach and Application

The presented modelling approach in this work requires the following parameters:

- core cross-section area
- magnetic path length of limb and yoke
- number of turns on high- and low-voltage winding
- winding resistance
- winding location relative to the core
- stray impedance
- zero-sequence impedance
- vector group
- transformer design (shell or core type; effect flux paths)

This data can be provided by the transformer manufacturer or be partly self-measured. The data for the transformer under test is listed in **Tab. 5** and **Tab. 4**.

3.1 Standard measurements

For the following section, the parameters refer to the YNyn0 transformer, as presented in **Fig. 3**. All measurements were carried out with a power amplifier. This power amplifier is able to supply a near perfect sinusoidal voltage with constant amplitude.

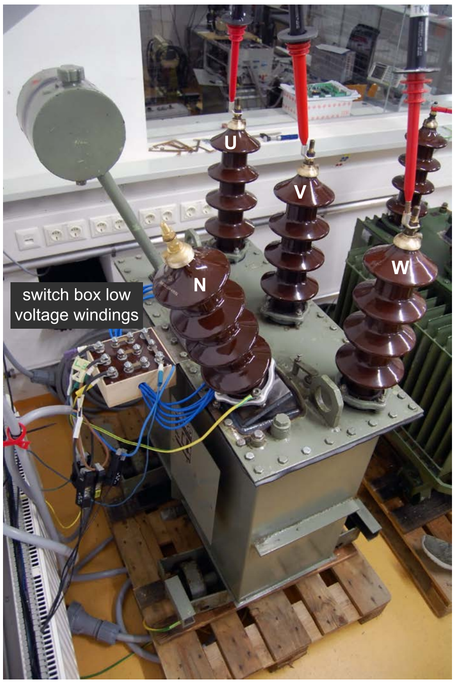

Figure 3 Laboratory setup with transformer under test

For the transformer model the zero-sequence impedance z_0, the winding resistance and the stray impedance are measured with the standard tests, according to [10]. The measured parameters are listed in Tab. 2. The transformer name plate data can be found in Tab. 4.

Z_0* Ω/phase	R_{HV} Ω	R_{LV} mΩ	$X_{1,2\sigma}$ mΩ
2.3	323	32	231

Table 2 Measured transformer parameters, according to [10] with a peak current of 101.8 A, a peak voltage of 78 V in YNyn vector group, with the low voltage windings connected in parallel and the high voltage terminals in open circuit configuration

3.2 1-phase no load test

The measured power and phase currents from a regular three-phase no-load test do not represent the currents required to produce the magnetomotive force by the actual core sections in the investigated YNyn0 transformer. Each phase current depends not only on the core section the winding is on, but on the other core sections as well [11]. In order to measure the true magnetic properties of the core material, a 1-phase measurement setup shown in **Fig. 4** was chosen. That way the magnetic coupling that would occur at a three-phase test can be prevented. In an ideal transformer, the fluxes in the middle limb would cancel each other out, leading to the main flux only appearing in the yokes and outer limbs. The measurement was executed at a frequency of 10 Hz in order to minimize dynamic effects. Another benefit of measuring at lower frequencies is the lower voltage amplitude required to reach the same flux amplitude, making the measurement possible even with mobile measuring/source devices.

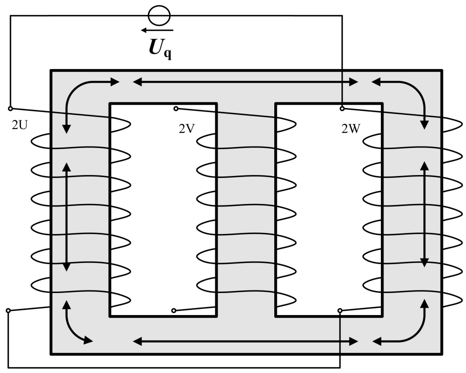

Figure 4 1-phase no-load measurement setup

3.3 JA-Parameter fit and results

The voltage drop across the windings is subtracted from measured voltage. The resulting voltage is integrated to obtain the magnetic flux. The setup shown in Fig. 4 was recreated in the simulation model and was used to fit the simulated characteristic to the measured one. The Jiles-Atherton parameters were roughly fitted by hand. This led to the parameters shown in **Tab. 3**. Fig. 5 shows the resulting flux-current characteristics.

In order to verify the parameters, a 3-phase no-load test at 50 Hz and nominal voltage was simulated and compared to the measurement. The fitted parameters in Tab. 3 were used

ETG-Kongress 2021 . ISBN 978-3-8007-5549-3 . ©VDE VERLAG GMBH . Berlin . Offenbach

Ms	a	c	α	k
$1.75{\cdot}10^6$	100	0.15	$0.16{\cdot}10^{-3}$	15

Table 3 JA-parameters

for every core element in the simulation. The dynamic hysteresis losses were fitted by means of a resistor in parallel to the hysteretic element. This resistor was adapted to fit the simulated 50 Hz no-load test to the measured one. The resulting phase currents are shown in **Fig. 6**. The simulated currents in phases U and W are in good accordance. The amplitude of the simulated current in phase V is smaller than the measured current. This was corrected by adjusting the JA-parameters for the middle limb separately. The saturation magnetization M_{sat} for the middle limb was lowered to $1.65 \cdot 10^6$. The resulting currents are shown in **Fig. 7**. In the case of a short circuit test, the behaviour depends mostly on the stray flux path. This behaviour can simply be modelled with the linear stray inductance L_{12}. The simulation shows an accurate representation in case of a simulated short-circuit test.

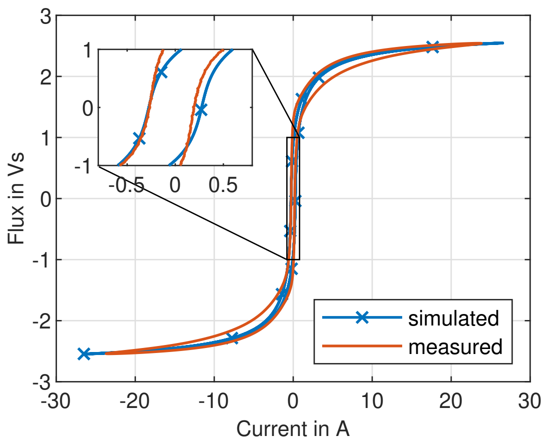

Figure 5 1 phase flux-current-characteristic measured and simulated at 160 V_{peak} 10 Hz

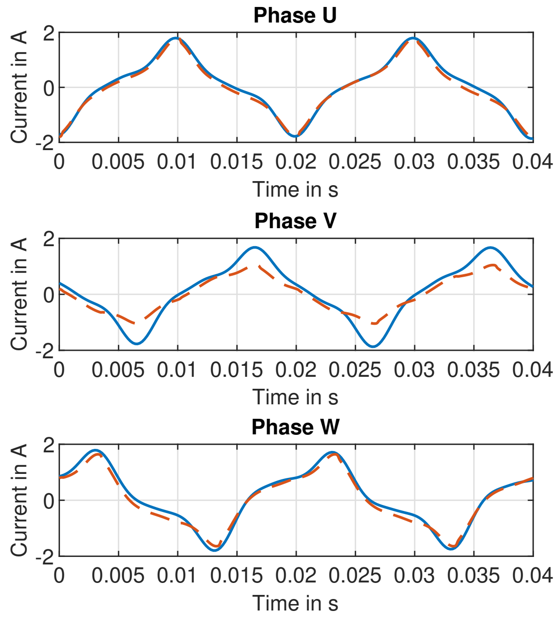

Figure 6 No load phase currents measured (solid) and simulated (dashed) at 50 Hz using identical parameters for all sections

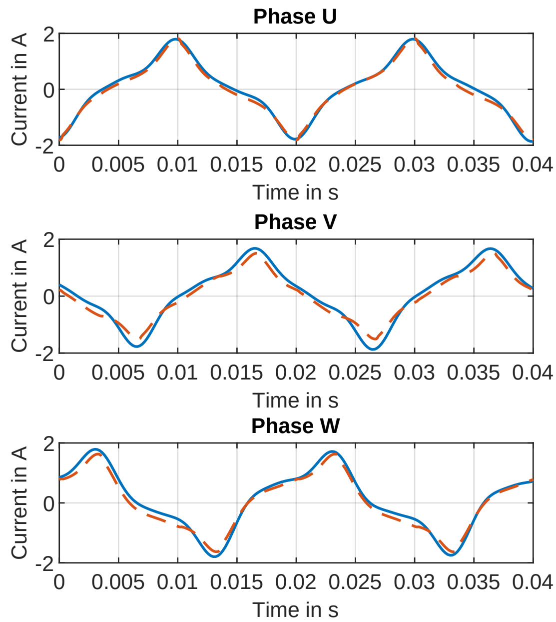

Figure 7 No load phase currents measured (solid) and simulated (dashed) at 50 Hz using adjusted parameters for phase V

4 Discussion

1-phase no load test and dynamic losses

The comparison of the flux-current-characteristic in Fig. 5 shows a deviation of the simulation to the measurement. The measured characteristic widens at the knee points, which could be attributed to a dynamic loss component [7].

In its current form, the model uses the traditional method of resistors in parallel to the Jiles-Atherton elements to model the dynamic losses. This method leads to inaccuracies when the voltage exceeds its nominal value. A more generally valid method is the inclusion of a rate-dependant dynamic hysteresis model [7].

Correction of phase V

The model assumes a perfect and joint-less core. It can be necessary to adjust the parameters for core sections in order to factor in those imperfections. The low simulated current in phase V can be corrected by adjusting the Jiles-Atherton parameters for the middle limb. Since the general shape of the simulated current fits the measured one, it was sufficient to decrease the saturation magnetization M_{sat}.

The correction had no significant influence on the other phase currents as seen in Fig. 7.

Non-sinusoidal excitation and DC offset flux
The model accuracy will be determined for non-sinusoidal excitation and DC transformer neutral point currents in further measurement and simulation comparisons. Non-sinusoidal excitation and DC transformer neutral point currents can be present in technical applications, such as in the power transmission grid [3]. The measurements will be carried out with a transformer back-to-back setup and a power amplifier. In [12] a decreasing accuracy of the JA model is measured, if additional harmonics are present. The measurements from [12] are done with a small scale single phase test bench. Therefore, large scale tests with power transformers should be carried out, to estimate the simulation-model accuracy in a technical application scale.

Simulation stability
The transfer from Eq. 1 is used to introduce a time delay to increase the simulation stability. Decreasing b shifts the -3 dB cut-off frequency and the phase reduction to a higher frequency. Thus the time delay is decreased with decreasing parameter b. For the shown simulations $\mathrm{b} = 5 \cdot 10^{-5}$ was used. The corresponding -3 dB cut-off frequency is at 3.18 kHz and thus does not affect the stationary frequency spectrum of the simulation.

$$\frac{1}{\mathrm{b}s+1} \tag{1}$$

The simulation stability during the energizing of the transformer can be further increased with a voltage ramp.

5 Conclusion

In conclusion, a measurement based model approach for transformer modelling is proposed. The model approach includes the hysteresis effect of the core material. The comparison of the measurements and simulation using the example of a 3-limb 3-phase 2-winding 50 kVA power transformer show a very good agreement. Therefore, the approach can be used especially for power transformer where no detailed information are available. The required data for the model can easily be measured, even in the field/substation. The combination of easy measurements, duality principle based model and the fast computation time can be a valuable tool for industry and research to study transformer behaviour and power grid interactions.

6 Literature

[1] Eastwood, J. P.; Biffis, E.; Hapgood, M. A.; Green, L.; Bisi, M. M.; Bentley, R. D.; Wicks, R.; McKinnell, L-A; Gibbs, M.; Burnett, C. *The Economic Impact of Space Weather: Where Do We Stand?*. Risk Analysis, 37: 206-218 (2017). https://doi.org/10.1111/risa.12765

[2] Albert, D.; Halbedl, T.; Renner, H.; Bailey, R. L., Achleitner, G. *Geomagnetically induced currents and space weather - A review of current and future research in Austria*. 54th International Universities Power Engineering Conference (UPEC), Bucharest, Romania, pp. 1-6, (2019). https://doi.org/10.1109/UPEC.2019.8893515

[3] Albert, D.; Schachinger, P.; Renner, H. et al. *Field experience of small quasi-DC bias on power transformers*. Elektrotech. Inftech. 137, 427–436 (2020). https://doi.org/10.1007/s00502-020-00846-1

[4] Prohammer, A.; Rueschitz, M.;Albert, D.;Renner, H. *Transformer Saturation Methods and Transformer Response to Low Frequency Currents*. IEEE Power and Energy Student Summit, PESS, pp. 1-6, (2020). `https://ieeexplore.ieee.org/stamp/stamp.jsp?tp=&arnumber=9273802`

[5] Shafieipour, M.; Alonso, J. C. G.; Jayasinghe, R. P.; Gole. A. M. *Principle of Duality with Normalized Core Concept for Modeling Multi-Limb Transformers*. International Conference on Power Systems Transients (IPST2019), Peripignan, France, (2019).

[6] Cherry, C. E. *The Duality between Interlinked Electric and Magnetic Circuits and the Formation of Transformer Equivalent Circuits*. Proc. Phys. Soc. B 62, 101-111 (1949). http://dx.doi.org/10.1088/0370-1301/62/2/303

[7] S. Jazebi et al., *Duality-Derived Transformer Models for Low-Frequency Electromagnetic Transients—Part II: Complementary Modeling Guidelines*. IEEE Transactions on Power Delivery vol. 31, no. 5, 2420-2430, (2016). https://doi.org/10.1109/TPWRD.2016.2556686

[8] Jiles, D. C. and Atherton, D. L.: *Theory of ferromagnetic hysteresis*. Journal of Magnetism and Magnetic Materials 61, 48-60 (1986). https://doi.org/10.1016/0304-8853(86)90066-1

[9] Zirka, S. E.; Moroz, Y. I.; Harrison, R. G.; Chwastek, K. *On physical aspects of the Jiles-Atherton hysteresis models* J. Appl. Phys. 112, 043916 (2012); https://doi.org/10.1063/1.4747915

[10] IEC 60076-1:2011; Power Transformers - Part 1: General

[11] Walker, C. S. *The Excitation Requirements of 3-Phase Core-Type 3-Legged Y-Connected Transformers.* Transactions of the American Institute of Electrical Engineers. Part III: Power Apparatus and Systems, vol. 76, no. 3, pp. 1113-1119, (1957). https://doi.org/10.1109/AIEEPAS.1957.4499731.

[12] Benabou, A.; Clenet, S.; Piriou, F. *Comparison of Preisach and Jiles–Atherton models to take into account hysteresis phenomenon for finite element analysis*. Journal of Magnetism and Magnetic Materials 261, 139-160 (2002). https://doi.org/10.1016/S0304-8853(02)01463-4

[13] Sadowski, N.; Batistela, N. J.; Bastos, J. P. A.; Lajoie-Mazenc, M. *An inverse Jiles-Atherton*

model to take into account hysteresis in time-stepping finite-element calculations IEEE Transactions on Magnetics, vol. 38, no. 2, pp. 797-800, (2002). https://doi.org/10.1109/20.996206

[14] Jiles, D. C.; Thoelke, J. B.; Devine, M. K. *Numerical determination of hysteresis parameters for the modeling of magnetic properties using the theory of ferromagnetic hysteresis* IEEE Transactions on Magnetics, vol. 28, no. 1, pp. 27-35, (1992) https://doi.org/10.1109/20.119813

[15] Deane, J. H. B. *Modeling the dynamics of nonlinear inductor circuits* IEEE Transactions on Magnetics, vol. 30, no. 5, pp. 2795-2801, (1994). https://doi.org/10.1109/20.312521

Appendix

Z_{ref} kΩ	U_1 kV	U_2 kV	S kVA
15.7	28	0.4	50

Table 4 Name plate of transformer under test

Tab. 5 lists the geometric data of the transformer under test. The dimensions were measured during the modification of the low voltage windings. A_{core} is the uniform core cross-section area of the yoke and limb. N_1 and N_2 are the number of turns of the high-voltage and low- voltage winding, respectively. The yoke length l_{yoke} and limb length l_{limb} are the middle iron path of the yoke and limb.

A_{core} mm²	N_1	N_2	l_{yoke} mm	l_{limb} mm
6001	7730	102	237	440

Table 5 Geometric data of transformer

The original Jiles-Atherton model uses the magnetic field H as an input to calculate the magnetization M. In this model an inverse Jiles-Atherton model was used, with the magnetic flux density B as an input and the magnetization M as an output. The hysteretic elements use a calculation based on [13]. This method can however lead to unphysical solutions at the loop tips [14]. To overcome this behaviour the parameter δ_M calculated in Eq. 9 was added to Eq. 10. This parameter is based on [15] and was adapted to fit the inverese Jiles-Atherton model.

Eq. 2 to 13 define the calculation in the hysteretic element, presented in fig. 2, according to [13].

$$H(t) = \frac{B(t)}{\mu_0} - M(t) \tag{2}$$

$$\Delta B = B(t+\Delta t) - B(t) \tag{3}$$

$$M(t) = \frac{B(t)}{\mu_0} - H(t) \tag{4}$$

$$H_e(t) = H(t) + \alpha M(t) \tag{5}$$

$$M_{an}(t) = M_s \left[\coth\frac{H_e(t)}{a} - \frac{a}{H_e(t)}\right] \tag{6}$$

$$\frac{dM_{an}}{dH_e} = \frac{M_s}{a}\left[1 - \coth^2\frac{H_e(t)}{a} + \left(\frac{a}{H_e(t)}\right)^2\right] \tag{7}$$

$$M_{irr}(t) = \frac{M(t) - cM_{an}(t)}{1-c} \tag{8}$$

$$\delta_M = \begin{cases} 0 : \Delta B < 0 \quad \text{and} \quad M_{an}(t) - M(t) > 0 \\ 0 : \Delta B > 0 \quad \text{and} \quad M_{an}(t) - M(t) < 0 \\ 1 : \text{otherwise} \end{cases} \tag{9}$$

$$\frac{dM_{irr}}{dB_e} = \delta_M \frac{M_{an}(t) - M_{irr}(t)}{\mu_0 k \delta} \tag{10}$$

$$\frac{dM}{dB} = \frac{(1-c)\frac{dM_{irr}}{dB_e} + \frac{c}{\mu_0}\frac{dM_{an}}{dH_e}}{1 + \mu_0(1-\alpha)(1-c)\frac{dM_{irr}}{dB_e} + c(1-\alpha)\frac{dM_{an}}{dH_e}} \tag{11}$$

$$M(t+\Delta t) = M(t) + \frac{dM}{dB}\Delta B \tag{12}$$

$$H(t+\Delta t) = \frac{B(t+\Delta t)}{\mu_0} - M(t+\Delta t) \tag{13}$$

Bibliography

[1] S. V. Kulkarni and S. A. Khaparde, *Transformer engineering, Design, technology, and diagnostics*, 2nd ed. CRC Press, 2017, 750 pp., ISBN: 9781351833226 (cit. on pp. 1, 5, 10, 15).

[2] S. Jazebi, S. E. Zirka, M. Lambert, A. Rezaei-Zare, N. Chiesa, Y. Moroz, X. Chen, M. Martinez-Duro, C. M. Arturi, E. P. Dick, A. Narang, R. A. Walling, J. Mahseredjian, J. A. Martinez, and F. de Leon, "Duality derived transformer models for low-frequency electromagnetic transients—part i: Topological models," *IEEE Transactions on Power Delivery*, vol. 31, no. 5, pp. 2410–2419, 2016. DOI: 10.1109/TPWRD.2016.2517327 (cit. on pp. 1, 16, 17).

[3] S. Jazebi, F. de Leon, A. Farazmand, and D. Deswal, "Dual reversible transformer model for the calculation of low-frequency transients," *IEEE Transactions on Power Delivery*, vol. 28, no. 4, pp. 2509–2517, 2013. DOI: 10.1109/TPWRD.2013.2268857 (cit. on pp. 1, 61).

[4] N. Chiesa and H. K. Høidalen, "Hysteretic iron-core inductor for transformer inrush current modelling in emtp," *PSCC 2008-16th Power Systems Computation Conference*, 2008 (cit. on pp. 1, 16, 21, 61).

[5] S. Jazebi, A. Rezaei-Zare, M. Lambert, S. E. Zirka, N. Chiesa, Y. I. Moroz, X. Chen, M. Martinez-Duro, C. M. Arturi, E. P. Dick, A. Narang, R. A. Walling, J. Mahseredjian, J. A. Martinez, and F. de Leon, "Duality-derived transformer models for low-frequency electromagnetic transients—part ii: Complementary modeling guidelines," *IEEE Transactions on Power Delivery*, vol. 31, no. 5, pp. 2420–2430, 2016, ISSN: 0885-8977. DOI: 10.1109/TPWRD.2016.2556686 (cit. on pp. 1, 15, 28, 30, 53, 61, 64).

[6] S. E. Zirka, Y. I. Moroz, N. Chiesa, R. G. Harrison, and H. K. Hoidalen, "Implementation of inverse hysteresis model into emtp—part ii: Dynamic model," *IEEE Transactions on Power Delivery*, vol. 30, no. 5, pp. 2233–2241, 2015. DOI: 10.1109/TPWRD.2015.2416199 (cit. on pp. 1, 28, 29).

[7] E. Ivers-Tiffée and W. von Münch, *Werkstoffe der Elektrotechnik, Mit 40 Tabellen*, ger, 10., überarb. und erw. Aufl., ser. Lehrbuch Elektrotechnik. Wiesbaden: Teubner, 2007, 266 pp., ISBN: 3835100521. [Online]. Available: `http://deposit.dnb.de/cgi-bin/dokserv?id=2657494&prov=M&dok_var=1&dok_ext=htm` (cit. on pp. 7–9, 24).

[8] F. Liorzou, B. Phelps, and D. L. Atherton, "Macroscopic models of magnetization," *IEEE Transactions on Magnetics*, vol. 36, no. 2, pp. 418–428, 2000. DOI: `10.1109/20.825802` (cit. on pp. 10, 21).

[9] J. Pearson, P. T. Squire, and D. Atkinson, "Which anhysteretic magnetization curve?" *IEEE Transactions on Magnetics*, vol. 33, no. 5, pp. 3970–3972, 1997. DOI: `10.1109/20.619632` (cit. on p. 10).

[10] C. S. Walker, "The excitation requirements of 3-phase core-type 3-legged y-connected transformers," *Transactions of the American Institute of Electrical Engineers. Part III: Power Apparatus and Systems*, vol. 76, no. 3, pp. 1113–1119, 1957. DOI: `10.1109/AIEEPAS.1957.4499731` (cit. on pp. 10, 11, 31, 67).

[11] CIGRE Working Group 02, "Guidelines for representation of network elements when calculating transients," *CIGRE Brochure 39*, 1990 (cit. on p. 15).

[12] J. A. Martinez and B. A. Mork, "Transformer modeling for low- and mid-frequency transients—a review," *IEEE Transactions on Power Delivery*, vol. 20, no. 2, pp. 1625–1632, 2005. DOI: `10.1109/TPWRD.2004.833884` (cit. on pp. 15, 16).

[13] B. A. Mork, F. Gonzalez, D. Ishchenko, D. L. Stuehm, and J. Mitra, "Hybrid transformer model for transient simulation—part i: Development and parameters," *IEEE Transactions on Power Delivery*, vol. 22, no. 1, pp. 248–255, 2007. DOI: `10.1109/TPWRD.2006.883000` (cit. on pp. 17, 30).

[14] N. Chiesa and H. K. Høidalen, "Systematic switching study of transformer inrush current: Simulations and measurements," *IPST'09 - International Conference on Power System Transients*, vol. IPST-139, Kyoto, Japan, Jun. 2009, 2009 (cit. on pp. 17, 30, 37, 63).

[15] E. C. Cherry, "The duality between interlinked electric and magnetic circuits and the formation of transformer equivalent circuits," *Proceedings of the Physical Society. Section B*, vol. 62, no. 2, pp. 101–111, 1949 (cit. on pp. 17–19, 61).

[16] H. Whitney, "Non-separable and planar graphs," *Transactions of the American Mathematical Society*, vol. 34, no. 2, pp. 339–362, 1932, PII: S0002994719321501641 2. DOI: 10.1090/S0002-9947-1932-1501641-2 (cit. on p. 17).

[17] C. M. Arturi, "Transient simulation and analysis of a three-phase five-limb step-up transformer following an out-of-phase synchronization," *IEEE Transactions on Power Delivery*, vol. 6, no. 1, pp. 196–207, 1991. DOI: 10.1109/61.103738 (cit. on p. 17).

[18] N. Chiesa, B. A. Mork, and H. K. Høidalen, "Transformer model for inrush current calculations: Simulations, measurements and sensitivity analysis," *IEEE Transactions on Power Delivery*, vol. 25, no. 4, pp. 2599–2608, 2010. DOI: 10.1109/TPWRD.2010.2045518 (cit. on pp. 17, 19).

[19] B. A. Mork, "Five-legged wound-core transformer model: Derivation, parameters, implementation and evaluation," *IEEE Transactions on Power Delivery*, vol. 14, no. 4, pp. 1519–1526, 1999. DOI: 10.1109/61.796249 (cit. on p. 19).

[20] F. de Leon and A. Semlyen, "A simple representation of dynamic hysteresis losses in power transformers," *IEEE Transactions on Power Delivery*, vol. 10, no. 1, pp. 315–321, 1995. DOI: 10.1109/61.368383 (cit. on p. 21).

[21] D. A. Philips, L. R. Dupre, and J. A. Melkebeek, "Comparison of jiles and preisach hysteresis models in magnetodynamics," *IEEE Transactions on Magnetics*, vol. 31, no. 6, pp. 3551–3553, 1995. DOI: 10.1109/20.489566 (cit. on p. 21).

[22] D. C. Jiles and D. L. Atherton, "Theory of ferromagnetic hysteresis," *Journal of Magnetism and Magnetic Materials*, vol. 61, no. 1-2, pp. 48–60, 1986, PII: 0304885386900661, ISSN: 03048853. DOI: 10.1016/0304-8853(86)90066-1 (cit. on pp. 21, 22, 62).

[23] D. C. Jiles, J. B. Thoelke, and M. K. Devine, "Numerical determination of hysteresis parameters for the modeling of magnetic properties using the theory of ferromagnetic hysteresis," *IEEE Transactions on Magnetics*, vol. 28, no. 1, pp. 27–35, 1992. DOI: 10.1109/20.119813 (cit. on pp. 21, 25, 26).

[24] S. E. Zirka, Y. I. Moroz, C. M. Arturi, N. Chiesa, and H. K. Hoidalen, "Topology-correct reversible transformer model," *IEEE Transactions on Power Delivery*, vol. 27, no. 4, pp. 2037–2045, 2012. DOI: 10.1109/TPWRD.2012.2205275 (cit. on p. 21).

[25] D. Lederer, H. Igarashi, A. Kost, and T. Honma, "On the parameter identification and application of the jiles-atherton hysteresis model for numerical modelling of measured characteristics," *IEEE Transactions on Magnetics*, vol. 35, no. 3, pp. 1211–1214, 1999. DOI: 10.1109/20.767167 (cit. on pp. 26, 27).

[26] J. Deane, "Modeling the dynamics of nonlinear inductor circuits," *IEEE Transactions on Magnetics*, vol. 30, no. 5, pp. 2795–2801, 1994. DOI: 10.1109/20.312521 (cit. on pp. 27, 73).

[27] N. Sadowski, N. J. Batistela, J. Bastos, and M. Lajoie-Mazenc, "An inverse jiles-atherton model to take into account hysteresis in time-stepping finite-element calculations," *IEEE Transactions on Magnetics*, vol. 38, no. 2, pp. 797–800, 2002. DOI: 10.1109/20.996206 (cit. on pp. 27, 73).

[28] U. D. Annakkage, P. G. McLaren, E. Dirks, R. P. Jayasinghe, and A. D. Parker, "A current transformer model based on the jiles-atherton theory of ferromagnetic hysteresis," *IEEE Transactions on Power Delivery*, vol. 15, no. 1, pp. 57–61, 2000. DOI: 10.1109/61.847229 (cit. on pp. 27, 62).

[29] S. E. Zirka, Y. I. Moroz, A. J. Moses, and C. M. Arturi, "Static and dynamic hysteresis models for studying transformer transients," *IEEE Transactions on Power Delivery*, vol. 26, no. 4, pp. 2352–2362, 2011. DOI: 10.1109/TPWRD.2011.2140404 (cit. on pp. 27–29).

[30] G. Bertotti, *Hysteresis in magnetism, For physicists, materials scientists and engineers*, eng, Digitaler Nachdr, ser. Academic Press series in electromagnetism. San Diego, Calif.: Acad. Press, 2008, 558 pp., ISBN: 9780120932702 (cit. on p. 28).

[31] W. Chandrasena, P. G. McLaren, U. D. Annakkage, and R. P. Jayasinghe, "An improved low-frequency transformer model for use in gic studies," *IEEE Transactions on Power Delivery*, vol. 19, no. 2, pp. 643–651, 2004. DOI: 10.1109/TPWRD.2004.824429 (cit. on pp. 29, 32).

[32] Austrian Standards Institute, Ed., *Power transformers – part 1: General*, Apr. 1, 2012 (cit. on pp. 30, 37, 50, 63).

[33] D. Albert, D. Maletic, and H. Renner, "Measurement based transformer modelling approach," in *Internationaler ETG-Kongress 2021, Das Gesamtsystem im Fokus der Energiewende : 18.-19. Mai 2021*, Energietechnische Gesellschaft, Ed., ser. ETG-Fachbericht, Berlin and Offenbach: VDE Verlag GmbH, 2021, pp. 578–583, ISBN: 978-3-8007-5549-3 (cit. on pp. 32, 62).

[34] B. Taupe, *Umbau zweier Leistungstransformatoren zur flexiblen Änderung der Schaltgruppe (BSc thesis)*. Institute of Electrical Power Systems, Graz University of Technology, 2020 (cit. on p. 35).

[35] B. A. Mork, D. Ishchenko, F. Gonzalez, and S. D. Cho, "Parameter estimation methods for five-limb magnetic core model," *IEEE Transactions on Power Delivery*, vol. 23, no. 4, pp. 2025–2032, 2008. DOI: 10.1109/TPWRD.2008.923164 (cit. on p. 35).

[36] C. Kath, J. Velásquez, S. Wenig, S. Beckler, J. Reisbeck, and R. Sapetschnig, "Vor-ort-messung der hysteresekurve von leistungstransformatoren zur verbesserten modellierung und simulation transienter vorgänge," in *ETG-Fb. 162: VDE Hochspannungstechnik, ETG-Fachtagung, 9.–11. November 2020, Online-Veranstaltung*, ser. ETG-Fachberichte, Berlin: VDE Verlag GmbH, 2020, ISBN: 978-3-8007-5353-6 (cit. on p. 40).

[37] F. de Leon and J. A. Martinez, "Dual three-winding transformer equivalent circuit matching leakage measurements," *IEEE Transactions on Power Delivery*, vol. 24, no. 1, pp. 160–168, 2009. DOI: 10.1109/TPWRD.2008.2007012 (cit. on p. 61).